IMAGING CHOLESTEROL METABOLISM AND TRAFFICKING BY STIMULATED RAMAN SCATTERING MICROSCOPY

by

Hyeon Jeong Lee

A Dissertation

Submitted to the Faculty of Purdue University

In Partial Fulfillment of the Requirements for the degree of

Doctor of Philosophy

Department of Comparative Pathobiology

West Lafayette, Indiana

December 2017

THE PURDUE UNIVERSITY GRADUATE SCHOOL
STATEMENT OF COMMITTEE APPROVAL

Dr. Ji-Xin Cheng, Co-Chair

Weldon School of Biomedical Engineering

Dr. Timothy L. Ratliff, Co-Chair

Department of Comparative Pathobiology

Dr. Xiaoqi Liu

Department of Biochemistry

Dr. Kinam Park

Weldon School of Biomedical Engineering

Approved by:

Dr. Christine A. Hrycyna

Head of the Graduate Program

To my parents and my grandparents for always believing in me. To my husband, Delong Zhang, for his continued support, patience and love.

I thank Sandra Torregrosa-Allen and Melanie Currie from Purdue Cancer Center, Dr. Andy Schaber from Imaging Facility, Gabrielle Shafer and Victor A. Bernal-Crespo from Histology Research Laboratory, Dr. Amber Jannasch and Victoria Hedrick from Bindley Bioscience Center, for their great help and technical support.

Finally, I am grateful to my husband and colleague, Dr. Delong Zhang, for his endless support and love, which brought all the happiness to my life.

TABLE OF CONTENTS

LIST OF TABLES

LIST OF FIGURES

LIST OF ABBREVIATIONS

3D	three-dimensional
ABC	ATP-binding cassette
ACAT	acyl-coenzyme A: cholesterol acyltrasferase
A-Chol	alkyne cholesterol
ADT	androgen deprivation therapy
AOM	acousto-optic modulator
ATCC	American Type Culture Collection
BODIPY	boron dipyrromethene difluoride
C. elegans	*Caenorhabditis elegans*
CARS	coherent anti-Stokes Raman scattering
CE	cholesteryl ester
CHO	Chinese hamster ovary
CN-Chol	cyano cholesterol
CRS	coherent Raman scattering
DHE	dehydroergosterol
DMSO	dimethyl sulfoxide
EOM	electro-optic modulator
FAD	flavin adenine dinucleotide
FBS	fetal bovine serum
H&E	hematoxylin and eosin
HDL	high-density lipoprotein
HMG-CoA	3-hydroxy-3-methylglutaryl coenzyme A
HPβCD	hydroxypropyl β-cyclodextrin
IFC	immunofluorescent chemistry
LC-MS	Liquid Chromatography-Mass Spectrometry
LDL	low-density lipoprotein
LDs	lipid droplets
LROs	lysosome-related organelles
LXR	liver X receptor

MCR	multivariate curve resolution
NADH	nicotinamide adenine dinucleotide
NBD	7-nitrobenz-2-oxa-1,3-diazole
NEAA	non-essential amino acids
NP-C	Niemann-Pick type C
NPC1	Niemann-Pick type C1
NPC2	Niemann-Pick type C2
OPO	optical parametric oscillator
ORPs	oxysterol binding protein-related proteins
PBR	peripheral benzodiazepine receptor
PCA	principle component analysis
PCa	prostate cancer
PhA-Chol	phenyl-alkyne cholesterol
PhDY-Chol	phenyl-diyne cholesterol
RXR	retinoid X receptor
SCD1	stearoyl-CoA desaturase
SD	standard deviation
SEM	standard error of the mean
SREBPs	sterol regulatory element-binding proteins
SRG	stimulated Raman gain
SRL	stimulated Raman loss
SRS	stimulated Raman scattering
SSD	sterol-sensing domain
StAR	steroidogenesis acute regulatory protein
START	StAR-related lipid transfer
TCGA	The Cancer Genome Atlas
TPEF	two-photon excitation fluorescence

ABSTRACT

Author: Lee, Hyeon Jeong. PhD
Institution: Purdue University
Degree Received: December 2017
Title: Imaging Cholesterol Metabolism and Trafficking by Stimulated Raman Scattering Microscopy
Major Professor: Ji-Xin Cheng

Cholesterol is an essential component of mammalian cells which is tightly regulated. However, our understanding of cholesterol transport and metabolism is still incomplete, partly due to lack of suitable tools for studying cholesterol dynamics in living cells and organisms with spatio-temporal information. My dissertation work applied spectroscopic imaging of cholesterol in human tissues, living cells, and model organisms to unravel new insights of cholesterol metabolism and trafficking.

Using stimulated Raman spectroscopic analysis of lipid droplets in human prostate cancer patient tissues, we observed an aberrant accumulation of cholesteryl ester in metastatic lesions. Inhibition of cholesterol esterification in prostate cancer cells significantly suppresses the development and growth of metastatic cancer lesions in both orthotopic and intra-cardiac injection mouse models. Gene expression profiling shows that cholesteryl ester depletion suppresses the metastatic potential through upregulation of multiple regulators that negatively impact metastasis. Additionally, Wnt/β-catenin, one of vital pathways for metastasis, is downregulated upon cholesteryl ester depletion. Mechanistically, we found evidence suggesting that inhibition of cholesterol esterification significantly blocks secretion of Wnt3a through reduction of monounsaturated fatty acid levels, which limits Wnt3a acylation. These results collectively validate cholesterol esterification as a novel metabolic target for treating metastatic prostate cancer.

My thesis work also developed a new biocompatible cholesterol analog, which enabled real-time imaging of cholesterol metabolism and trafficking in living cells and organisms. Based on quantum chemistry calculations, we designed and synthesized phenyl-diyne cholesterol (PhDY-Chol), which has an extremely large Raman scattering cross section. The phenyl-diyne group is biologically inert and provides a Raman scattering cross section that is 88 times larger than the

endogenous C=O stretching mode. Stimulated Raman scattering microscopy offers an imaging speed that is faster than spontaneous Raman microscopy by three orders of magnitude, and a detection sensitivity of 31 μM PhDY-Chol (~1,800 molecules in the excitation volume). Inside living cells, PhDY-Chol mimics the behavior of cholesterol, including membrane incorporation and esterification. In a cellular model of Niemann-Pick type C disease, PhDY-Chol reflects the lysosomal accumulation of cholesterol, and shows relocation to lipid droplets after HPβCD treatment. In living *C. elegans*, PhDY-Chol mimics cholesterol uptake by intestinal cells and reflects cholesterol storage. Together, this work demonstrates an enabling platform for study of cholesterol trafficking in living cells and organisms.

1. INTRODUCTION

1.1 Intracellular cholesterol trafficking and metabolism

Cholesterol is a lipid with multiple functions. It is an essential component of cellular membrane, which influences physical properties of membrane such as fluidity [1]. In addition, it plays an important role in the formation of membrane domains, lipid rafts [1, 2]. Cholesterol serves as the precursor for steroid hormones (progestogen, corticosteroids, androgens, and estrogens) [3]. Inside cells, cholesterol modulates various signaling pathways [4, 5], and modifies specific proteins to control protein trafficking [6, 7]. Therefore, the amount and distribution of cholesterol in a living cell is tightly regulated [8-10].

1.1.1 Cholesterol synthesis, uptake, and efflux

Mammalian cells have two major sources of cholesterol: *de novo* synthesis and uptake of low-density lipoprotein (LDL). Cholesterol is synthesized through mevalonate pathway [11], which starts with acetyl CoA. The rate-limiting step in this process is 3-hydroxy-3-methylglutaryl coenzyme A (HMG-CoA) reductase, which is a membrane protein located in the ER. Exogenous cholesterol mainly comes from LDL. Cells uptake LDL through LDL receptors via receptor-mediated endocytosis [12]. Cholesterol is then released from lysosomes to be transported to ER or plasma membrane [9]. Finally, cholesterol efflux is an essential process occurs either by passive diffusion or active pathways mediated by ATP-binding cassette (ABC) transporters (e.g. ABCA1, ABCG1) [13]. High-density lipoprotein (HDL) acts as the major acceptor for cellular cholesterol efflux, which serves as an important vehicle to transport excess cellular cholesterol to liver for recycle and excretion [9]. Overall, these processes modulate total cholesterol levels inside cells.

1.1.2 Intracellular cholesterol trafficking

Location of cholesterol is one of major factors that regulate the fate of cholesterol [10]. Therefore, cholesterol trafficking is tightly controlled [14]. Once cholesterol is synthesized in ER, it leaves ER rapidly to be transported to plasma membrane through a non-vesicular trafficking process [15-17]. Some studies have shown that this process is dependent on caveolin-1 [18, 19]. Other lipid-binding proteins, such as oxysterol binding protein-related proteins (ORPs) [20] and StAR-related lipid transfer (START) domain containing proteins [21] may also be involved in this process.

On the other hand, the exogenous cholesterol obtained from LDL uptake goes through endocytic pathway [12]. After LDL uptake, CE in LDL is hydrolyzed in a hydrolytic compartment [22], after which moves to the late endosome/lysosome. Then the cholesterol from LDL is exported out of lysosomes, which is facilitated by Niemann-Pick types C1 (NPC1) and C2 (NPC2) proteins [23]. These cholesterols are transported to plasma membrane or ER [22]. In ER, cholesterol is re-esterified and stored in lipid droplets (LDs). ER is also the location where cholesterol modification of protein occurs [24]. Alternatively, cholesterol in late endosome/lysosome can be transported to other organelles by Rab9-dependent vesicular trafficking process [9, 10]. Rab9 is a small GTPase, which plays important roles in vesicular trafficking between late endosomes and the Golgi network [25].

Steroidogenesis happens in mitochondria. Cholesterol transport to inner mitochondrial membrane is the rate-limiting step in steroidogenesis [26, 27], which involves steroidogenesis acute regulatory protein (StAR) and peripheral benzodiazepine receptor (PBR) [28]. StAR contains a sequence to target the protein to enter mitochondria [29, 30], whereas PBR is outer mitochondrial membrane protein working as a cholesterol recognition site [31].

1.1.3 Cholesterol homeostasis

Although it is an essential lipid in mammalian cells, excess cholesterol causes cytotoxicity [32]. High level of intracellular free cholesterol has been shown to disrupt membrane fluidity and membrane domains [33], which lead to loss of function of certain membrane proteins [34] and altered signaling pathways [32]. Cholesterol crystal is formed when free cholesterol level is very high, and this needle-shaped structure can disrupt organelles [35]. Some oxysterols generated from excess cholesterol are harmful to cells [36, 37]. Other mechanism involves apoptotic pathway induced by free cholesterol overloading [38, 39]. ER stress induced by high level of cholesterol is also found in various metabolic disorders [40]. Therefore, maintaining cholesterol homeostasis is critical for cells.

Cholesterol homeostasis is maintained by sensor proteins through a feedback-regulated manner [41]. There are several different cholesterol sensors on the ER membrane [8]. Scap and HMG CoA reductase contain sterol-sensing domain (SSD) [42-44], which binds to Insigs protein in the

presence of high sterol level. When certain sterols accumulate intracellularly, Insigs binds to HMG CoA reductase to cause rapid degradation of the enzyme, which suppresses sterol synthesis [44, 45]. Scap mediates translocation of sterol regulatory element-binding proteins (SREBPs), a family of transcription factors regulating lipid metabolism [46, 47]. SREBPs are ER membrane proteins in precursor form bound to Scap, and Scap-mediated translocation of SREBPs to Golgi is essential for cleavage of SREBPs into mature form. Mature SREBPs move into nucleus to upregulate target genes. When the sterol level elevates, sterol-induced conformation change of Scap causes binding of Insigs, which prevents Scap from exiting the ER [48]. As a result, SREBPs are retained on the ER membrane in the inactive form.

There are three isoforms of SREBP, SREBP-1a, SREBP-1c, and SREBP-2 [47], which have different specificity. SREBP-1c is involved in fatty acid metabolism, SREBP-2 is involved in cholesterol uptake and synthesis, and SREBP-1a regulates both [49, 50]. Specifically, target genes of SREBP-1c include ATP citrate lyase, acetyl-CoA carboxylase, and fatty acid synthase, fatty acid elongase complex, stearoyl-CoA desaturase 1 (SCD1) [51, 52], glycerol-3-phosphate acyltransferase [47]. SREBP-2 is shown to upregulate LDL receptor, HMG-CoA reductase, farnesyl diphosphate synthase, and squalene synthase [47]. In addition to the cleavage of SREBP precursor, SREBPs are also regulated in transcriptional and post-translational levels [53].

Another regulator of cholesterol homeostasis is liver X receptor (LXR). It is a transcription factor consists of two isoforms, LXRα and LXRβ. While LXRα is expressed mainly in spleen, pituitary, lung, liver and fat, LXRβ is expressed ubiquitously [54]. LXRs form heterodimers with retinoid X receptor (RXR) to recruit corepressors and bind to promoters of the target genes [55]. Binding of oxysterols replaces corepressors with coactivators [56, 57], which promotes expression of genes involved in fatty acid metabolism, cholesterol efflux and degradation of LDL receptors. Specifically, its target genes include fatty acid synthase [58], SREBP-1c [59], ABCA1, ABCG1 [60], and Idol [61].

Besides maintaining cholesterol homeostasis through regulation of cholesterol uptake, synthesis, and efflux, another level of regulation comes from esterification and storage of cholesterol into LDs [10, 62]. This process is catalyzed by an ER protein known as acyl-coenzyme A: cholesterol

acyltrasferase (ACAT) [9, 63], with free cholesterol and long-chain fatty acyl coenzyme A as substrates to generate cholesteryl ester (CE). Although ACAT does not contain SSD, its activity is regulated through allosteric activation by sterols, preferably cholesterol [64, 65]. By converting cholesterol into CE, cells can effectively reduce free cholesterol level in the ER membrane, reducing the cytotoxicity.

Disruption of cholesterol homeostasis is associated with many diseases, including atherosclerosis [32], metabolic diseases [66], and cancer [67]. Atherosclerosis is caused by building up of plaque that clog arteries. One of the major risk factors of this disease is increased serum cholesterol [68], and massive accumulation of CE in macrophage foam cell is a hallmark of early atherosclerotic lesion [69]. As the lesions become more advanced, free cholesterol content increases at the lesions [70], indicating the disruption of cholesterol homeostasis during the disease progression. There are several metabolic diseases that results from defects in genes involved in cholesterol metabolism. Some of them are caused by alteration in the cholesterol synthesis pathway, such as Smith-Lemli-Opitz syndrome [71]. In these disorders, intermediate metabolites are accumulated due to defects in one of enzymes in the cholesterol biosynthesis pathway. Niemann-Pick type C (NP-C) disease is an autosomal recessive lysosomal storage disorder caused by defects in cholesterol trafficking [72]. Mutations in NPC1 or NPC2 genes results in accumulation of free cholesterol in late endosome/lysosome, which cause neurodegeneration [73]. Tangier disease is another disorder caused by mutations in ABCA1 [74]. In addition to these metabolic diseases, altered cholesterol metabolism is found in various cancers [67], which is discussed in the next section.

1.2 Cholesterol metabolism in cancer

Cholesterol accumulation in tumor was found as early as in 1900s [75]. Since then, many studies further show evidence supporting the important roles of cholesterol in cancer development [67]. Based on several epidemiological studies, there is a positive correlation between increased serum cholesterol and risk for certain types of cancer, such as prostate cancer [76, 77]. The interests in understanding the functions of cholesterol and utilizing it as a therapeutic target have further increased when the association between statin, a class of cholesterol synthesis inhibitors, and reduced cancer risk was observed [78]. However, there are also studies indicating no association

between cholesterol and cancer progression [79-82]. These controversial results indicate that the link between cholesterol and cancer is complex.

Despite the controversy from the epidemiological studies, preclinical studies show more consistent association between high cholesterol and cancer development. For example, cholesterol is shown to promote formation of more aggressive tumor in the breast cancer mouse model [83]. Furthermore, increased cholesterol synthesis and membrane cholesterol level contribute to progression of $HER2^+$ breast cancer to more a malignant phenotype [84]. More recently, by analysis of The Cancer Genome Atlas (TCGA) database [85], alteration in cholesterol pathway in tumor cells was correlated with cancer patient survival [67]. These studies indicate the important roles of intracellular cholesterol in cancer cells. Indeed, multiple oncogenic pathways regulate cholesterol metabolism in cancer. PI3K/Akt pathway enhances cholesterol levels in cancer by increasing cholesterol synthesis, uptake and suppressing cholesterol export [86, 87]. Activation of PI3K/Akt pathway also promotes cholesterol esterification, resulting accumulation of CE in LDs in prostate cancer cells [88]. PKB/Akt promotes cholesterol and fatty acid biosynthesis, which promotes synthesis of membrane [89]. Spleen tyrosine kinase/PI3K pathway promotes cholesterol synthesis to maintain the activity of B cell receptor signaling in lipid rafts [89]. Mutant p53 proteins promotes cancer progression by upregulating mevalonate pathway [90].

Given the essential roles of cholesterol in maintaining cell structure and serving as a precursor for various signaling molecules, it is hypothesized that increased cholesterol promotes cell proliferation and survival in various cancer [67]. One mechanism is that increased intracellular cholesterol level provides membrane components for the formation of lipid rafts [91-93]. In addition to plasma membrane, cholesterol content in mitochondrial membrane has an important impact on cancer cell survival. For example, decreased ABCA1 activity in colorectal cancer promotes cancer cell survival by increasing mitochondrial cholesterol levels [94]. In hepatocellular carcinoma, mitochondrial cholesterol increases the mitochondrial membrane order, which contributes to obtaining resistance to chemotherapy [95]. Another mechanism involves regulation of oncogenic pathways by cholesterol. For example, myristoylated Akt is sensitive to membrane cholesterol levels, and it requires localization to the cholesterol-rich membrane microdomains to exert its oncogenic functions [96]. Mevalonate pathway was also shown to regulate Hippo pathway

to promote proliferation and self-renewal of breast cancer cells [97]. Cholesterol modification of hedgehog protein [6, 98] is essential for distribution and activity of hedgehog pathway, an essential pathway that promotes carcinogenesis [99]. Regulation of cell cycle is another important aspect in cancer cell proliferation. It has been demonstrated that cholesterol is required in the G2-M phase of cell cycle [100]. In another study, prohibitin was identified as a cholesterol-sensitive cell cycle regulator which protects prostate cancer from apoptosis [101]. Finally, being a precursor for steroidogenesis, accumulation of cholesterol in prostate cancer has been proposed to promote androgen synthesis in tumor which leads to development of castration-resistant prostate cancer [102-104]. Overall, abnormal cholesterol metabolism plays an important role in cancer development.

Cholesterol synthesis pathway has been tested for its anti-cancer activities. Statins (HMGCoA reductase inhibitor), and oxidosqualene cyclase inhibitor reduce tumor growth and metastasis [105, 106]. Blocking exogenous cholesterol source by inhibiting LDL receptor, in combination with chemotherapy, suppresses pancreatic cancer progression [107]. At the same time, formulation of anti-cancer drugs into LDL or LDL-like structures shows a potential to enhance drug targeting and delivery to cancer cells [108]. Suppressing cholesterol storage in cancer cells by inhibiting ACAT has been shown to suppress tumor growth in prostate [88], pancreatic [109], lung and colon cancers [110]. More recently, targeting cholesterol transport pathway was proposed suppress cancer cell survival [111].

In summary, it is becoming clear that deregulation of cholesterol metabolism contributes to cancer development. Despite the controversial epidemiological studies, preclinical studies demonstrate important and complex roles of cholesterol in multiple types of cancer. Given the complexity of cholesterol regulation, deeper understanding of molecular pathways and consequences of aberrant cholesterol metabolism in cancer is needed to further strengthen the link between cholesterol and cancer development.

1.3 Conventional analytical tools for tracking cholesterol

There are several different ways to study level, localization and trafficking of cholesterol in cells or tissues. These techniques utilize reporter molecules which can be divided into two major

categories: cholesterol binding molecules and cholesterol analogs [112]. Cholesterol binding molecules are generally used to quantify the levels of cholesterol or study steady state distribution of cholesterol. Fluorometric or colorimetric assays based on cholesterol oxidase, sometimes in combination with cholesterol esterase, are widely used to quantify total cholesterol, free cholesterol and esterified cholesterol in homogenized samples [113]. However, these assays do not provide spatial information. Filipin is a commonly used fluorescent cholesterol binding molecule that can form complex with free cholesterol and visualize distribution of free cholesterol in fixed cells [114]. Another type of cholesterol binding molecule is perfringolysin O derivatives [115]. These molecules are shown to have high affinity to free cholesterol and can effectively label cholesterol-rich domains at the plasma membrane without fixation or in the intracellular structures with fixation [116].

As cholesterol distribution is an important factor that determines the fate and physiological functions of cholesterol, visualizing cholesterol and tracking its dynamics are essential. Unfortunately, cholesterol is a small lipid, which is difficult to label and track in real-time. Radioactive cholesterol or its precursor is used in biochemical studies aiming to understand cholesterol trafficking and metabolism [112]. Although this approach provides high sensitivity and specificity, it has to be used in combination with separation methods to determine intracellular distribution of cholesterol. Imaging approaches using cholesterol analogs enables real-time tracking of cholesterol dynamics and provides more accurate spatial information. To image cholesterol, various fluorescent cholesterol analogs were developed. Dehydroergosterol (DHE) is an intrinsic fluorescent sterol, which structurally is slightly different from cholesterol. DHE has been shown to closely mimic the cholesterol physiology [117]. Unfortunately, its fluorescent property is not optimal due to rapid photo-bleaching and strong overlapping signals from autofluorescence in tissues or in organisms [112, 118]. Other fluorescent cholesterol analogs include fluorophore tagged cholesterol molecules such as 7-nitrobenz-2-oxa-1,3-diazole (NBD)-cholesterol and boron dipyrromethene difluoride (BODIPY)-cholesterol [119, 120]. These molecules have more favorable fluorescent properties, but large fluorophore group often interfere with function of cholesterol [121]. Lastly, clickable cholesterol analogs were developed and used to study cholesterol-binding proteins [122, 123]. These molecules contain small tag, which minimize the perturbation, but it requires additional steps before fluorescence imaging.

As demonstrated in this section, there are many reporter molecules developed to study cholesterol transportation and metabolism, indicating the importance of understanding cholesterol dynamics in real-time. At the same time, it is still challenging to study cholesterol in living cells and organism with the current methods due to the abovementioned difficulties, further stressing the need for developing new techniques for imaging cholesterol in a living system.

1.4 Stimulated Raman scattering imaging of living cells

The work presented in this section was published in *Methods* [124]. Reprinted with permission from [124].

A central theme of chemical science is deciphering how molecules function in a complex system, such as a living cell. Such study contributes to the society by providing fundamental knowledge in medical science to improve our lives. Yet, our understanding of chemistry in living system (e.g., how intensive biosynthetic chemical activity drives cell development, function, and inter-cellular communications) is still limited, partly because conventional biochemical assays treat the cell, a highly dynamic structure, as a static bag of molecules. In current paradigms, molecules are extracted from a tissue and analyzed by various analytical techniques such as immunoblotting and liquid chromatography/mass spectrometry. These *in vitro* assays provide very little information about the spatial distribution or temporal dynamics of molecules in real life, thus they are unable to tell the exact roles of molecular activities on cellular functions [125]. Furthermore, the molecular profile of a cell may alter during the extensive sample processing procedures. For *in situ* imaging, fluorescent microscopy is widely used. By measuring fluorescent signals from endogenous species, such as coenzymes nicotinamide adenine dinucleotide (NADH) and Flavin adenine dinucleotide (FAD), cell metabolism can be measured in real time [126-128]. Unfortunately, not all endogenous molecules possess the ideal optical properties. Fluorescent labels allow imaging of proteins and some key metabolites in living cells, but they often disturb the function of small biomolecules, such as glucose and cholesterol, limiting the ability to monitor their activities. These limitations stress the critical need of establishing new platforms for learning chemistry in situ in living systems.

Raman-scattering based vibrational spectroscopy has been a powerful tool for non-invasive, label-free analysis of chemicals. Raman scattering is an inelastic scattering process, in which an excitation photon loses energy to a certain molecular vibration mode, resulting a scattered photon with a different wavelength. Such energy losses are directly related to vibrational transitions of a molecule, showing as peaks in Raman spectrum (**Figure 1.1A**). Therefore, analysis of Raman-scattered photons can be used to identify chemical species quantitatively. Raman microscope, which is now commercially available, allows chemical imaging with submicron spatial resolution [125].

However, because Raman scattering is a feeble process, the image acquisition speed of current Raman microscopes (at least tens of minutes per frame) is insufficient to follow chemical dynamics in vivo. To improve the imaging speed, line illumination has been adopted for ultra-fast Raman imaging, allowing several minutes per frame imaging speed (Nanophoton, Osaka, Japan). To overcome the speed limitation, coherent Raman scattering (CRS) microscopy [129] has been developed to enhance the Raman signal level. In CRS microscopy, two excitation beams, known as pump (ω_p) and Stokes (ω_s), are used. When the laser-beating frequency ($\omega_p - \omega_s$) is in resonance with a molecular vibration frequency (Ω), four major CRS processes occur simultaneously, known as coherent anti-Stokes Raman scattering (CARS), coherent Stokes Raman scattering, stimulated Raman gain (SRG), and stimulated Raman loss (SRL) (**Figure 1.1B**). These nonlinear optical processes offer a large signal that allows live-cell imaging at a speed three to four orders of magnitude faster than Raman microscope. As nonlinear optical process, CARS and SRS microscopy offers inherent three-dimensional (3D) sectioning capability. Furthermore, because CRS microscopy uses near infrared light for excitation, it induces minimal photodamage to cells.

CARS is a four-wave mixing process in which the signal is generated at a higher frequency (**Figure 1.1B**). CARS signal consists of a non-resonant part independent of the beating frequency and a resonant part depending on the beating frequency. The non-resonant background part is contributed by electronic motions [130, 131]. SRG and SRL belong to stimulated Raman scattering (SRS) [132]. It is a dissipative process accompanied by intensity increase in the Stokes beam and intensity decrease in the pump beam when the energy difference between the two beams pumps the molecule from a ground state to a vibrationally excited state (**Figure 1.1B**). Because SRG and

SRL signals appear at the same frequency as the incident beams, optical modulation and demodulation are used to extract those signals. In contrast to CARS, SRS signal is free of non-resonant background, spectral distortion, and is linearly dependent on molecular concentration. These advantages allow SRS microscopy to study lipids, proteins, nucleic acids, glucose, and other metabolites in living cells and organisms via quantitative chemical imaging with high sensitivity [133, 134]. In accordance with the rapid development of SRS microscopy field, there is number of reviews on application of SRS imaging in living cells and/or biomedical research [135-140]. In this section, we discuss different SRS imaging modalities and their applications to study chemical content, transport, and reaction in biological samples.

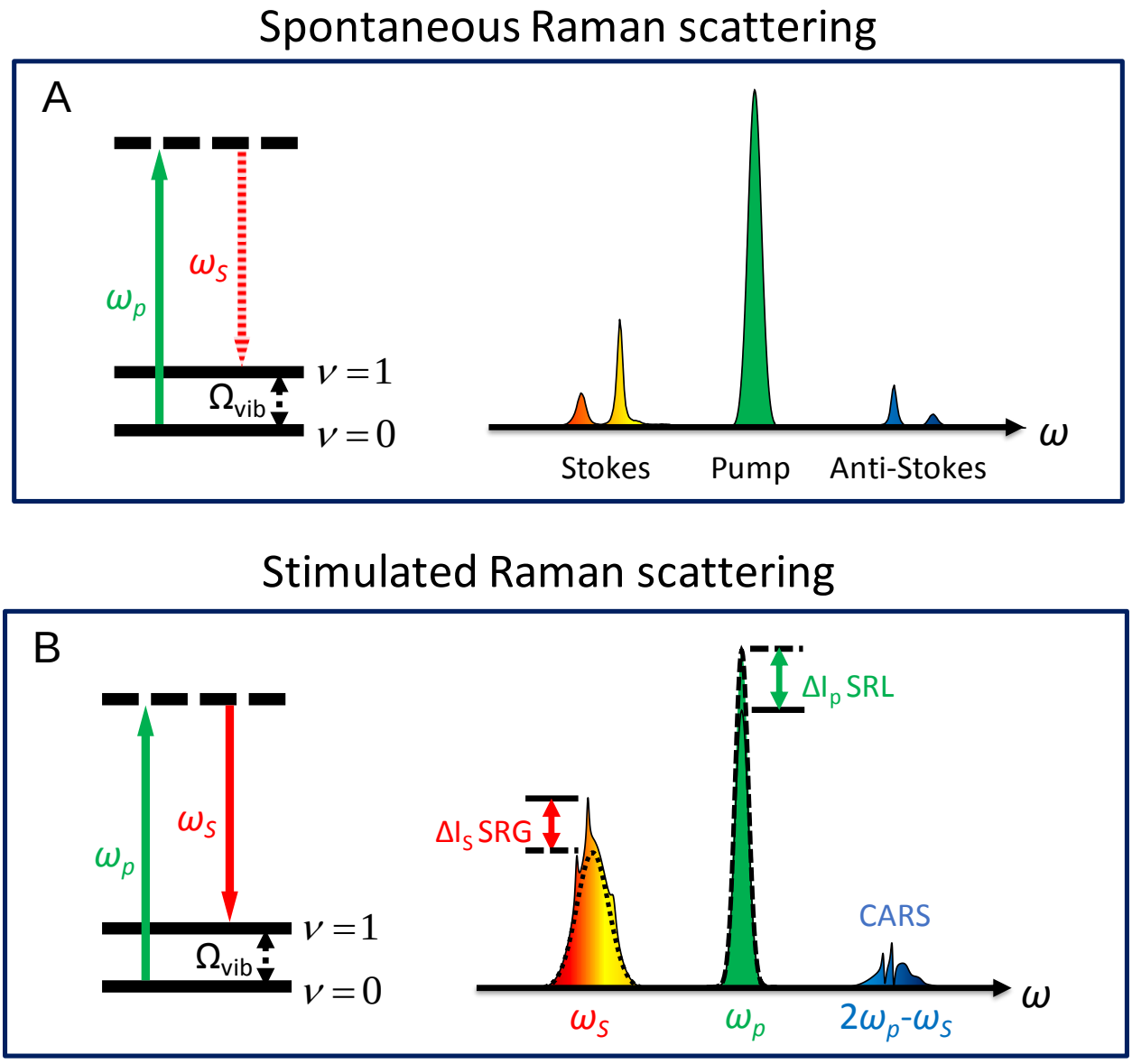

Figure 1.1 Spontaneous and coherent Raman scattering processes.
(A) Energy diagram of spontaneous Raman scattering and representative spectra. (B) Energy diagram of SRS and CARS processes and representative spectra. Broadband coherent Raman scattering induced by a pump field at ω_p and a Stokes field at ω_S. Solid arrows indicates laser excitation and dashed arrow indicates the spontaneous scattering process Ω_{vib} denotes the vibrational energy.

1.4.1 SRS imaging modalities

Key components of a SRS microscope include a two-color laser source, an optical modulator, a laser scanner, a detector and an electronic demodulator (**Figure 1.2**). Below we will review recently developed approaches of constructing a SRS microscope.

1.4.1.1 Single-frequency SRS imaging

In single-frequency SRS imaging scheme, the laser energy is focused to a specific Raman mode of typical bandwidth around 10 – 100 cm^{-1}. To achieve high spectral resolution, picosecond laser is preferred, especially for imaging narrow Raman bands. At the same time, picosecond excitation reduces cross-phase modulation background and photodamage. However, SRS is a nonlinear process, which requires high peak power to generate signals, and the signal level can be increased by more than one order using femtosecond laser [141]. Moreover, femtosecond excitation is preferred when the SRS microscope is coupled with other widely used imaging modalities, such as two-photon excitation fluorescence (TPEF), second harmonic generation, and third harmonic generation. Several laser sources were developed for SRS imaging: (1) electronically synchronized, mode-locked Ti:sapphire lasers which produce mode-locked pulse trains with a repetition rate of ~80 MHz and pulse duration from several picoseconds to 100 femtoseconds [142], (2) a mode-locked picosecond Nd:YVO4 laser at 1064 nm that synchronously pumps a second beam through optical parametric oscillator (OPO) [143], (3) a femtosecond Ti:sapphire laser with an OPO [144].

SRS signal appears at the same frequency as one of the excitation beams. To extract the signal, optical modulation and demodulation are used. Pump or Stokes beam is modulated at megahertz frequency using acousto-optic modulator (AOM) or electro-optic modulator (EOM). These two synchronized laser pulses are spatially overlapped and coupled into a laser scanning microscope. A high numeric aperture objective lens is used for tight focusing. Oil condenser is used to suppress background from cross-phase modulation by enhancing the signal collection efficiency [145]. A photodiode is used for the detector, which can withstand high laser power at milliwatt level. SRL or SRG signal is extracted with a demodulator, such as a lock-in amplifier. As a cost-effective alternative, a tuned amplifier that resonates at the modulation frequency can also be used as a demodulator [146]. Various SRS imaging setups have been demonstrated based on the abovementioned methods.

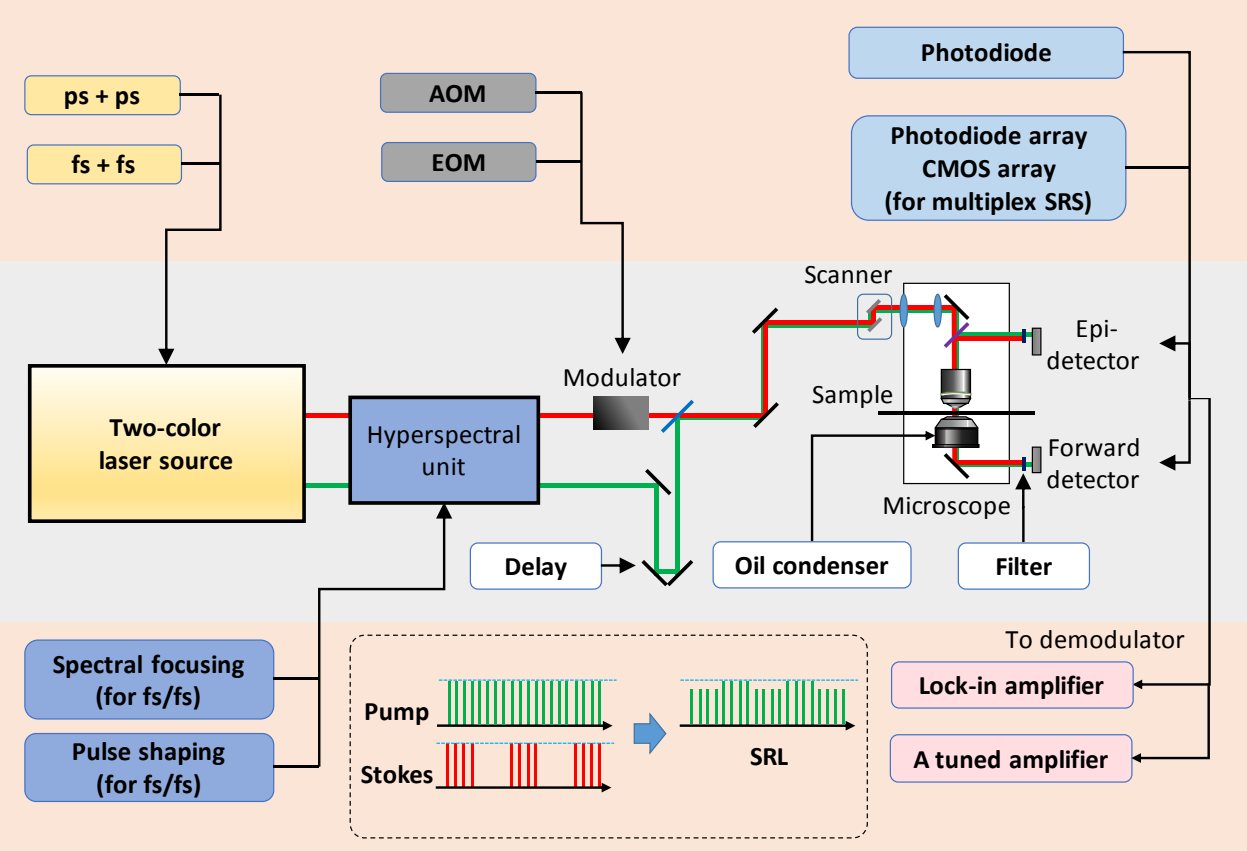

Figure 1.2 Instrumentation of SRS microscopy.
Insert: Schematic of the pulse trains in the stimulated Raman loss. OPO, optical parametric oscillator; AOM, acousto-optic modulator; EOM, electro-optic modulator; CMOS, complementary metal-oxide-semiconductor.

1.4.1.2 Frame-by-frame hyperspectral SRS imaging

Single-frequency SRS imaging provides real-time chemical imaging based on isolated Raman bands. However, it is difficult to distinguish spectrally overlapped Raman bands. Hyperspectral SRS microscopy offers better chemical specificity. Frame-by-frame hyperspectral SRS imaging records a stack of SRS images at multiple Raman shifts. Wavelength scanning is a straightforward method for hyperspectral SRS imaging. Using two tunable picosecond lasers, the wavelength is tuned over a continuous range to cover multiple Raman shifts [147, 148]. The fastest spectral tuning approach can resolve more than 50 spectrally-distinct frames in ~10 min.

With the broad bandwidth, femtosecond lasers can be used for hyperspectral SRS imaging in multiple ways. A relatively simple and robust method utilizes spectral focusing technique [149,

150]. In this approach, two femtosecond laser beams are chirped with NSF57 glass to picosecond range, which improves spectral resolution [151]. By tuning the time delay between the two chirped pulses, the frequency difference is subsequently changed to excite different Raman shifts. With this approach, hyperspectral SRS images can be recorded within a minute over a ~270 cm^{-1} spectral window. The important optimization parameters for this method are linear chirping and alignment of beams and calibration of Raman shift. Another approach uses a pulse shaper to filter and scan a narrow spectral component out of a broadband femtosecond spectrum [152-154]. Using spectral filtering coupled with a customized fiber amplifier, a hyperspectral SRS imaging of spectral resolution better than 10 cm^{-1} can be reached [155].

1.4.1.3 Multiplex SRS imaging

Hyperspectral SRS imaging generally takes seconds to minutes to obtain the hyperspectral SRS image stacks. This acquisition speed causes spectral and spatial distortions when imaging dynamic process happening in vivo. Multiplex SRS microscopy was developed to provides high-speed high-content biological imaging. Multiple Raman bands can be detected simultaneously in the spectral domain or in the time domain. The main requirement for multiplex SRS microscopy in spectral domain is parallel detection of dispersed SRS signals. The detection using a photodiode array has been demonstrated by Marx et al [156]. To extract the signal, demodulators are required, such as a high-frequency lock-in amplifier. Lu et al. used three independent lock-in amplifiers to demonstrate multicolor SRS imaging [157]. A multichannel lock-in amplifier has been developed for 128-channel multiplex SRS microscopy [158]. Resonant amplifiers[146] provide cost-effective approach for multiplex detection, and by designing a 32-channel tuned-amplifier array integrated with a photodiode array, Liao et al. significantly reduced the spectral acquisition time to 32 µs with a spectral window of ~200 cm^{-1} [159].

Another approach in time domain utilizes frequency coding. In this approach, each photon is modulated at certain frequency, which is then collected by a single detector. The spectral information is extracted by demodulating at different frequencies. Fu et al. [160] demonstrated parallel detection of three-color SRS imaging by modulating each color of the excitation laser with an acousto-optical tunable filter at a specific kilohertz-rate frequency. Megahertz-rate modulation

has been demonstrated by scanning dispersed excitation beam on a spatial pattern inside a femtosecond pulse shaper, achieving a spectral acquisition within 60 μs per pixel [161].

1.4.1.4 Image analysis

Hyperspectral SRS microscopy generates x-y-Ω image stacks. By extracting spectral profile at each pixel, concentration maps of different species can be generated. Several imaging processing methods are available for analyzing hyperspectral SRS image stacks, including principle component analysis (PCA) [149], multivariate curve resolution (MCR) [152], and spectral phasor analysis [162]. PCA is used to determine the number of principle components in the hyperspectral image stack. MCR analysis is a widely-applied method to analyze hyperspectral SRS images [152, 163, 164]. It decomposes the SRS image stack into concentration profiles (matrix C) and spectra of each component (ST). The dataset D and the reference spectra of each component are entered in the model $D = C \cdot ST + E$, in which S contains the output spectra of all fitted components, and T is the transpose of matrix S. E is the residual matrix or experimental error. Initial estimate of pure spectra can be obtained from PCA, k-means clustering or prior knowledge of the sample, and with this information, an alternating least squares algorithm calculates C and S iteratively until optimal fit to the data matrix D is achieved. The output is a concentration map for every principle component, expressed as a percentage relative to the intensity of the MCR-optimized spectrum.

1.4.2 Imaging chemistry in cells and tissues by label-free SRS microscopy

Label-free SRS imaging has been applied to in vivo imaging of mouse skin [132, 159-161, 165], brain [166], *Caenorhabditis elegans* (*C. elegans*) [163, 167, 168], *Drosophila* [169, 170], tadpoles [171], and human cancer tissues [88, 172, 173]. C-H bond is the most abundant chemical bond in living cells, providing chemical information of molecules, such as lipids and proteins. Compared to C-H region where multiple C-H stretching bands are highly crowded and spectrally overlapped, fingerprint region (500 – 1800 cm^{-1}) is used to provide better chemical specificity for imaging of nucleic acids, metabolites, and drugs. Below we will review applications of SRS imaging to study chemical content, dynamics and functions in living cells, tissues, and human samples.

1.4.2.1 Mapping chemical content in cells and tissues.

Altered lipid metabolism is recognized as a signature of various types of human cancer. Although intracellular lipid accumulation has been observed in human cancer tissues and cells, it has not been widely used as a prognostic factor or therapeutic target due to limited understanding of lipid metabolism in cancer. In particular, the role of lipid accumulation in cancer progression remains elusive partly because lack of tool for mapping lipid species in a single-cell level. Quantitative analysis of lipid content at single-cell level in human patient cancerous tissue by coupling confocal Raman microscopy with SRS microscopy enabled identification of metabolic signature of aggressive human prostate cancer [88]. The spectroscopic imaging data revealed aberrant accumulation of CE in LDs of high-grade prostate cancer and metastases, which was shown to be a consequence of loss of tumor suppressor PTEN and subsequent activation of PI3K/AKT pathway in prostate cancer cells. Depleting CE storage significantly suppressed tumor growth in mouse xenograft models and impaired cancer invasion [88]. This work opens opportunities for using altered cholesterol metabolism for prostate cancer diagnosis and treatment. Recently, by hyperspectral SRS imaging of single living cells, Li et al. [172] identified lipid unsaturation level as a metabolic marker for ovarian cancer stem cells. By analysis of ratio between 3002 cm^{-1} and 2900 cm^{-1} from the hyperspectral SRS image-stacks, lipid unsaturation levels were mapped in the individual cells, revealing high unsaturation level in cancer stem cell population. This signature was shown to be directly regulated by NF-κB and inhibiting lipid desaturation effectively eliminated cancer stem cells, which blocked tumor initiation capability *in vivo* [172]. This work demonstrates the importance of single-cell chemical imaging, which enabled label-free identification of rare and the most malignant population of cancer cells and cancer stem cell-specific therapy.

At the tissue level, *in situ* mapping of chemical content allowed visualization of cholesterol crystals, lipids, proteins, and nucleic acids. By separating sterol C=C band at 1669 cm^{-1}, acyl C=C band 1655 cm^{-1} and broad amide I band, the distribution of cholesterol crystals, lipids and proteins were mapped in an intact atherosclerotic arterial tissue [174]. CH_2 and CH_3 stretching modes represent major components of lipid and protein, respectively, and are used to map these two compositions in fresh mouse ear skin [157] and *ex vivo* mouse skin tissue [160]. Nucleic acid has signature

Raman peaks at 785 cm^{-1} and 1090 cm^{-1}, which was used to study the distribution of nucleic acid in mammalian cells and single salivary gland cells of *Drosophila* larvae [170].

For medical application, label-free histology by SRS imaging demonstrates one of the important translational applications of this imaging platform [161, 166, 173, 175]. Histopathology is a standard examination for diagnosis. However, the current techniques require the tissues to be frozen or fixed and stained with dyes before they can be observed, which is label-intensive and time-consuming. By analysis of SRS images at 2850 cm^{-1} and 2930 cm^{-1} for CH_2 and CH_3 vibration modes, Freudiger et al. [175] showed stain-free histopathological imaging of fresh tissue, which is comparable to a hematoxylin and eosin (H&E) staining. Using this approach, *in vivo* SRS imaging of mouse brain after craniotomy was performed to locate brain tumor margin [166]. More recently, Lu et al.[173] profiled a range of human brain tumors from patients to establish hallmarks for glioma classification. Owing to the sharp contrast between lipids and proteins provided by SRS imaging, vascular proliferation, red blood cells and necrosis were easily discriminated. Moreover, marked alteration of myelinated fibers observed using SRS imaging of fresh oligodendroglioma suggested a new mechanism for tumor to modify microenvironment for adaptive advantage [173]. A recent development of spectrometer-free multiplex SRS microscopy further enabled in situ label-free histological analysis of highly scattered, 5-mm-thick human breast cancer tissues [161]. This work opens opportunities to perform in vivo clinical imaging using label-free SRS microscopy for cancer diagnosis and tumor margin detection during the surgery.

Chemical mapping in model organisms such as *C. elegans* has been widely applied to study metabolic process. Identifying genetic regulators of fat storage has been challenging due to controversies of the visualization tool for lipids [176, 177] and complication from quantification of fluorescence labeling and dye-incorporation into lipids in the organisms. Owing to high peak power, femtosecond excitation was used to increase the SRS signal level and performed label-free 3D sectioning of *C. elegans* to distinguish fat storage from membrane lipids [141]. SRS imaging platform has also been combined with RNAi screening to discover novel genetic regulators of fat storage in *C. elegans* [168]. Mapping chemical content in *C. elegans* by hyperspectral SRS imaging further provided label-free approach to distinguish intracellular compartments, including fat droplets, lysosome-related organelles, oxidized lipids, and proteins [163]. By examining

spectral profiles in the fingerprint regions using k-means clustering and MCR analysis, the degree of lipid unsaturation and oxidation and cholesterol storage were mapped in the entire worm. This study demonstrates the potential of applying hyperspectral SRS imaging to understand how lipid storage change in response to diet and the role of insulin in obesity, diabetes and longevity in animals.

1.4.2.2 Monitoring molecular transport in cells and tissues.

One advantage of label-free imaging is the capability of quantitative long-duration imaging. This is especially important when studying the dynamics and tracking changes of biomolecules during ongoing processes, such as embryonic development and injury. Dou et al. [169] performed time-lapse SRS imaging of developing *Drosophila* embryo to track single LD motion within large populations of droplets. By analysis of velocity and turning frequency of each droplet, the mathematical model for the LD movement was developed to show key regulatory point of LD dynamics in the developmental process. [169]. This work shows a potential of using SRS imaging technique to study lipid trafficking in living cells and organisms. More recently, by *in vivo* SRS imaging of single neurons and myelin in the spinal cord, Hu et al. [171] monitored myelin sheath formation, maturation of a node of Ranvier and myelin degradation in live *Xenopus Laevis* tadpole.

Dynamic information is especially important in the study of drug molecules in living systems because the treatment efficiency is highly dependent on the delivery of drug to the target locations. Several chemical signatures of drug molecules have been used to track drug penetration to skin and drug release inside living cells. Fu et al. characterized chemical signature of a tyrosine-kinase inhibitors, which is used for cancer therapy, to image intracellular distribution. The direct visualization of drug in living cells allowed evaluation of lysosome accusation and release of drug [150]. Others have demonstrated the tracking of drug molecules penetrating mouse or human skins using in vivo SRS imaging [132, 165]. By focusing at S=O and C=C bonds, mouse skin uptake of dimethyl sulfoxide (DMSO) and retinoic acid was imaged. More recently, owing to fast spectral acquisition speed, multiplex SRS imaging allowed visualization of DMSO drug diffusion through mouse skin tissues in real-time, revealing fast dynamic diffusion process without spectral distortion from the motions of the animal [159]. This is not easily achieved using frame-by-frame hyperspectral SRS imaging. Liao et al. demonstrated in vivo SRS imaging of vitamin E distribution

on mouse skin by multiplexed modulation at megahertz rate and spectral acquisition within 60 µs per pixel [161].

1.4.2.3 Probing chemical reaction in cells and tissues.

Metabolic conversion is a dynamic process that happens in living cells and tissues all the time, yet, the most adopted methods for measuring metabolism is though *in vitro* analysis of cell or tissue homogenates. High-speed SRS imaging platform opens the possibility to monitor metabolic conversions in real-time by probing chemical reactions *in situ*. By compositional mapping of LDs in single living cells at the speed of 32 microseconds using multiplex SRS microscopy, intracellular metabolic conversion of retinoic acids into retinol was monitored in living cells [159]. By developing hyperspectral SRS microscopy with high spectral resolution (9 cm^{-1}) and submicrometer spatial resolution, aromatic ring of lignin, aldehyde, and alcohol groups in lignified plant cell walls were spectrally and spatially separated [164]. By analysis of hyperspectral images with multivariate curve resolution, Liu et al performed real-time monitoring of aldehyde reduction to alcohol in an intact plant tissue, which represents the lignin reduction. This work demonstrates the potential of SRS imaging in the understanding of dynamic lignin chemical compositions, which provides a novel technique for enhancing the efficiency of biomass utilization.

1.4.3 Probing chemical activities in living cells by SRS imaging of Raman probes

Molecules in biological samples contain chemical bonds that are spectrally overlapping. In order to study the transport or metabolism of a specific molecule, labeling the molecule of interest is helpful in some cases. Several chemical bonds, such as C-D, C≡C, and C≡N, give Raman signals in the silent region (1800 – 2800 cm^{-1}), which can be used to label specific molecules to track their trafficking and metabolism inside living cells and animals. These Raman tags are small, thus can be used to label small molecules with minimum perturbation of their biological functions, allowing bio-orthogonal chemical imaging in living cells and organisms.

The introduction of deuterium isotope in biological system has the advantage that it is stable without radioactivity and replacing hydrogen with deuterium does not change the molecular structure. Therefore, carbon-deuterium (C-D) bond has been used to label small molecules to study their uptake and metabolism in living cells and organisms. One example of the application of

deuterated metabolite is visualizing de novo lipogenesis in living cells by feeding cells with deuterated glucose [178]. Compared to the currently available glucose analogs, such as 3-O-methylglucose, 2-deoxy-D-glucose and fluoro-deoxyglucose, deuterated glucose can be metabolized by cells following the metabolic pathways, which allowed tracing of glucose to lipogenic fate in live cancer cells. *De novo* protein synthesis is another important process in biology that is visualized using deuterium labels [179, 180]. Supplemented deuterated amino acids in the growth medium metabolically incorporate into translational machineries, providing enriched and specific C-D bond signals for newly synthesized proteins. By comparing with the endogenous protein Raman peak of Amide I band at 1655 cm^{-1} or CH_3 band at 2940 cm^{-1}, protein synthesis or degradation can be mapped in living cells [179]. Moreover, Raman peaks of C-D bonds vary slightly due to the structural differences. Taking advantage of these differences, two-color pulse-chase analysis of protein was designed to image formation of protein aggregates. Moving into *in vivo* imaging, this technique has been demonstrated in live brain tissues, zebrafish embryos and mice fed with deuterated amino acids [180]. In addition to glucose and amino acids, choline, a small molecule for membrane synthesis, neurotransmitter, and signaling pathway, has been imaged in living cells and *C. elegans* after metabolic incorporation of deuterated choline [181].

Lipids contain a number of C-H bonds that can be exchanged into C-D bonds, rendering various lipid species good candidates to be probed with SRS imaging of C-D bonds. Deuterated fatty acids were used to visualize cellular fatty acid uptake and distribution in LDs and membranes [141]. By tracing deuterated saturated and unsaturated fatty acids in *C. elegans* using hyperspectral SRS imaging, Fu et al. identified different fates of these fatty acids upon uptake in the worms [182]. More recently, deuterated cholesterol was delivered into living cells to visualize cholesterol storage in steroidogenic cells [183].

As another important application of SRS imaging of C-D bonds in vivo, drug delivery to skin is studied using deuterated drug applied to animal and human skins. Deuterated DMSO was applied to human skin, and the penetration into the skin was visualized using epi-SRS imaging [165]. In another study, anti-inflammatory drug ketoprofen and ibuprofen was imaged in the mouse ear skin [184]. These studies show the potential of using SRS imaging technique to monitor dermato-pharmacokinetics in live animals and humans.

Although isotope labels provide biocompatible analogs for biological studies, the Raman scattering cross section of C-D bond vibration is relatively small. Alkyne bond (C≡C) has a Raman scattering cross section that is larger than most endogenous chemical bonds [185, 186]. The size of alkyne tag is small compared to a fluorescent dye, making it bio-orthogonal. Direct SRS imaging of a broad spectrum of alkyne-tagged small molecules, including deoxyribonucleosides, ribonucleosides, amino acids, choline, fatty acids and glycan, was demonstrated [186, 187]. The reported SRS detection sensitivity for alkynes is around 200 μM with 100 μs pixel dwell time [186]. By feeding alkyne-tagged glucose to live tumor xenograft and brain tissues, glucose uptake was imaged using SRS imaging of alkyne bonds to study glucose uptake patterns [188]. In addition to biomolecules, alkyne tag has been proven to be an effective approach to image pharmacokinetics *in vivo*. Terbinafine hydrochloride, a FDA approved antifungal drug that contains alkyne bonds, was used to study the delivery of this skin drug to mouse ear tissue to ~ 100 μm depth [186].

Alkyne tag can be modified to further increase SRS signals and reduce cytotoxicity in some cases. Phenyl-diyne tagged cholesterol was designed to assess cholesterol storage in living cells and in *C. elegans* [189]. In this study, distribution of BODIPY-conjugated cholesterol is compared with phenyl-diyne cholesterol, showing that bulky and lipophilic BODIPY tag bypass metabolic process of cholesterol and move directly into LDs, whereas bio-orthogonal phenyl-diyne cholesterol followed cholesterol esterification for storage [189]. It was shown that the Raman cross section of a phenyl-diyne tag is ~15 times higher than an alkyne tag, achieving the SRS detection limit of 30 μM phenyl-diyne cholesterol [189]. It should be noted that chirped femtosecond excitation was used to measure the detection limit of phenyl-diyne bond, whereas picosecond excitation was used to measure the detection limit of alkyne bond. In this study, probe size and SRS signal was carefully evaluated to achieve strong signal and biocompatibility, and the trade-off between these two parameters should be balanced in a case-by-case manner. Collectively, we expect that development of novel Raman tagged bio-orthogonal molecules will lead to better understanding of cellular processes by detecting specific chemical activities *in situ*.

1.4.4 Conclusions and outlook

With the capability of mapping chemical species in living cells and organisms in a label-free manner, SRS microscopy offers a novel platform to study metabolism, trafficking of organelles,

and pharmacokinetics *in vivo*. The integration of SRS microscope and Raman tag provides an innovative strategy to map the metabolic activities of small molecules *in vivo*. We note that there are several limitations and/or disadvantages of current SRS imaging system. Raman scattering signals of endogenous chemical bonds are sometimes weak, resulting in low detection sensitivity. Also, the ability to distinguish chemical species may be compromised when there is no distinguishable vibrational signature due to similarities in chemical bonds. With these considerations in mind, we expect several promising directions in the future. The first direction is development of a broadband SRS microscope using an ultrashort pulse laser as excitation source. By covering the entire fingerprint vibration region, such a system would allow discovery of signatures inside living cells. The second direction is the study of less abundant metabolites enabled by further improving the sensitivity. Along this line, we anticipate novel design of Raman tagged small molecules for dynamic and functional study of biological processes. The third direction is the development of miniature SRS imaging systems, which have the penitential of clinical applications, for example, for diagnosis of cancer margin in the operating room.

2. TARGETING CHOLESTEROL ESTERIFICATION TO SUPPRESS PROSTATE CANCER METASTASIS

The work presented in this chapter has been submitted to *Molecular Cancer Research*.

Dysregulation of cholesterol is a common characteristic of human cancers including prostate cancer. In this study, we observed an aberrant accumulation of CE in metastatic lesions using stimulated Raman spectroscopic analysis of LDs in human prostate cancer patient tissues. Inhibition of cholesterol esterification in prostate cancer cells significantly suppresses the development and growth of metastatic cancer lesions in both orthotopic and intra-cardiac injection mouse models. Gene expression profiling shows that CE depletion suppresses the metastatic potential through upregulation of multiple regulators that negatively impact metastasis. Additionally, Wnt/β-catenin, one of vital pathways for metastasis, is downregulated upon CE depletion. Mechanistically, we found evidence suggesting that inhibition of cholesterol esterification significantly blocks secretion of Wnt3a through reduction of monounsaturated fatty acid levels, which limits Wnt3a acylation. These results collectively validate cholesterol esterification as a novel metabolic target for treating metastatic prostate cancer.

2.1 Introduction

Cholesterol is an essential component of mammalian cells and is tightly regulated at multiple levels [9, 10]. Cells obtain cholesterol from either *de novo* synthesis or uptake of LDL for construction of membrane structures [1, 2], steroidogenesis [3], or modulation of protein trafficking and activity [7]. Cholesterol overloading causes cytotoxicity, and for most cell types, cholesterol efflux is essential for maintaining its homeostasis [13]. Another mechanism for avoiding free cholesterol toxicity is by storing excess cholesterol into LDs. This process involves conversion of cholesterol into CE by ACAT [9, 63]. Cholesterol homeostasis is maintained through a feedback-regulated manner [8] and disruption of this balance is associated with many diseases such as atherosclerosis [68], metabolic diseases [66], and cancers [67]. Analysis of TCGA database demonstrates correlation between cholesterol level and cancer patient survival [67], which supports an important role of abnormal cholesterol metabolism in cancer development. Other studies on mechanisms

have also shown the connection between oncogenic pathway and altered cholesterol metabolism during cancer progression [90, 97].

It was observed several decades ago that cholesterol accumulates in prostate cancer (PCa) [190]. Since then, an increasing number of studies support the indispensable roles of cholesterol in PCa progression [76, 191, 192]. One hypothesis is that the accumulated cholesterol from either *de novo* synthesis or uptake in PCa provides precursor for androgen synthesis within tumor for the development of castration-resistant PCa [102-104]. Another hypothesis is that increased cholesterol level supports prostate cancer growth by providing key membrane components such as lipid rafts [91-93]. Other studies have shown that a certain signaling molecule [96] and cell cycle regulator [101] are sensitive to intracellular cholesterol level. In the meanwhile, suppression of cholesterol efflux pathway in advanced PCa was observed [193], which further supports increased cholesterol level during PCa progression. These extensive studies on functional roles of cholesterol accumulation in PCa regulated by synthesis, uptake and efflux have provided important insights. However, our understanding of cholesterol homeostasis in PCa is incomplete, as another critical aspect of cholesterol metabolism, cholesterol esterification, is relatively understudied. Being an important buffering mechanism for detoxifying excess free cholesterol [10], esterification of cholesterol may be necessary for PCa cells to cope with high intracellular cholesterol level.

We previously showed an aberrant accumulation of CE in LDs inside cancerous lesions by implementing label-free Raman spectroscopic imaging of LDs in human PCa tissues [88]. This accumulation was found to be a result of loss of tumor suppressor PTEN and subsequent activation of PI3K/Akt pathway. Increased LDL uptake is the major source of such accumulation. Depleting CE by ACAT inhibition reduces PCa proliferation and growth in a mouse xenograft model [88]. This study serves as a foundation for developing a therapeutic approach using ACAT as a target. Nevertheless, it remains unclear what kind of role CE accumulation plays in PCa metastasis and whether metastasis can be suppressed through CE depletion. Notably, early-stage PCa is often treated successfully, but late-stage PCa, where cancers have been spread to distant lymph nodes, bones, or other organs, has a five-year survival rate as low as 29% [194], making metastasis the major cause of PCa mortality in men. Given that there is currently no effective treatment for this

disease [195], a deeper understanding into the role of cholesterol esterification in PCa metastasis would be valuable to the development of novel treatment approaches for metastatic PCa.

In this study, we reveal that CE accumulation is a metabolic signature of human metastatic PCa. We further demonstrate the suppression of both development and growth of metastatic PCa by inhibiting cholesterol esterification in an orthotopic mouse model and an intra-cardiac injection model. Through gene expression profiling, we identified downregulation of Wnt/β-catenin pathway after CE depletion, confirmed by β-catenin protein levels and distribution in PCa cells. We further show evidence supporting that CE depletion lowers fatty acid availability for Wnt3a acylation, which is essential for Wnt-mediated cell migration. These results collectively support that inhibiting cholesterol esterification suppresses PCa metastasis through impairing Wnt/β-catenin signaling, which opens a new opportunity for treating metastatic PCa.

2.2 Experimental section

2.2.1 Human metastatic PCa tissue specimens and cell lines

The study of human patient specimens was approved by the institutional review board at Purdue University. Frozen specimens of human metastatic PCa tissues obtained by warm body autopsy from patients who had failed hormone therapy were obtained from Johns Hopkins Hospital. SRS imaging and confocal Raman spectroscopy was performed on these tissue slices (~20 μm) without any processing or labeling.

Cell lines were obtained from American Type Culture Collection (ATCC). PC-3M cell line was obtained from M.D. Anderson Cancer Center Characterized Cell Line Core. RPMI 1640, F-12K, non-essential amino acids (NEAA) were purchased from Life Technologies. EMEM was purchased from ATCC. Fetal bovine serum (FBS) was purchased from Atlanta Biologicals. Cells were cultured in the following media: PC-3M in RPMI 1640 supplemented with 10% FBS and 0.1 mM NEAA, PC-3 in F-12K supplemented with 10% FBS, LNCaP-HP was derived upon continuous passage from original LNCaP (ATCC) in RPMI 1640 supplemented with 10% FBS until the passage number was over 81 following the procedure reported [196-199], DU145 PTEN-

KD cell line in EMEM supplemented with 10% FBS and 5 μg/mL puromycin (Life technologies). All cells were cultured at 37˚C in a humidified incubator with 5% CO2 supply.

2.2.2 SRS imaging and quantification of CE in tissues and cell culture

SRS imaging was performed on a femtosecond SRS microscope, with the laser beating frequency tuned to the C-H stretching vibration band at 2845 cm^{-1}, as described previously [141]. No cell or tissue damage was observed during the imaging procedure. LD amount was quantified using ImageJ. Specifically, Threshold function was used to select LDs in the cells due to their significantly higher signal intensities compared to other cellular structures. "Analyze Particles" function was then used to quantify the area fractions of LDs in the whole image area, then normalized to the cell number counted from the same image. Each image contained ~10 cells and represented as n = 1.

Confocal Raman was performed as described previously [200]. CE percentage in LDs was linearly correlated with the height ratio of the 702 cm^{-1} peak (I_{702}) to the 1442 cm^{-1} peak (I_{1442}) and expressed as $I_{702}/I_{1442} = 0.00334 \times$ CE percentage (%). CE percentage for each group was obtained by averaging the CE percentage of LDs in 3 to 6 cells as Raman profiles of LDs in the same specimen were nearly the same.

2.2.3 Chemicals and reagents

Avasimin was prepared following the protocol described previously [110]. Avasimibe, DMSO, human albumin, cholesteryl oleate, glyceryl trioleate, myristoleic acid, palmitic acid, palmitoleic acid, stearate, oleate, linoleic acid, arachidonic acid, and docosahexaenoic acid were purchased from Sigma-Aldrich. IWP-2 was purchased from Abcam. Recombinant human Wnt3a was purchased from Bio-Techne Corporation. Luciferin was purchased from Perkin Elmer.

2.2.4 Migration assay

Migration assay was performed in Transwell chambers (Corning) with 8 μm pore-sized membranes. Cells were pre-treated with indicated treatment for 2 days before transferring to the Transwell chambers. 2×10^5 cells were seeded in the upper chamber in serum-free media. The lower chamber was filled with media containing 20% FBS and 50 ng/mL human EGF (Life Technologies). Cells were then incubated for 20 hr at 37˚C to migrate. The transwell membranes

were fixed and cells that had not migrated through the chamber were removed with a cotton swab. Migrated cells were stained with propidium iodide (Life Technologies) and visualized by confocal fluorescence microscopy. For quantification, average number of cells in 3 fields for one migration chamber was considered n = 1.

2.2.5 Prostate cancer orthotopic mouse model

Orthotopic model was used to study whether Avasimin treatment can suppress the development of metastasis in a mouse model. All animal procedures were approved by the Purdue Animal Care and Use Committee. PC-3M were injected into the prostate of male, 6-week-old NSG mice (Purdue University Center for Cancer Research) following the protocols reported previously [201, 202]. Specifically, 2×10^5 PC-3M cells were mixed with an equal volume of Matrigel HC (Corning) and injected into the prostate gland of the mouse. 10 days after the surgery, mice were randomly assigned into 2 groups for the treatment. Avasimin was dissolved in sterile PBS and administrated daily via intraperitoneal injections at the dose of 75 mg/kg. The dosage for the treatment was selected based on previous animal studies [110]. Sterile PBS was used for vehicle group. Primary tumor volume was assessed twice a week with palpation. Body weight was also measured twice a week. After treatment for 25 days, tumors and lung were harvested and prepared for tumor volume measurement, H&E and immunofluorescent chemistry (IFC) staining.

2.2.6 Prostate cancer intra-cardiac injection mouse model

Intra-cardiac injection model was used to study the therapeutic effect of Avasmin to metastasis already developed in mice by introducing tumor cells directly into the systemic circulation. All animal procedures were approved by the Purdue Animal Care and Use Committee. PC-3 cells with stable expression of luciferase (PC-3-Luc) were injected into the heart of male, 7-week-old nude mice (Envigo) following the protocols reported previously [201]. Specifically, 2×10^5 PC-3-Luc cells were injected into the left ventricle. 7 days after the injection, mice were randomly assigned into 2 groups for the treatment. Avasimin was dissolved in sterile PBS and administrated daily via intraperitoneal injections at the dose of 75 mg/kg. Sterile PBS was used for vehicle group. Tumor growth was monitored every two weeks by bioluminescent imaging using IVIS in Bindley Bioscience Center at Purdue. After treatment for 5 weeks, metastatic lesions in the heart, lungs, pancreas, liver, spleen, intestine, and kidneys were visualized using IVIS. Metastatic lesions were

harvested and prepared for H&E and spectroscopic imaging. Histological examination was performed by a pathologist after H&E staining to confirm metastatic lesions.

2.2.7 Histology and IFC staining

Primary prostate tumor and tissues containing metastatic lesions were fixed in 10% neutral buffered formalin. After paraffin embedding, tissue sections were stained using H&E staining. The adjacent tissue sections were used for IFC staining. After deparaffinization and rehydration of tissue slides, antigens were retrieved using unmasking solution (Vector Laboratories) with a 2100-Retriever (PickCell Laboratories). Tissue slides were then incubated with anti-human mitochondria antibody (Millipore MAB1273, 1:100) or anti-Ki-67 antibody (Leica KI67-MM1-L-CE, 1:200).

2.2.8 RT-PCR profiler array

Total RNA was extracted from PC-3 treated with DMSO or avasimibe using E.Z.N.A. Total RNA Kit I (Omega Bio-teck) and reverse transcribed using RT2 First Strand Kit (QIAGEN Inc) following the manufacturer's instructions. The human prostate cancer RT^2 Profiler PCR Array (PAHS-135Z) was purchased from QIAGEN Inc and quantitative PCR was conducted following the manufacturer's instructions using Roche LightCycler 96. Data analysis was performed based on the ΔΔCT method with normalization of the raw data to the housekeeping genes using PCR Array Data Analysis Web portal provided by the manufacturer. To determine fold change in gene expression, the normalized expression of each gene in the avasimibe-treated sample is divided by the normalized expression of the same gene in the control sample. Genes were grouped based on their functions.

2.2.9 Immunoblotting analysis

Cells were lysed in TBSN buffer (20 mM Tris, pH 8.0, 150 mM NaCl, 0.5% Nonidet P-40, 5 mM EGTA, 1.5 mM EDTA, 0.5 mM Na_3VO_4, 20 mM p-nitrophenyl phosphate) or RIPA buffer (Sigma-Aldrich) after indicated treatments. Proteins were detected by immunoblotting with the antibodies against active β-catenin (Millipore 05-665, 1:1000), β-catenin (Cell Signaling 9562S, 1:2000), Wnt3a (Abcam ab28472, 1:1000), and β-actin (Sigma A5441, 1:5000). The immunoblots were quantified using Image Lab software (Bio-Rad), using β-actin as a loading control.

2.2.10 Fatty acid extraction and measurement

PC-3 cells were starved to deplete the fatty acid pool, after which serum is supplemented with avasimibe (10 μM, 1 days). Free fatty acids were extracted from the cell pellets following the procedure reported previously [203]. Cell pellets were lysed in 200 μL methanol and acidified with 25 mM HCl. Then the sample was mixed with 1 mL iso-octane, and centrifuged at 3,000 g for 1 min. The top layer was transferred to new vials and the extraction was repeated once with the bottom layer. The combined iso-octane layers were dried under N_2 flow. For quantitative analysis, each fatty acid at known concentration were used as internal standards. Liquid Chromatography-Mass Spectrometry (LC-MS) analysis of fatty acids was performed following the protocol described previously [204].

2.2.11 Immunoprecipitation of Wnt3a from medium

For immunoprecipitation, 1 mL medium was collected from DU145 PTEN-KD cells and pre-incubated with 100 μL protein A/G agarose beads (Santa Cruz) on a rotator for overnight at 4˚C. The beads were discarded and the supernatant was incubated with anti-Wnt3a antibody (2 μg/mL) on a rotator for 10 – 12 hr at 4˚C and subsequently immunoprecipitated with protein A/G agarose beads while rotating for 2 hr at 4˚C. The beads were washed once with RPMI buffer supplemented with protease inhibitor. The proteins were then collected by resuspension in sample buffer and heated for 10 min at 50˚C. Supernatants were collected and supplemented with 100 mM dithiothreitol, and the mixture was heated for 5 min at 95˚C before SDS-PAGE.

2.2.12 Statistical Analysis

Results for the animal studies were shown as mean + standard error of the mean (SEM). Mann-Whitney U-test was used for comparisons between vehicle and Avasimin-treated groups as the data do not follow normal distribution. Other results were shown as mean + standard deviation (SD), unless stated otherwise, and Student's t-test was performed for the comparisons. $p < 0.05$ was considered statistically significant.

2.3 Results

2.3.1 CE accumulation in human metastatic PCa tissues

To map the lipid distribution and composition in metastatic PCa, human patient tissues from multiple metastatic sites, including abdominal soft tissue, liver, adrenal gland, rib and lymph nodes, were examined by SRS microscopy. C-H-rich lipids were visualized by tuning the laser beating frequency to be resonant with C-H stretching vibration. LDs were observed in metastatic lesions of abdominal soft tissue, liver, adrenal gland, rib and lymph nodes (**Figure 3.1A**). By analyzing the composition of these LDs with confocal Raman microspectroscopy [200], we found characteristic bands for cholesterol rings at 702 cm^{-1} and for ester bond at 1742 cm^{-1} in the Raman spectra of these LDs [205] (**Figure 3.1B**). These spectroscopic signatures indicate the presence of CE. For quantitative measurement of CE level in these samples, we constructed the calibration curve for molar percentage of CE in the total lipids based on the Raman spectral measurement of emulsions containing cholesteryl oleate and glyceryl trioleate. The height ratio between 702 cm^{-1} cholesterol band and 1442 cm^{-1} CH_2 bending band was linearly proportional to the molar percentage of CE in the lipid mixture (**Figure 3.1C**). Based on the calibration curve, we estimated that LDs in all metastatic lesions are composed of 60 to 80% CE (**Figure 3.1D**). Our analysis suggests that accumulation of CE is a metabolic marker for metastatic PCa.

2.3.2 CE depletion suppresses PCa migration *in vitro* and metastasis *in vivo*

CE accumulation in metastatic tumor suggests a possible functional role of CE in metastasis. We hypothesized that depleting CE by ACAT inhibitor would reduce metastatic potential of PCa. To test this hypothesis, we first examined the migration capability of PC-3M, a metastatic PCa cell line derived from liver metastasis of PC-3 xenograft [206]. We treated cultured PC-3M with a potent ACAT inhibitor, avasimibe. To confirm the reduction of CE level after avasimibe treatment, we measured Raman spectra of LDs in PC-3M cells using confocal Raman microscopy. The Raman spectral analysis showed a significant reduction in CE level upon avasimibe treatment (**Figure 3.2**). To assess migration capability, we performed a transwell assay of PC-3M cells pre-treated with avasimibe. Our results indicate that migration capability of PC-3M cells was suppressed significantly (**Figure 3.3**). These results suggest that CE depletion impairs the migration capability of PCa cells.

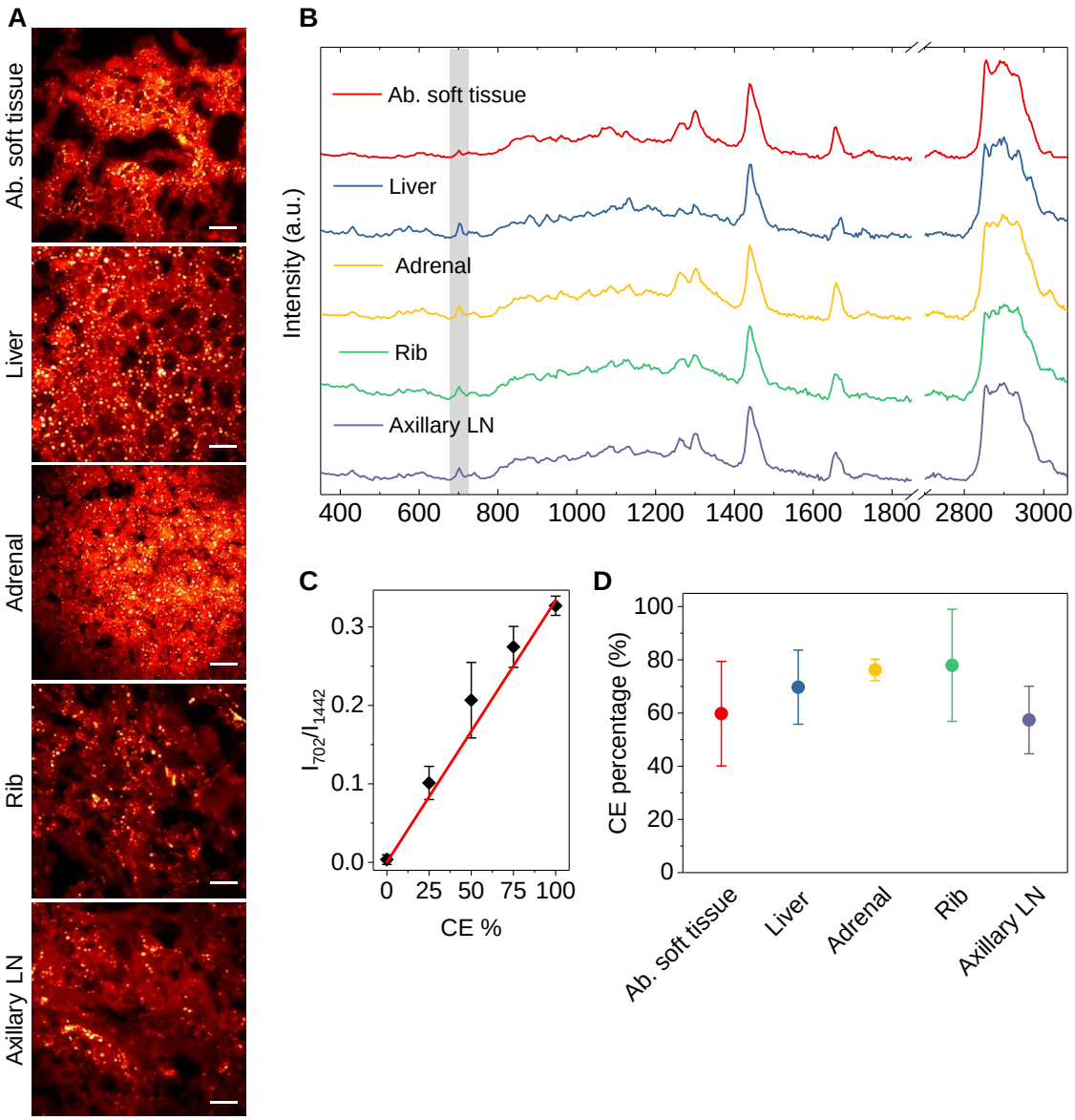

Figure 2.1 CE accumulation in human metastatic PCa.
(A) SRS images of metastatic PCa in abdominal soft tissue (ab. soft tissue), liver, adrenal gland, rib and axillary lymph node (LN). Scale bar: 20 μm. (B) Raman spectra of LDs in metastatic PCa tissues shown in (A). Spectral intensity was normalized by CH_2 bending at 1442 cm^{-1}. Grey shade indicates the band of cholesterol rings at 702 cm^{-1}. (C) Calibration curve of molar percentage of CE in total lipid, generated by linear fitting of height ratio between the peak at 702 cm^{-1} (I_{702}) and the peak at 1442 cm^{-1} (I_{1442}). I_{702}/I_{1442} = 0.00334 × CE %. R^2 = 0.99. Error bars represent SD (n = 3). (D) CE molar percentage in LDs of metastatic PCa in abdominal soft tissue (n = 3), liver (n = 6), adrenal gland (n = 3), rib (n = 3), and axillary lymph node (n = 6). Error bars represent SD.

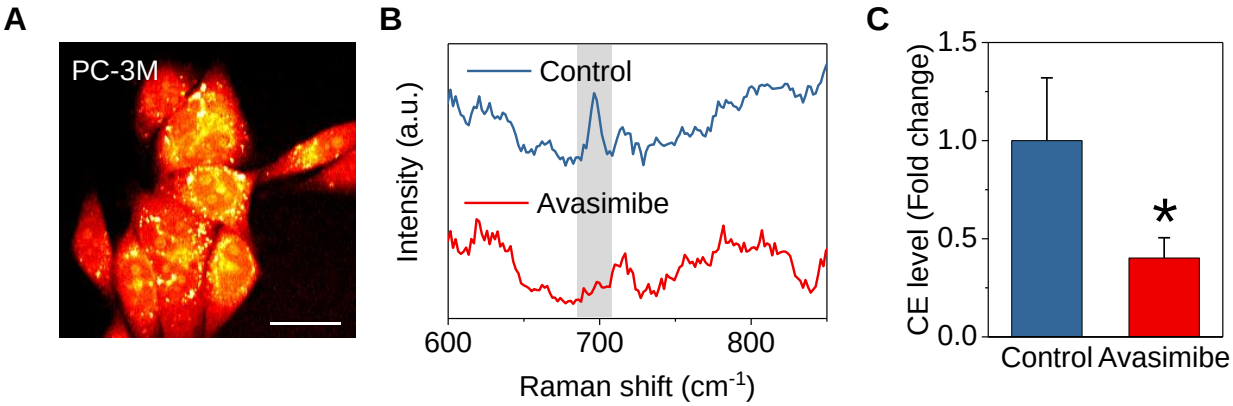

Figure 2.2 CE depletion by avasimibe treatment in PCa cells.
(A) An SRS image of PC-3M cells with LDs. Scale bar: 10 μm. (B) Raman spectra of LDs in PC-3M treated with avasimibe (10 μM, 1 day). Grey shade indicates the bands of cholesterol rings at 702 cm^{-1}. (C) Change in CE molar percentage in LDs of PC-3M cells after avasimibe treatment.
Error bars represent SD (n = 7). *p < 0.05.

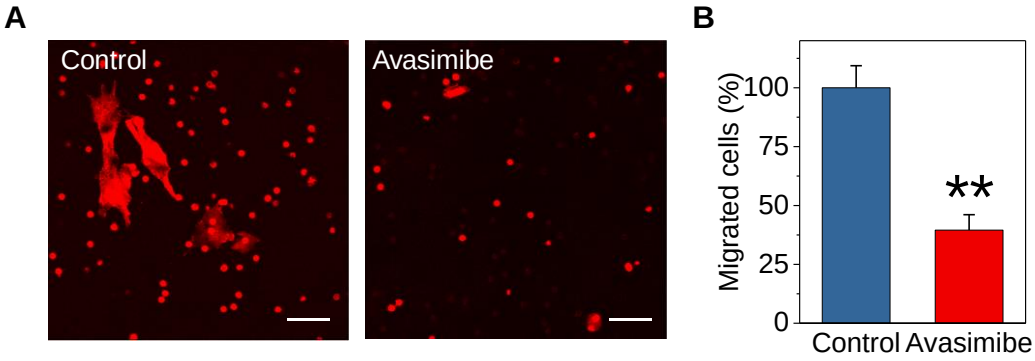

Figure 2.3 PCa migration suppressed by ACAT inhibition.
(A) Representative images of migration of PC-3M cells pre-treated with avasimibe (10 μM, 2 days). Red: propidium iodide staining. Scale bar: 50 μm. (E) Quantitation of migrated cells shown in (A). Error bars represent SD (n = 2). **p < 0.005.

To examine whether CE depletion can suppress PCa tumor metastasis, we generated an orthotopic mouse model of prostate cancer using the PC-3M cells [201, 202]. The mice bearing an orthotopic PC-3M xenograft were treated with either vehicle or Avasimin, a systemically injectable nanoformulation of avasimibe [110]. As illustrated in **Figure 3.4A**, mice were treated with Avasimin daily via intraperitoneal injection and tumor metastasis was assessed at the end of the study by IFC staining of cancer cells in lung tissue sections. Primary prostate tumor growth was monitored over the treatment period. Avasimin treatment reduced the growth rate of primary tumors significantly (**Figure 3.5A**) and inhibited the tumor size by ~1.4-fold at the end of 25-day treatment (**Figure 3.4B**). No changes in body weight were observed in mice treated with Avasimin, indicating no detectable general toxicity to the animals (**Figure 3.4C**). To characterize primary prostate cancers after the treatment, we performed IFC staining of prostate tissues harvested at the end of the study. Anti-human mitochondria antibody was used to specifically label human cancerous cells presented in mouse tissues (**Figure 3.5B**). Primary prostate tumors were visualized in tissues from both vehicle and Avasimin-treated mice. Importantly, we observed that cancer cells in the vehicle-treated group have invaded into the normal tissues, whereas cancer cells in the Avasimin-treated group maintained a confined tumor margin (**Figure 3.4D**). This phenotype was confirmed by pathological review of the adjacent sections. Furthermore, Ki-67 staining of the adjacent tissue sections showed lower expression of Ki-67 in Avasimin-treated group compared to control group, which indicates an anti-proliferating effect of Avasimin to the primary tumor (**Figure 3.4D**). Taken together, these results provide evidence that Avasimin treatment suppresses invasive phenotype and proliferation of primary PCa.

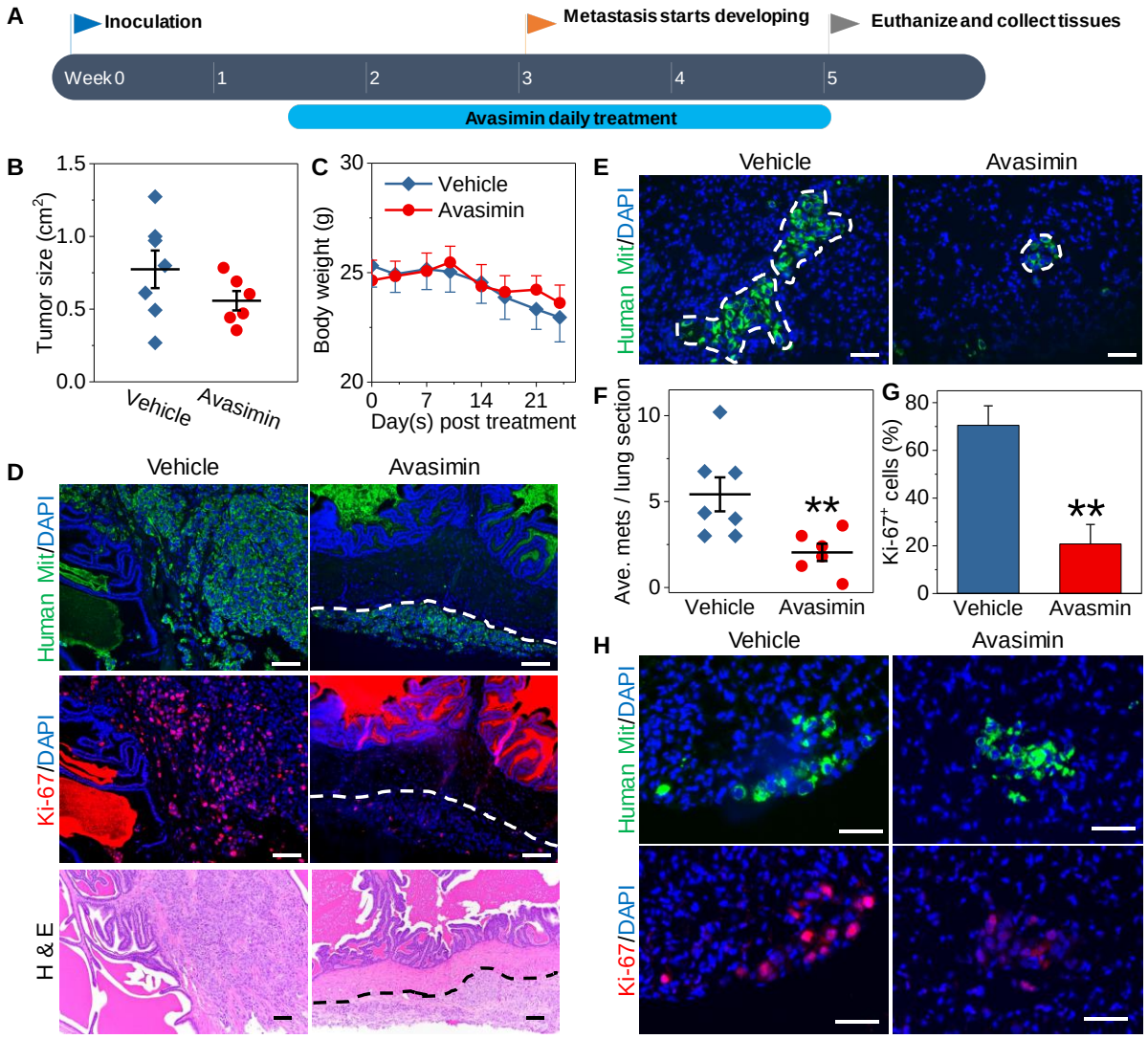

Figure 2.4 PCa metastasis suppressed by targeting cholesterol esterification *in vivo*. (A) Schematic of PCa orthotopic model study. Avasimin (75 mg/kg) was administrated into mice daily via intraperitoneal injection from 10 days post-transplantation of PC-3M. Vehicle mice were treated with sterile PBS. (B) Tumor size measured after harvested from vehicle (n = 7) and avasimin-treated (n = 6) mice. (C) Body weight of the mice over 25-day treatments. (D) Representative images of IFC and H&E staining of primary prostate tumor tissues harvested at the end of the study. Dashed lines indicate clear tumor margins in the vehicle group. Scale bar: 100 μm. (E) Representative images of IFC staining of lung tissues harvested at the end of the study with distinct metastatic clusters indicated. Scale bar: 50 μm. (F) Quantification of metastatic clusters in lung tissues harvested from vehicle and Avasimin-treated mice. (G-H) Percentage of Ki-67-positive cells in metastatic tumor lesions harvested from lung tissues of vehicle and Avasimin-treated mice. Representative images shown in (H). Green: human mitochondria, red: Ki-67, blue: DAPI. Error bars represent SEM. **p < 0.005.

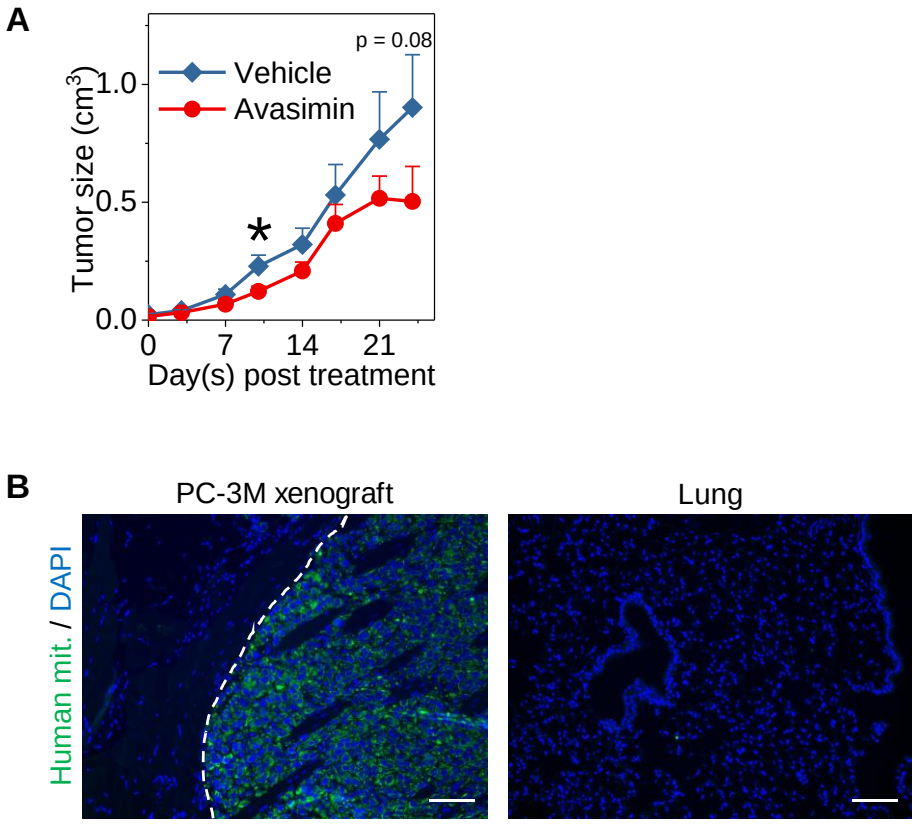

Figure 2.5 Primary PCa growth suppressed by targeting cholesterol esterification *in vivo*. (A) Primary prostate tumor growth curve estimated by palpation. Error bars represent SEM (n = 7 for vehicle, n = 6 for Avasimin). *p < 0.05. (B) Representative images of IFC staining of PC-3M xenograft on muscle and lung from a healthy NSG mouse. Dashed line indicates clear tumor margin. Scale bar: 100 µm.

To assess metastasis in this mouse model, we performed IFC staining of lung tissues with anti-human mitochondria antibody and counted the number of metastatic clusters. Distinct metastasis was defined by a clear cluster of 5 or more cells [202] (**Figure 3.4E**, dashed lines), and counted from the whole lung sections for each mouse. We found a dramatic reduction (~50%) in the number of metastatic clusters in the lung of Avasimin-treated mice compared to that in vehicle-treated mice (**Figure 3.4F**), indicating reduced metastatic potential of PCa by Avasimin. Moreover, Ki-67 staining of the adjacent tissue sections showed ~3.5-fold reduction in the level of Ki-67 in metastatic lesions of Avasimin-treated group, indicating anti-proliferative activity of Avasimin to the metastatic tumors (**Figure 3.4G** and **H**). These results collectively support that CE depletion by Avasimin suppresses metastatic potential of PCa *in vivo*.

2.3.3 CE depletion directly inhibits growth of metastatic PCa *in vivo*

To determine the clinical potential of CE depletion as a cancer therapy for metastatic PCa, we examined therapeutic efficacy of Avasimin in an intra-cardiac injection model [201], where metastatic PCa cells have already spread to other organs at the start of treatment. Seven days after transplantation of PC-3 cells stably expressing luciferase (PC-3-Luc), the mice were treated with Avasimin daily via intraperitoneal injection and tumor growth was monitored bi-weekly using *in vivo* bioluminescence imaging (**Figure 3.6A**). A significant reduction of tumor growth rate in Avasimin-treated group compared to vehicle-treated group was determined (**Figure 3.6B** and **C**). Body weight measurement showed no significant change during the treatment period, indicating no observable toxicity to the mice (**Figure 3.6D**). After 35 days of Avasimin treatment, we observed ~4.7-fold reduction in metastatic tumor size in lungs, liver, and spleen/pancreas (**Figure 3.6E** and **F**). To evaluate the amount and composition of LDs in the metastatic cancer, we conducted spectroscopic analysis on the frozen lung tissue sections. By SRS imaging of the cancerous lesions, we observed a significant reduction of LDs in Avasimin-treated group compared to the control group (**Figure 3.6G**). Confocal Raman spectroscopy further demonstrated that CE level is significantly reduced in these LDs in Avasimin-treated group (**Figure 3.6H**), confirming CE depletion after the treatment. Collectively, these results support our hypothesis that depleting CE suppresses metastatic tumor growth.

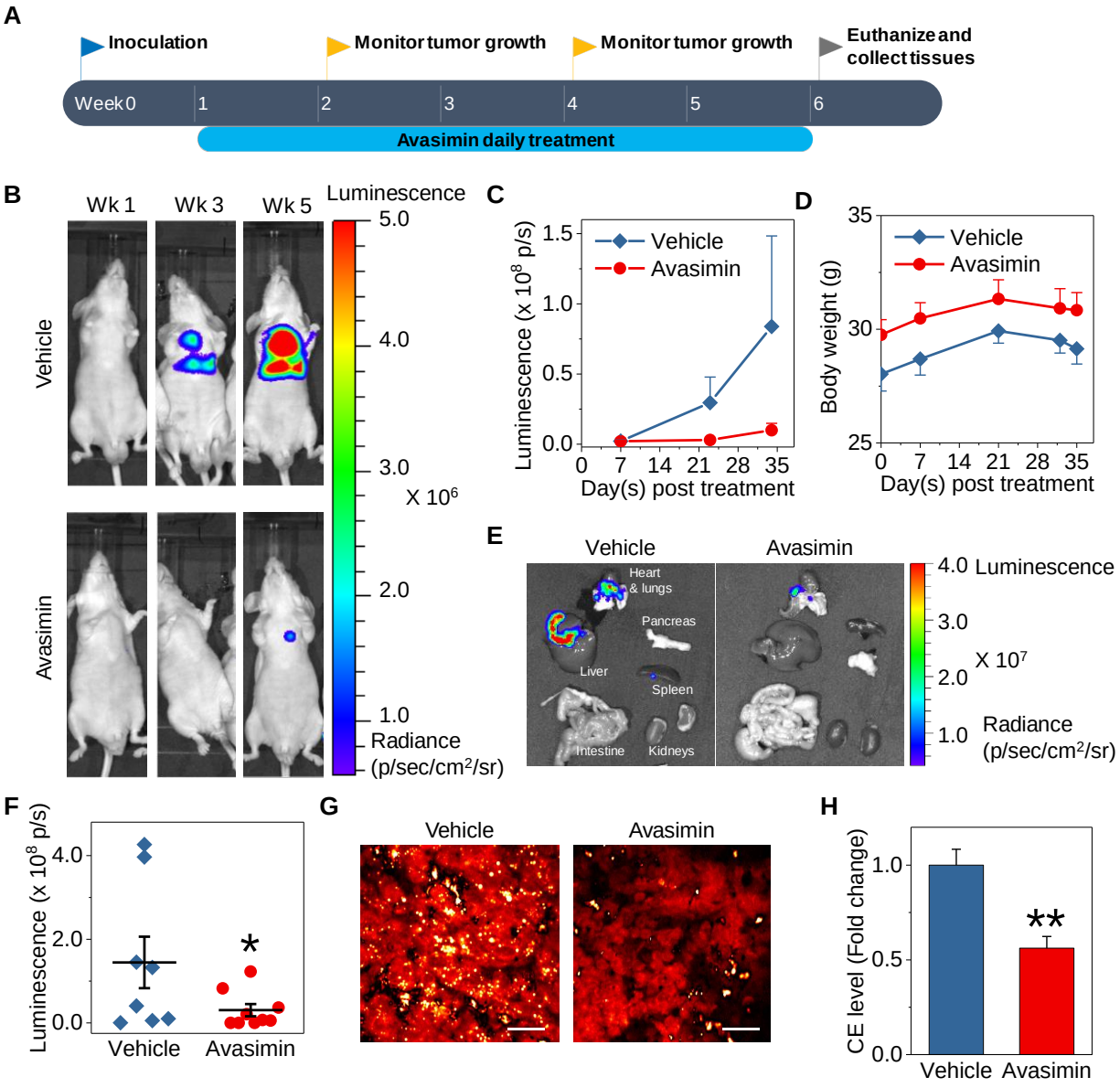

Figure 2.6 Metastatic PCa growth inhibited by CE depletion *in vivo*.
(A) Schematic of PCa intra-cardiac injection model study. Avasimin (75 mg/kg) was administrated into mice daily via intraperitoneal injection from 7 days post-inoculation of PC-3-Luc. Vehicle mice were treated with sterile PBS. (B) Representative IVIS images of mice treated with vehicle (n = 8) and Avasimin (n = 9). (C) Tumor growth curve quantified by total intensity of IVIS imaging. (D) Body weight of the mice over 35-day treatments. (E) Representative IVIS images of metastatic lesions in organs. (F) Quantification of total intensity of metastatic lesions from IVIS imaging. (G) SRS images of metastatic lesions in lung tissues harvested at the end of the study. Scale bar: 10 μm. (H) CE level in the metastatic lesions shown in (G). Error bars represent SEM (n > 3). *p < 0.05, **p < 0.005.

2.3.4 Gene expression profiling reveals inactivation of Wnt/β-catenin pathway by CE depletion

To unveil the signaling pathways that are associated with CE accumulation and/or depletion, we measured the expression levels of 84 human PCa-related genes after inhibiting cholesterol esterification in PC-3 cells, a metastatic PCa cell line [207]. After confirming CE depletion with avasimibe using confocal Raman microscopy (**Figure 3.7A** and **B**), the gene expression analysis was performed using a RT-PCR profiler array. The analysis revealed increased expression of regulators that negatively impact metastasis (DKK3 [208], DLC1 [209], FOXO1 [210], GNRH1) and genes that are lost in metastatic PCa (EGR3 [211], GPX3 [212], NKX3-1 [213]) (**Figure 3.7C** and **Figure 3.8A**). At the same time, expression level of proliferating marker gene MKI67 was decreased dramatically, supporting suppressed cancer proliferation by avasimibe (**Figure 3.7C** and **Figure 3.8B).** We also note that CE depletion by avasimibe inhibited expression of ERG by ~2.8-fold, which is a common proto-oncogene in PCa (**Figure 3.7C** and **Figure 3.8B**). Overall, these results indicate that CE depletion by avasimibe suppresses proliferation and metastatic potential of PCa through upregulating multiple negative regulators of metastasis.

Among these metastasis-related genes, DKK3 is a negative regulator of Wnt/β-catenin pathway, one of the major oncogenic pathways associated with PCa progression and metastasis [214, 215]. To confirm that CE depletion inactivates Wnt/β-catenin, immunoblotting of β-catenin was performed in PC-3 cells after ACAT inhibition by avasimibe. Protein level of active β-catenin significantly decreased after avasimibe treatment (**Figure 3.7D**). To eliminate the possibility of nonspecific targeting by ACAT inhibitor, we knocked down ACAT-1 using shRNA (**Figure 3.9A**). ACAT-1 knockdown in PC-3 depleted CE (**Figure 3.9B** and **C**) and resulted in significant reduction of active β-catenin protein level (**Figure 3.7D**). Since active β-catenin translocate to nucleus to act as a transcription factor, we analyzed localization of β-catenin by immunofluorescence staining. CE depletion by either avasimibe or ACAT-1 knockdown reduced nuclear localized β-catenin in PC-3 (**Figure 3.7E** and **F**, **Figure 3.9D** and **E**). To test whether β-catenin inactivation by ACAT inhibition occurs to other aggressive PCa cell lines, we used two other CE-rich aggressive PCa cell models developed from LNCaP and DU145. LNCaP-HP (high passage) is a cell line derived upon continuous passage from LNCaP-LP (low passage) until the passage number exceeds 81 [196], which shows more aggressive and invasive phenotypes

compared to LNCaP-LP [196-199]. DU145 with stable PTEN knockdown (DU145 PTEN-KD) is an invasive cell line [216] containing significantly higher CE compared to PTEN wildtype DU145 [88]. In both cell models, CE depletion by avasimibe significantly downregulated β-catenin (**Figure 3.10**), which also supports inactivation of Wnt/β-catenin signaling by ACAT inhibition. These results collectively indicate that CE depletion inactivates Wnt/β-catenin pathway in aggressive PCa cells.

Figure 2.7 Depleting CE downregulates Wnt/β-catenin pathway.
(A) SRS images of PC-3 cells treated with avasimibe (5 μM, 3 days). Scale bar: 10 μm. (B) CE percentage in PC-3 cells shown in (A). Error bars represent SD (n = 10). (C) Expression profiling of 84 PCa-related genes in PC-3 cells shown in (A). Upregulation is indicated by shades of red, and downregulation is indicated by shades of green. Grey indicate genes that are not expressed. ±1.5-fold change is set as a threshold. ECM: extracellular matrix, GF: growth factor. (D) Immunoblot of antibodies against active β-catenin (de-phosphorylated at Ser37 and Thr41) and β-actin in PC-3 cells treated with concentrations of avasimibe as indicated for 2 days or with ACAT-1 shRNA. (E) Immunofluorescent staining of β-catenin in PC-3 cells treated with concentrations of avasimibe as indicated for 2 days. Scale bar: 10 μm. (F) Quantification of cells with nuclear β-catenin after avasimibe treatment. Error bars represent SD (n > 90 in each group). **p < 0.005, ***p < 0.0005.

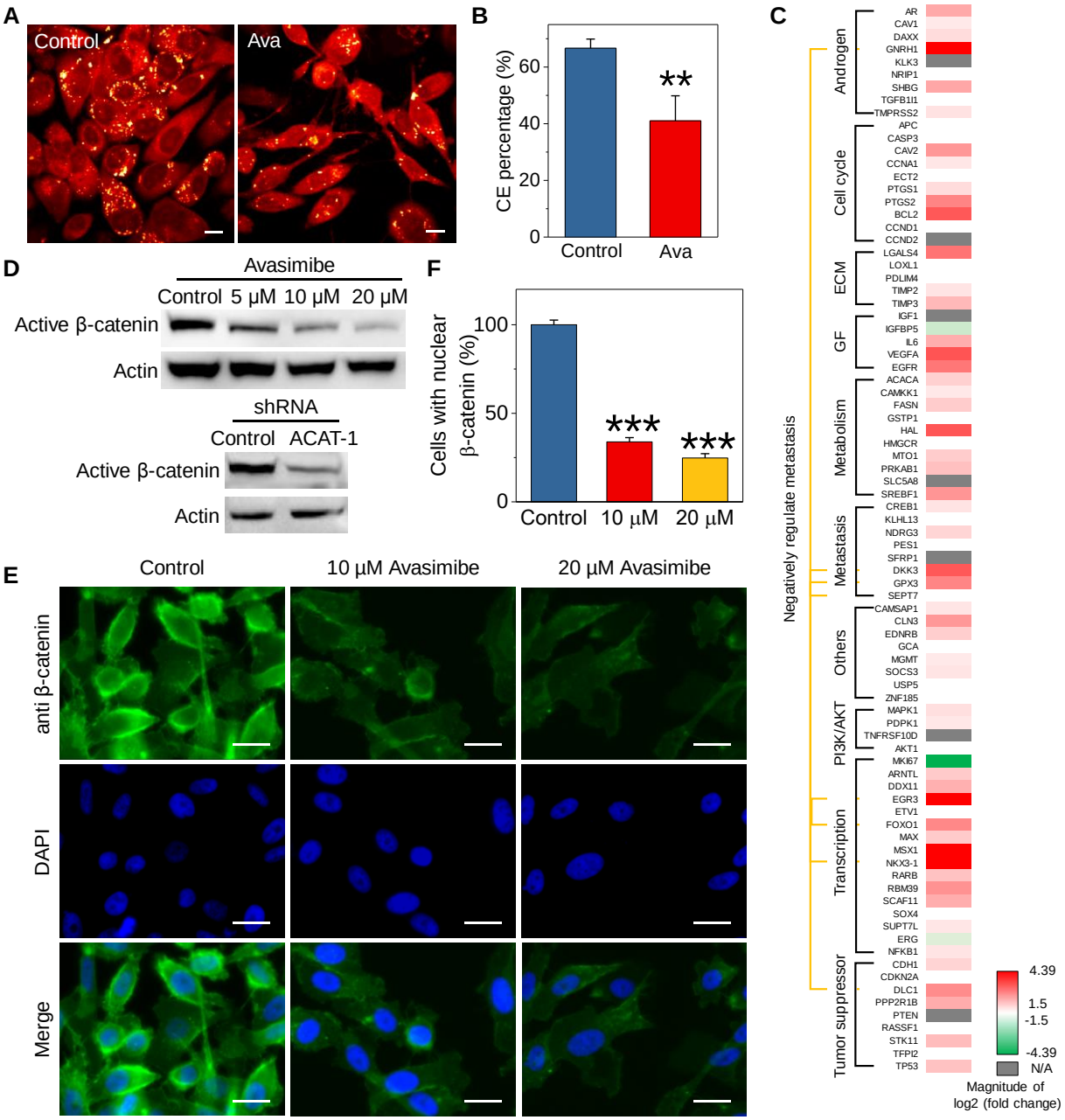
A
Control
Ava
B
CE percentage (%)
60
40
20
0
**
Control
Ava
C
Negatively regulate metastasis
Androgen
AR
CAV1
DAXX
GNRH1
KLK3
NRIP1
SHBG
TGFB1I1
TMPRSS2
Cell cycle
APC
CASP3
CAV2
CCNA1
ECT2
PTGS1
PTGS2
BCL2
CCND1
CCND2
ECM
LGALS4
LOXL1
PDLIM4
TIMP2
TIMP3
GF
IGF1
IGFBP5
IL6
VEGFA
EGFR
Metabolism
ACACA
CAMKK1
FASN
GSTP1
HAL
HMGCR
MTO1
PRKAB1
SLC5A8
SREBF1
Metastasis
CREB1
KLHL13
NDRG3
PES1
SFRP1
DKK3
GPX3
SEPT7
Others
CAMSAP1
CLN3
EDNRB
GCA
MGMT
SOCS3
USP5
ZNF185
PI3K/AKT
MAPK1
PDPK1
TNFRSF10D
AKT1
Transcription
MKI67
ARNTL
DDX11
EGR3
ETV1
FOXO1
MAX
MSX1
NKX3-1
RARB
RBM39
SCAF11
SOX4
SUPT7L
ERG
NFKB1
Tumor suppressor
CDH1
CDKN2A
DLC1
PPP2R1B
PTEN
RASSF1
STK11
TFPI2
TP53
4.39
1.5
-1.5
-4.39
N/A
Magnitude of
log2 (fold change)
D
Avasimibe
Control 5 μM 10 μM 20 μM
Active β-catenin
Actin
shRNA
Control ACAT-1
Active β-catenin
Actin
F
Cells with nuclear β-catenin (%)
100
50
0
***
***
Control 10 μM 20 μM
E
Control
10 μM Avasimibe
20 μM Avasimibe
anti β-catenin
DAPI
Merge

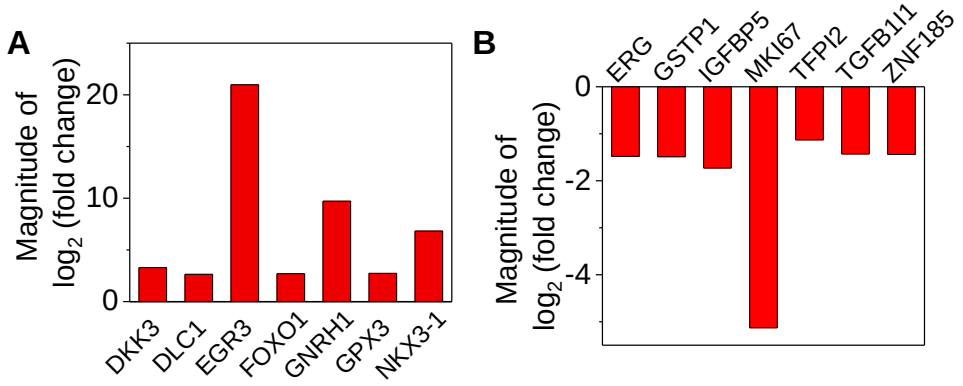

Figure 2.8 Expression profiling of PCa-related genes after ACAT inhibition.
(A) Changes in expression of 7 genes that negatively impact PCa metastasis after ACAT inhibition in PC-3 cells. (B) Downregulated genes after ACAT inhibition in PC-3 cells.

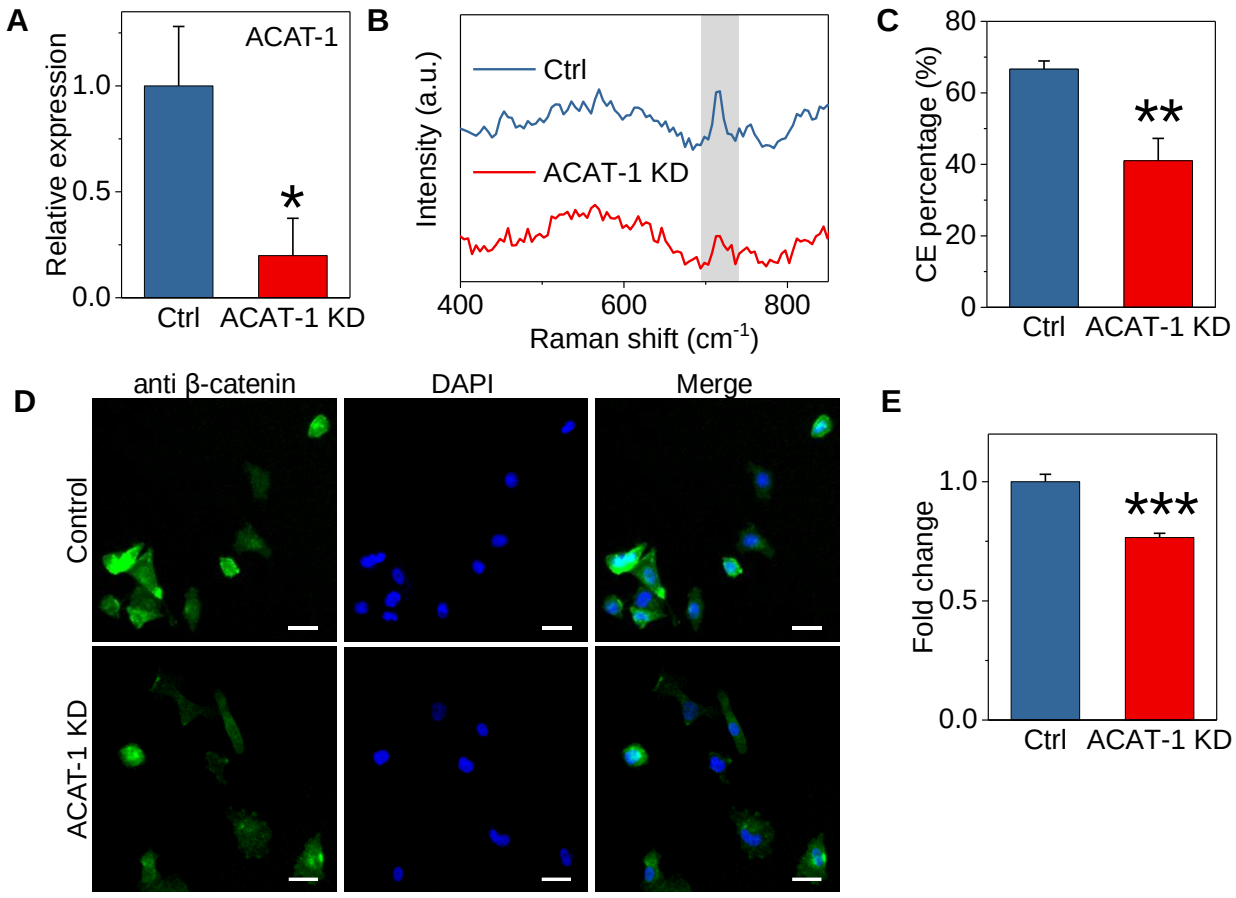

Figure 2.9 Inactivation of Wnt/β-catenin pathway by ACAT-1 knockdown.
(A) ACAT-1 expression level in PC-3 cells treated with ACAT-1 shRNA. Error bars represent SD (n = 2). (B) Raman spectra of LDs in ACAT-1 knocked down PC-3. Grey shade indicates the bands of cholesterol rings at 702 cm^{-1}. (C) Change in CE molar percentage in LDs of ACAT-1 knocked down PC-3. Error bars represent SD (n = 8). (D) Immunofluorescent staining of β-catenin in ACAT-1 knocked down PC-3 cells. Scale bar: 10 μm. (E) Quantification of cells with nuclear β-catenin after ACAT-1 knockdown. Error bars represent SD (n > 90 in each group). *p < 0.05, **p < 0.005, ***p < 0.0005.

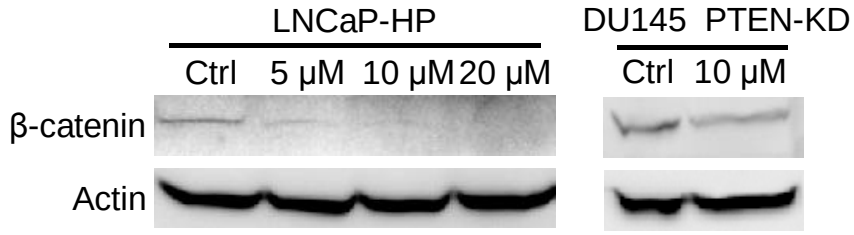

Figure 2.10 Inactivation of Wnt/β-catenin pathway by CE depletion.

Immunoblot of antibodies against β-catenin and β-actin in LNCaP-HP and DU145-PTEN knockdown (DU145 PTEN-KD) treated with concentrations of avasimibe as indicated for 2 days.

2.3.5 CE depletion suppresses lipogenic potential of PCa

In Wnt/β-catenin signaling pathway, lipid modification of Wnt is a prerequisite for Wnt activation [217, 218]. During the acylation process, fatty acids serve as substrates for this reaction. Interestingly, we observed decreased amount of LD in Avasimin-treated metastatic PCa tissues (**Figure 3.6G**) and avasimibe-treated PCa cells (**Figure 3.7A**), suggesting the possibility of reduced lipogenic potential. Considering the crosstalk between regulation of cholesterol and fatty acid metabolisms [219, 220], we hypothesized that CE depletion limits availability of fatty acid substrates for Wnt acylation. To test our hypothesis, we performed SRS imaging on LDs in PCa cell lines after ACAT inhibition (**Figure 3.11A**). From analysis of LD amount in SRS images, we found ~1.7-fold reduction in the number of LDs in cells treated with avasimibe or with ACAT-1 shRNA (**Figure 3.11B**). To confirm that such reduction is a result of decreased lipogenesis or uptake, the levels of free fatty acids in PCa were analyzed using LC-MS. Overall, fatty acid synthesis or uptake in CE-depleted cells was reduced for most of fatty acid species tested, except for docosahexaenoic acid (C22:6) (**Figure 3.11C-E**). The most significant reduction was found in monounsaturated fatty acids (C14:1, C16:1, C18:1) (**Figure 3.11D**). These results support our hypothesis that CE depletion reduces free fatty acid availability in PCa.

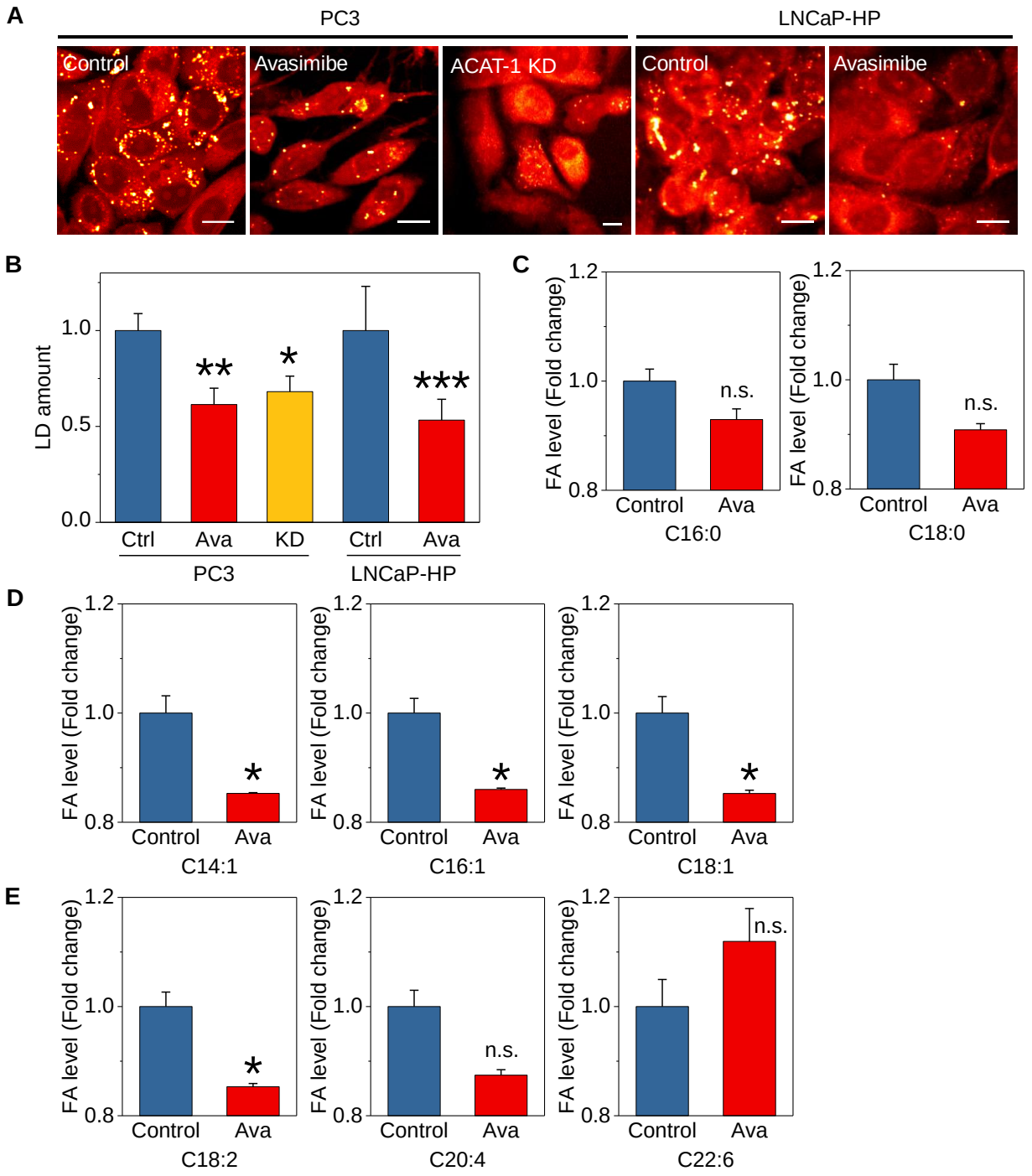

Figure 2.11 ACAT inhibition reduces fatty acid levels in PCa.
(A) SRS images of PC-3 and LNCaP-HP cells treated with avasimibe (10 μM, 2 days) or with ACAT-1 shRNA. Scale bar: 10 μm. (B) Quantitation of LD amount normalized to control groups. Error bars represent SD (n > 9). (C-E) LC-MS measurement of fatty acids from lipids extracted from PC-3. Fatty acid levels were normalized by cell number in each group. Fatty acids are grouped in saturated fatty acids (C), monounsaturated fatty acids (D), and polyunsaturated fatty acids (E). Error bars represent SEM (n = 3). *p < 0.05, **p < 0.005, n.s.: not significant.

2.3.6 CE depletion suppresses cell migration through inhibiting Wnt3a secretion

Stabilization and nuclear transport of β-catenin is a result of Wnt activation, which requires secretion and binding of lipid-modified Wnt to membrane proteins [217, 218]. As fatty acid levels in cells decrease, substrates for Wnt acylation become limited. We note that one decreased monounsaturated fatty acid after ACAT inhibition, palmitoleic acid (C16:1), is the fatty acid species used for Wnt acylation required for secretion [218]. Therefore, it is likely that Wnt secretion is inhibited as a consequence of CE depletion. First, we tested whether Wnt is inactivated after CE depletion by visualizing its location. By immunofluorescent staining of Wnt3a in PCa cells after avasimibe treatment, we observed membrane localized Wnt3a in control cells (**Figure 3.12A**), indicating activation of Wnt3a. In contrast, avasimibe-treated cells show dramatic ~6-fold reduction in membrane-bound Wnt3a, accompanied by intracellular aggregates of Wnt3a (**Figure 3.12A** and **B**). The Wnt3a distribution after avasimibe treatment resembles the localization of Wnt3a after IWP-2 treatment, a potent inhibitor of Wnt3a acylation [221] (**Figure 3.12A**). To further confirm inactivation of Wnt3a, we measured intracellular and secreted Wnt3a after avasimibe treatment using immunoblotting analysis. Intracellular Wnt3a level increased after avasimibe treatment, while medium Wnt3a level decreased by ~1.4-fold (**Figure 3.12C**). These results indicate that avasimibe treatment inactivates Wnt/β-catenin pathway through reducing Wnt secretion.

To test whether Wnt/β-catenin is an essential pathway that links CE accumulation to aggressiveness of PCa, we performed a migration rescue experiment with Wnt3a. CE depletion by avasimibe significantly suppressed migration capability of PCa by ~42% (**Figure 3.12D** and **E**). When Wnt3a was supplemented into the medium, migration capability of the cells was rescued significantly (**Figure 3.12D** and **E**), although not to the full extent (~86% recovery). These results indicate that CE depletion suppresses PCa aggressiveness largely through Wnt/β-catenin pathway.

Based on our data, we propose that blocking cholesterol esterification creates imbalance in cancer lipid metabolism that is important for modulating the activities of Wnt/β-catenin pathway (**Figure 3.12F**). Under normal condition, excess cholesterol in PCa cells is esterified and stored in LDs by ACAT, and high level of lipid synthesis and/or uptake [222-224] provides sustained, ample supply of fatty acids (i.e. palmitic acid and palmitoleic acid) for acylation of Wnt protein. Lipid-modified

Wnt is secreted and bound to membrane to exert its functions, such as promoting cell migration and invasion. By inhibition of cholesterol esterification, expression and cleavage of SREBP-1 decreased as we reported previously [88]. Consequently, the unavailability of fatty acids inhibited the Wnt acylation and secretion. Unable to bind to the membrane, the inactivation of Wnt/β-catenin signaling suppressed PCa migration and metastasis.

2.4 Discussion

Metastatic PCa is a deadly disease still in need of effective treatment [225]. Androgen deprivation therapy (ADT) is the first-line hormone treatment for metastatic PCa [226]. Despite initial tumor regression, progression into castration-resistant PCa is inevitable [195]. Although drugs that target androgen receptor or androgen synthesis (i.e. enzalutamide or abiraterone) show clinical benefits [227], resistance to these treatments eventually occur [228]. These phenomena show that current therapeutic strategies for metastatic PCa are still not curative [195] and development of new treatments is needed to improve patient outcomes.

In this study, we revealed an essential role of CE in metastasis and its potential as a therapeutic target for metastatic PCa. Using two animal models that focus on different aspects of metastatic PCa, we tested the therapeutic benefits of CE depletion on development of metastasis and growth of metastatic tumors in mice. PCa metastasis in an orthotopic mouse model involves escape of cancer cells from the primary tumor site and migration into other organs. It also provides information about the therapeutic effect on the primary tumor. Using this mouse model, we observed striking phenotypic differences between the primary tumors in vehicle versus that in Avasimin-treated mice, which provides strong evidence that ACAT inhibition suppresses invasiveness of PCa cells. Consistently, we observed a reduced number of metastatic nodules in Avasimin-treated mice, supporting that ACAT inhibition suppresses development of metastasis during PCa progression.

Figure 2.12 CE depletion inhibits cell migration through reducing Wnt3a secretion.
(A) Immunofluorescent staining of Wnt3a in DU145 PTEN-KD treated with avasimibe (10 μM, 2 days) or IWP-2 (10 μM, 1 day). Arrows indicate membrane localized Wnt3a. Green: Wnt3a, Blue: DAPI. Scale bar: 25 μm. Insert scale bar: 10 μm. (B) Quantification of cells with membrane Wnt3a after avasimibe or IWP-2 treatment as indicated in (A). (C) Immunoblot of antibodies against Wnt3a and β-actin in DU145 PTEN-KD treated with avasimibe (10 μM, 2 days). Medium Wnt3a was immunoprecipitated and normalized by precipitated protein concentration. (D) Representative images of migration of cells pre-treated with avasimibe (10 μM, 2 days) and subsequent Wnt3a supplement (100 ng/mL). Red: propidium iodide staining. Scale bar: 50 μm. (E) Quantitation of migrated cells shown in (D). Error bars represent SD (n = 3). ***$p < 0.0005$. (F) Schematic showing the molecular mechanism. In metastatic PCa, high level of lipid synthesis and/or uptake provides fatty acid substrates for Wnt acylation. This process is accompanied by conversion of excess cholesterol to CE by ACAT and stored in LDs. Wnt acylation allows secretion and binding of Wnt to the membrane to drive cell migration and invasion. Suppressing cholesterol esterification by ACAT inhibition downregulates SREBP through negative feedback loop. As a result, lipogenesis pathway is suppressed, which limits the availability of free fatty acids required for Wnt acylation. Metastasis is then inhibited by reduced secretion of Wnt protein.
SFA: saturated fatty acid, MUFA: unsaturated fatty acid, LD: lipid droplet.

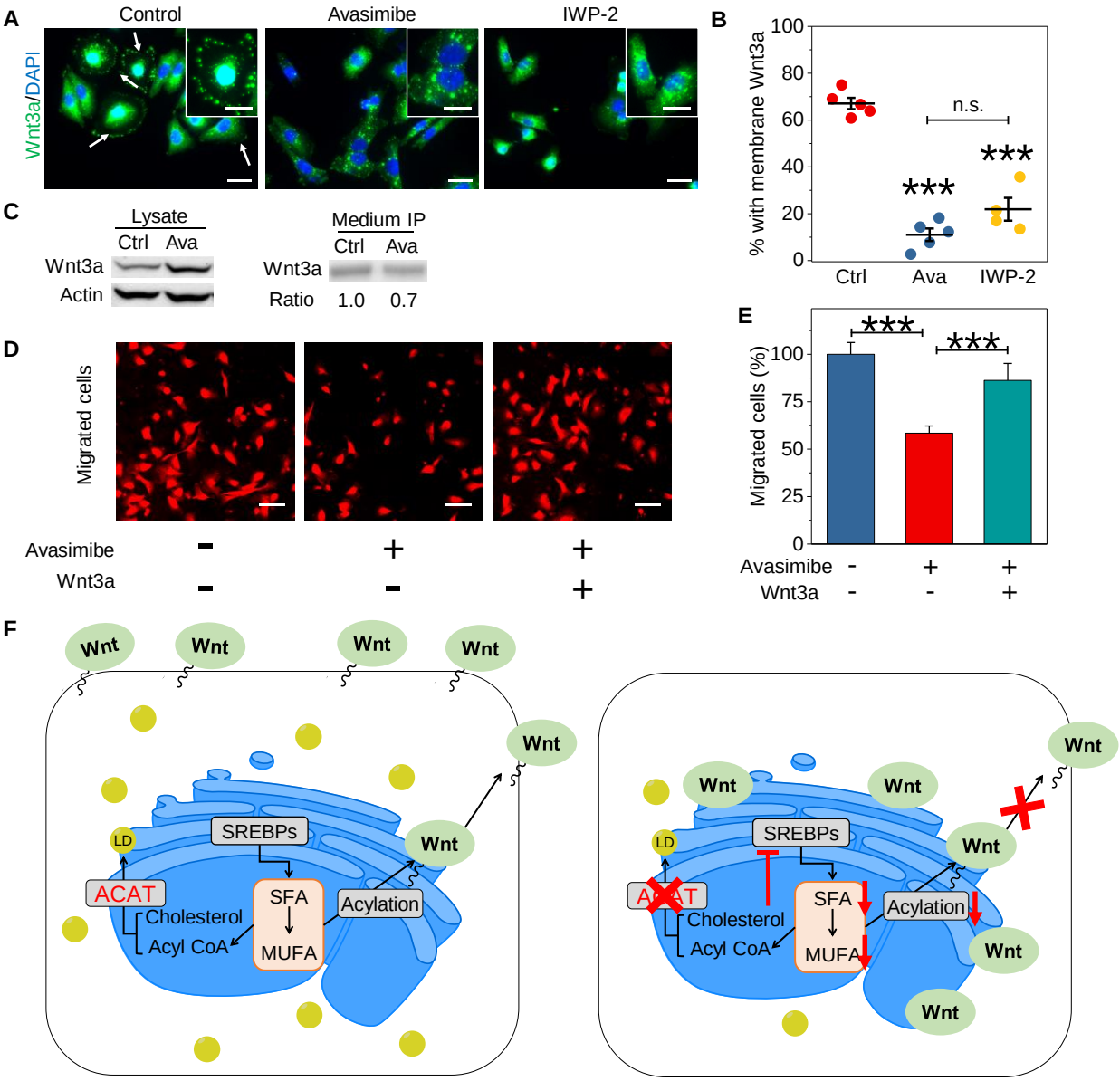
A
Control
Avasimibe
IWP-2
Wnt3a/DAPI
B
% with membrane Wnt3a
n.s.
***
***
Ctrl
Ava
IWP-2
C
Lysate
Ctrl Ava
Wnt3a
Actin
Medium IP
Ctrl Ava
Wnt3a
Ratio 1.0 0.7
D
Migrated cells
Avasimibe - + +
Wnt3a - - +
E
Migrated cells (%)
***
***
Avasimibe - + +
Wnt3a - - +
F
Wnt
SREBPs
LD
ACAT
Cholesterol
Acyl CoA
SFA
MUFA
Acylation

The intra-cardiac injection mouse model introduces the tumor cells directly into circulation, thus emphasizes the survival and growth of PCa cells in other organs. Thus, we used this model to evaluate therapeutic efficacy of CE depletion in mice with metastatic PCa already developed. Our results indicate that Avasimin treatment effectively suppressed growth of metastatic PCa in multiple organs. Importantly, we did not observe detectable toxicity from Avasimin to the animals. This is because CE content is usually low in most normal cell types [9, 63], giving a unique opportunity to specifically target PCa cells without causing unfavorable disturbance to the cholesterol homeostasis in most of normal cells. Indeed, there is an increasing body of evidence showing accumulation of CE in various types of cancer, including prostate cancer [88], breast cancer [229], leukemia [230, 231], glioblastoma [232], and pancreatic cancer [109]. These studies collectively support the importance of the cholesterol storage pathway in malignancy.

We observed reduced free monounsaturated fatty acid levels after ACAT inhibition. We suspect that as a consequence of inhibiting cholesterol esterification, free cholesterol level is increased, which downregulates SREBP activities through sterol-dependent negative feedback loop [8]. This is supported by our previous finding that expression and cleavage of SREBP-1c are reduced upon CE depletion [88]. As SREBP-1c is the isoform that mainly promotes fatty acid biosynthetic pathway [49, 50], our observation of decreased fatty acid levels after inhibiting cholesterol esterification is likely to be through the regulation of SREBP-1c. Importantly, it has been reported that depleting SREBP results in reduction in the monounsaturated fatty acids in the cellular pool of free fatty acids [233], which supports our hypothesis. As the enzyme catalyzing the rate-limiting step in unsaturated fatty acid synthesis, SCD1, is directly regulated by SREBP-1c [51, 52], it is possible that the level of monounsaturated fatty acids is reduced by downregulation of SCD1. Overall, given that SREBP-1 has been proposed to be an important regulator that provides a link between oncogenic signaling and tumor metabolism [233, 234], we believe that SREBP-1 plays an essential role in lipid homeostasis in during PCa progression.

Finally, our results reveal that lipid metabolism is an important regulator of Wnt activity. Several studies show that Wnt acylation by acyltransferase Porcupine is essential for its secretion and binding to membrane receptors [218, 221, 235]. In a recent study, alterations in the Wnt signaling pathway were observed in 18% of patients with metastatic castration-resistant PCa [236].

Interestingly, it was reported that patients with alterations in these genes are predicted to respond to Porcupine inhibitors, such as IWP-2 [235], which supports the importance of Wnt acylation in PCa progression. During acylation, a sufficient fatty acid pool is as critical as the expression of involved proteins. In support of this concept, overexpression of fatty acid synthase was shown to promote palmitoylation of Wnt protein in human prostate epithelial cells [237]. In our study, we show that palmitoleic acid level regulates Wnt secretion in PCa, which is essential for cell migration (**Figure 3.11** and **3.12**). Collectively, these results show an important crosstalk between lipid metabolism and Wnt signaling, which work cooperatively to promote PCa metastasis.

3. ASSESSING CHOLESTEROL STORAGE IN LIVE CELLS AND *C. ELEGANS* BY SRS IMAGING OF PHENYL-DIYNE CHOLESTEROL

The work presented in this chapter was published in *Scientific Reports* [189].

Here, we report a cholesterol imaging method using rationally synthesized phenyl-diyne cholesterol (PhDY-Chol) and SRS microscope. The phenyl-diyne group is biologically inert and provides a Raman scattering cross section that is 88 times larger than the endogenous C=O stretching mode. SRS microscopy offers an imaging speed that is faster than spontaneous Raman microscopy by three orders of magnitude, and a detection sensitivity of 31 μM PhDY-Chol (~1,800 molecules in the excitation volume). Inside living Chinese hamster ovary (CHO) cells, PhDY-Chol mimics the behavior of cholesterol, including membrane incorporation and esterification. In a cellular model of NP-C disease, PhDY-Chol reflects the lysosomal accumulation of cholesterol, and shows relocation to LDs after HPβCD treatment. In living *C. elegans*, PhDY-Chol mimics cholesterol uptake by intestinal cells and reflects cholesterol storage. Together, our work demonstrates an enabling platform for study of cholesterol trafficking in living cells and organisms.

3.1 Introduction

As an important component of cellular membrane, cholesterol controls physical properties of the membrane and contributes to specific membrane structures such as lipid rafts [1, 2]. Inside cells, cholesterol plays an important role in various signaling pathways [4, 5] serves as the precursor for signaling molecules, and modifies specific proteins, such as hedgehog, to control protein trafficking and activity [6]. The distribution of cholesterol in a living cell is highly regulated [8, 10]. Intracellular cholesterol is stored in LDs in the form of CE to avoid the toxicity caused by free cholesterol [62, 63]. Dysregulation of cholesterol metabolism and/or trafficking has been linked to diseases, including atherosclerosis [32, 62], NP-C disease [72], and various cancers [88, 238]. So far, our understanding of cholesterol transport and metabolism is limited, partly due to lack of suitable tools for imaging cholesterol in a living system [9].

Intracellular cholesterol transport and metabolism have been studied extensively using various reporter molecules [112], including cholesterol binding molecules and cholesterol analogs. Cholesterol binding molecules, such as cholesterol oxidase, filipin, and perfringolysin O derivatives, are commonly used to study steady-state distribution of cholesterol in fixed cells and tissues [113-115]. Fluorescent cholesterol, including intrinsic fluorescent sterols such as DHE and fluorophore-tagged analogs such as NBD-cholesterol and BODIPY-cholesterol are widely used *in vitro* and *in vivo* [117, 119, 120]. Radiolabeled cholesterol or its precursors are used in biochemical studies of metabolism and trafficking of cholesterol [112]. More recently, clickable cholesterol analogs were also developed for studying cholesterol-binding proteins and tracking cholesterol metabolism and distribution [122, 123].

These current cholesterol assays have limitations. Cholesterol oxidase is commonly used in fluorometric or colorimetric assays to quantify total cholesterol in homogenized cells. Radiolabeled cholesterol has to be used in combination with separation methods to determine intracellular cholesterol distribution indirectly. For imaging purpose, filipin is the most commonly used molecule for visualizing distribution of free cholesterol, but it is only applicable to fixed cells or tissues with moderate specificity because filipin also labels other lipids [239]. BODIPY-cholesterol is known to cause perturbations due to bulkiness of the fluorophores [121]. DHE has the closest structure as cholesterol, but its fluorescence undergoes rapid photo-bleaching [112], which impedes real-time observation of cholesterol trafficking. Clickable cholesterol analog requires additional steps before fluorescence imaging.

Owing to smaller volumes compared to fluorophores, Raman tags provide a promising way of imaging biomolecules like DNA and cytochrome c inside cells on a Raman microscope [185, 240]. These Raman tags utilize the vibrational signatures of the carbon-deuterium (C-D) bond, the cyano bond (C≡N) or the alkyne bond (C≡C) that are spectrally isolated from the endogenous Raman bands [241]. Spontaneous Raman imaging has allowed cellular trafficking of different C-D labeled lipid species in fixed cells [242], and direct visualization of alkyne-tagged DNA synthesis and cytochrome c release from mitochondria in living cells [185, 240] with an image acquisition speed of 50 min per frame of 127 × 127 pixels. To enhance the signal level, nonlinear vibrational microscopy based on the coherent Raman process has been developed [129] and deployed for

imaging C-D labeled fatty acids [141, 243], amino acids [179], and drugs [244] in living cells with a speed that is ~1,000 times faster than with spontaneous Raman microscopy. More recently, SRS imaging of alkyne-tagged molecules has been reported, with a detection limit at the level of hundreds of micromolar [186, 187]. SRS is a third order nonlinear optical process that involves two laser fields, namely, a pump field at ω_p and a Stokes field at ω_S. When the beating frequency ($\omega_p - \omega_S$) is tuned to excite a molecular vibration, the energy difference between ω_p and ω_S pumps the molecule from a ground state to a vibrationally excited state. In correspondence, the laser fields experience a weak decrease in pump beam intensity, called SRL, and a corresponding increase in Stokes beam intensity, called SRG. In the case of SRL, the Stokes beam intensity I_S is modulated and the pump beam intensity I_p is recorded by a photodiode. The induced modulation is often extracted by a lock-in amplifier. Theoretically, the modulation depth induced by SRL, I_{SRL}/I_p, is linearly proportional to the Raman cross section, σ, molar concentration of the target molecule, N, and the Stokes beam intensity, i.e., $I_{SRL}/I_p \propto \sigma N I_S$. SRS microscopy offers much faster imaging speed compared to spontaneous Raman microscopy [133].

Here, we report the synthesis of a Raman probe, PhDY-Chol, and its use for imaging cholesterol esterification, storage and trafficking inside living cells and vital organisms. By rational design and chemical synthesis, we prepared a probe molecule, PhDY-Chol, which gives a 2254 cm^{-1} Raman peak that is 88 times stronger than the endogenous C=O stretching band. Compared to alkyne-tagged cholesterol of which the IC_{50} is 16 μM, the phenyl-diyne group is biologically inert and did not cause cytotoxicity after 16 h incubation at 50 μM. In living CHO cells, SRS imaging showed incorporation into plasma membrane, esterification of PhDY-Chol by ACAT, and storage in LDs. In a cellular model of NP-C disease, PhDY-Chol is selectively accumulated in lysosomes and is esterified and relocated to LDs after treatment with a cholesterol-mobilization drug. In live *C. elegans*, SRS imaging of PhDY-Chol reflected cholesterol uptake through ChUP-1 regulated manner, and storage in the intestinal cells. These studies herald the potential of our method for unveiling intracellular cholesterol trafficking mechanisms and highly efficient screening of drugs that target cholesterol metabolism.

3.2 Experimental section

3.2.1 Calculation of Raman intensity

All calculations were performed at the HF/6-311G* level of theory. Geometry optimizations, vibrational frequencies and Raman intensities are obtained in Q-Chem electronic structure package [245]. Localized polarizabilities are calculated in the GAMESS quantum chemistry software [246].

3.2.2 Chemicals

3β-hydroxy-Δ5-cholenic acid was purchased from VWR. Lipoprotein-deficient serum was purchased from Biomedical Technologies Inc. Cholesterol, avasimibe, and filipin complex were purchased from Sigma-Aldrich. BODIPY-cholesterol was purchased from Avanti Polar Lipids, Inc. Propidium iodide, BODIPY, and LysoTracker were purchased from Life technologies.

3.2.3 Synthesis of Raman-tagged cholesterol

A series of tagged cholesterols – alkyne cholesterol (A-Chol, **5**), phenyl-alkyne cholesterol (PhA-Chol, **6**), phenyl-diyne cholesterol (PhDY-Chol, **7**), and cyano cholesterol (CN-Chol, **8**), was synthesized as shown in **Figure 4.1**. Our synthesis commenced with commercially available cholenic acid **3**. Using a sequence of THP-protection, $LiAlH_4$ reduction, Dess-Martin oxidation and Seyferth-Gilbert-Bestmann homologation, cholenic acid **3** was converted to compound **4** with a terminal alkyne group in excellent yield. Removal of the THP-protecting group gave probe **5**. We further prepared PhA-Chol **6** and PhDY-Chol **7** from compound **4** via a palladium-catalyzed Sonogashira reaction and a copper-catalyzed Cadiot-Chodkiewicz reaction, respectively, followed by acidic removal of THP group. Additionally, CN-Chol **8** was prepared from cholenic acid **3** via standard transformations.

Figure 3.1 Design and synthesis of tagged cholesterol probes.
Reagents and conditions:
a) DHP (5.0 equiv), p-TsOH (0.2 equiv), THF, RT, 91%;
b) $LiAlH_4$ (3.0 equiv), THF, 0 °C to RT, 98%;
c) DMP (3.0 equiv), $NaHCO_3$ (3.0 equiv), CH_2Cl_2, 0 °C, 86%;
d) dimethyl (1-diazo-2-oxopropyl)phosphonate (Bestmann reagent, 2.4 equiv), K_2CO_3 (4.0 equiv), THF/MeOH, RT, 99%;
e) p-TsOH (1.0 equiv), THF/MeOH, RT, 84%;
f) Iodobenzene (1.02 equiv), $PdCl_2(PPh_3)_2$ (0.05 equiv), CuI (0.05 equiv), TEA, RT; then p-TsOH (1.0 equiv), THF/MeOH, RT, 77%;
g) CuI (0.1 equiv), K_2CO_3 (2.0 equiv), $P(o\text{-}Tol)_3$ (0.2 equiv), phenyl bromoacetylene (1.3 equiv), EtOH, 100 °C, 51%;
h) p-TsOH (1.0 equiv), THF/MeOH, RT, 95%;
i) MsCl (3.0 equiv), TEA (3.0 equiv), CH_2Cl_2, 0°C to RT, 75%;
j) KCN (2.0 equiv), DMSO, 90°C, 76%;
k) p-TsOH (1.0 equiv), THF/MeOH, RT, 74%. DHP = 3,4-Dihydro-2H-pyran, DMP = Dess-Martin Periodinane, p-TsOH = p-Toluenesulfonic acid, TEA = triethylamine, $P(o\text{-}Tol)_3$ = tri(o-tolyl)phosphine, MsCl = methanesulfonyl chloride.
CN: cyano; A: alkyne; PhA: phenyl-alkyne; PhDY: phenyl-diyne; Chol: cholesterol.

Raman Probe Design:

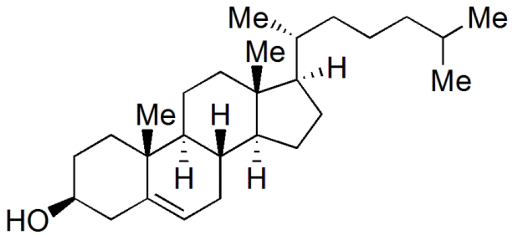

Cholesterol (**1**)

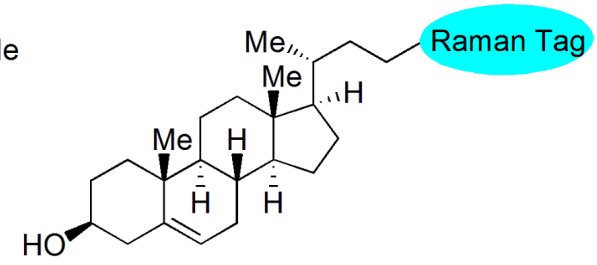

Tagged-cholesterol (**2**)

Raman Probe Synthesis:

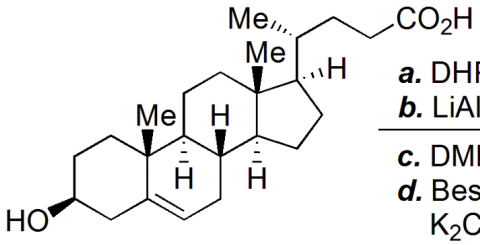

cholenic acid (**3**)

a. DHP, *p*-TsOH, 91%
b. $LiAlH_4$, 98%
c. DMP, 86%
d. Bestmann Reagent
K_2CO_3, MeOH
99%

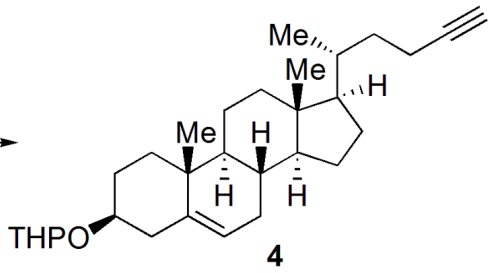

4

e. TsOH, 84% (R = H)

or ***f.*** PhI, $PdCl_2(PPh_3)_2$,
CuI, TEA, r.t.
then TsOH
77% (R = Ph)

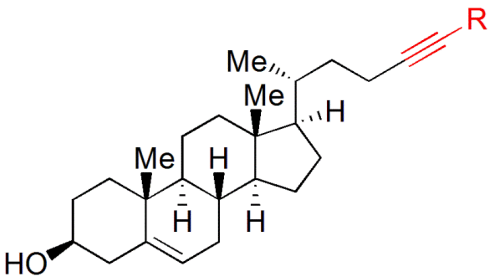

A-Chol (R = H, **5**)
PhA-Chol (R = Ph, **6**)

g. CuI, K_2CO_3,P(*o*-Tol)$_3$
Ph—≡—Br
51%

h. TsOH, 95%

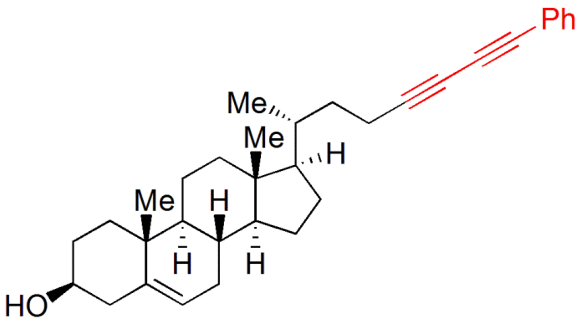

PhDY-Chol (**7**)

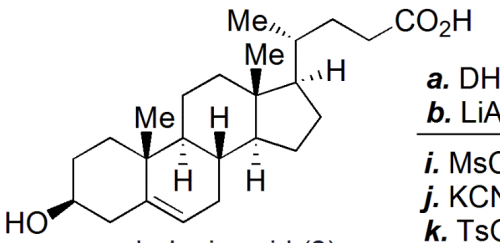

cholenic acid (**3**)

a. DHP, *p*-TsOH, 91%
b. $LiAlH_4$, 98%
i. MsCl, NEt_3, 75%
j. KCN, 76%
k. TsOH, 74%

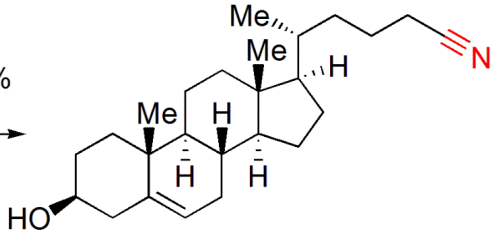

CN-Chol (**8**)

3.2.4 Solubilization of tagged cholesterol

To solubilize the tagged cholesterol molecules, the following procedure was used to prepare a stock solution of 10 mM cholesterol probe molecules. The appropriate amount of cholesterol probe powder was dissolved in 100% ethanol to make a 20 mM-solution. The tube was vortexed and then sonicated in bath sonicator for 2 min. The same volume of DMSO was added into the tube, vortexed, and then sonicated in bath sonicator for 2 min. BODIPY-cholesterol was prepared with the same procedure. For SRS imaging and Raman spectral analysis of tagged cholesterol solutions, cholesterol probe molecules were prepared in cyclohexanone at 50 mM. The tube was vortexed and then sonicated in bath sonicator for 2 min. 1 µL of the solution was taken to prepare cover glass samples immediately before use.

3.2.5 Cell culture and PhDY-Chol treatment

CHO-K1 cells and M12 cells (mutant CHO-K1 cells that contain a deletion of the NPC1 locus [247]) were kindly provided by Dr. Daniel Ory, and were grown in a monolayer at 37˚C in 5% CO_2 in DMEM/F-12 medium supplemented with 10% (vol/vol) FBS. To incubate cells with PhDY-Chol, cells were pre-incubated in DMEM/F-12 medium supplemented with 4.4% lipoprotein-deficient serum to deplete medium cholesterol for 16 hr. The cells were then incubated with PhDY-Chol containing medium (DMEM/F-12 + 4.4% lipoprotein-deficient serum + 50 µM PhDY-Chol) for 16 h to 24 hr. Cells were rinsed with 1x PBS buffer three times before the next procedure.

3.2.6 Raman spectromicroscopy

The background of Raman spectrum was removed as described [200]. Each Raman spectrum of tagged cholesterol solution was acquired in 10 seconds, and each Raman spectrum of fluorescence stained cells was acquired in 30 seconds. On the same microscope, TPEF imaging was performed with 707 nm laser with 100 mW power. Backward-detected two-photon fluorescence signal was collected through a 425/40 nm or 522/40 nm band-pass filter for imaging filipin or BODIPY fluorescence, respectively.

3.2.7 SRS microscopy

SRS imaging was performed on a femtosecond SRL microscope, with the laser beating frequency tuned to the C≡C vibration band at 2252 cm^{-1}, or to the C-H vibration band at 2885 cm^{-1}, as described previously [141]. The laser power at the specimen was maintained at 75 mW, and no cell or tissue damage was observed. For off-resonance, 2099 cm^{-1} was used. On the same microscope, TPEF imaging was performed with 843 nm laser with 30 mW power. Forward-detected two-photon fluorescence signal was collected through an appropriate band-pass filter for imaging filipin, BODIPY, or LysoTracker.

3.2.8 ACAT-1 inhibition

ACAT-1 inhibition was used to block cholesterol esterification either by adding a potent ACAT inhibitor, avasimibe, or by RNA interference with ACAT-1 shRNA plasmid. Avasimibe: Cells were pre-treated with avasimibe at a final concentration of 10 μM for 24 hr. Then PhDY-Chol containing medium with 10 μM avasimibe was added into the cells and incubated for 24 hr. RNA interference: RNA interference was employed to specifically inhibit endogenous ACAT-1. The ACAT-1 shRNA plasmid was purchased from Santa Cruz (sc-29624-SH). shRNA plasmid was transfected with Lipofectamine®2000 (Invitrogen 11668030) as described in the manufacturer's protocols.

3.2.9 hydroxypropyl β-cyclodextrin (HPβCD) treatment

HPβCD was used as a drug treatment of NP-C disease. M12 cells were incubated with PhDY-Chol for 16 hr as described above. Then cells were treated with 500 μM HPβCD for 30 hr.

3.2.10 Cell viability assay

CHO cells were grown in 96-well plates with density of 4,000 cells per well. The next day, the cells were treated with each cholesterol probe at the indicated concentrations for 48 hr. Cell-viability was measured with the MTT colorimetric assay (Sigma).

3.2.11 Propidium iodide staining

Propidium iodide was used to stain late apoptotic or necrotic cells. CHO cells were incubated with 30 μM of tagged cholesterol molecules for 24 hr. The propidium iodide staining was performed following protocols provided by the manufacturer (Life Technologies).

3.2.12 Fluorescent staining of free cholesterol, LDs, and lysosomes

Filipin was used to stain free cholesterol. Cells were fixed with 10% formalin solution (Sigma) for 1 hr at room temperature. 1.5 mg/mL glycine in PBS was used to quench the formalin by incubating the fixed cells for 10 min at room temperature. To stain the cells with filipin, working solution of 0.05 mg/mL of filipin in PBS/10% FBS was used to incubate cells for 2 hr at room temperature. BODIPY was used to label LDs. Cells were incubated with 10 μg/mL of BODIPY for 30 min at room temperature. LysoTracker Yellow-HCK-123 was used to stain lysosomes following protocols provided by the manufacturer (Life Technologies). Cells were rinsed with PBS three times before TPEF imaging.

3.2.13 *C. elegans* strains

The N2 Bristol was used as wild-type strain. VC452 strain with chup-1(gk245) X genotype was used to study PhDY-Chol uptake. VS17 strain with hjIs9 [ges-1p::glo-1::GFP + unc-119(+)] genotype was used to study cholesterol storage in worms.

3.2.14 PhDY-Chol uptake into *C. elegans*

PhDY-Chol uptake procedure was modified from a previously reported procedure [119]. Briefly, 500 μM of PhDY-Chol in DMSO was spread on the NGM plates seeded with an *E. coli* OP50 lawn and allowed to grow overnight at room temperature. *C. elegans* was then transferred to PhDY-Chol containing plates and grown for 3 days before SRS imaging.

3.2.15 Statistical analysis

To quantify PhDY-rich area, we first selected one cell and used “Threshold” function to select PhDY-rich cellular regions using ImageJ. Then, by using “Analyze Particles” function, the area fraction (%) of PhDY-rich region was obtained. To quantify PhDY-rich LDs, “Image Calculator” function in ImageJ was used to multiply SRS image of PhDY-Chol by TPEF image of BODIPY. Then, after using “Threshold” function to select PhDY-rich LDs, the number of PhDY-rich LDs was counted by “Analyze Particles” function. For each group, 7 cells were analyzed, and results were shown as mean ± SD. Student’s t-test was used for all the comparisons. $p < 0.05$ was considered statistically significant.

3.3 Results

3.3.1 Rational design and synthesis of tagged cholesterol with an extremely large Raman scattering cross section

In order to design a probe molecule that not only maintains physiological functions of cholesterol, but also has a large Raman scattering cross section, we chose to replace the aliphatic side chain of cholesterol with a cyano or an alkynyl group (**Figure 4.1**). These groups have small size, which could minimize structural perturbation of the molecule of interest, in this case, cholesterol. Meanwhile, these groups produce strong Raman scattering peaks in a cellular silent region (1800 – 2800 cm^{-1}) [240, 241] and therefore, can potentially be used for Raman imaging in a low-concentration condition. It has been reported that as the chain length increases, the hyperpolarizability increases in polyynes [248]. Also, aromatic ring capped alkyne was shown to give stronger Raman signals than terminal alkyne [185]. To design tagged cholesterol with very strong Raman intensity, we calculated the Raman cross section of potential tags, namely alkyne, phenyl-alkyne, diyne, and phenyl-diyne, using the Q-Chem and GAMESS electronic structure packages to provide insight of the relation between molecular structure and Raman intensity. Our results show that the localized polarizabilities on each C≡C moiety increase with the number of conjugated triple bonds, as well as with addition of a phenyl ring (**Figure 4.2A and Table 4.1**). Thus, the total polarizability of the molecule increases as a result of the additive effect as well as non-linear boost in the polarizability of conjugated bonds. The phenyl ring serves as both a donor and an acceptor of π-electrons from the neighboring triple bonds, further escalating polarizabilities of neighboring conjugated bonds. Taking into account that the Raman intensity is proportional to squares of polarizability derivatives, the additional three-fold enhancement of the total polarizability due to conjugation results in a ~10-fold boost in Raman intensity. Together, compared to the alkyne group, the Raman intensity increases by 9 times by adding a phenyl group to the terminal alkyne, and 52 times by conjugating a phenyl group and another alkyne (**Figure 4.2B**). Based on the above considerations, we have synthesized a series of tagged cholesterols – alkyne cholesterol (A-Chol, **5**), phenyl-alkyne cholesterol (PhA-Chol, **6**), phenyl-diyne cholesterol (PhDY-Chol, **7**), and cyano cholesterol (CN-Chol, **8**), as shown in **Figure 4.1**.

Figure 3.2 Theoretical Raman intensities of the C≡C stretching mode in various tags. The total molecular polarizability is broken down in terms of the value of the polarizability corresponding to each bond in the molecule. The Raman scattering cross section arises from the polarizability caused by conjugation of the π-electrons of the alkyne and the phenyl groups. The π-orbitals possess large polarizability tensors, such that the polarizability of the triple bond is mainly determined by the polarizability of π-orbitals. (A) Depiction of symmetry-localized π-orbitals in C_4H-C_6H_5 (C≡C-C≡C-Ph). The distributed polarizabilities corresponding to the localized orbitals on C≡C and phenyl ring are shown in **Table 4.1**, such that the polarizabilities of orbitals 1 and 2 determine the total polarizability of the left C≡C bond, polarizabilities of orbitals 3 and 4 sum up to the polarizability of the middle C≡C bond. Additionally, the closest to alkyne part of the ring (orbital 5) exhibits significant change in polarizability along triple-bond stretching vibration, and therefore polarizabilities corresponding to this orbital are included in the total count of polarizability of the triple-bond system. Distributed polarizabilities are calculated using GAMESS electronic structure package [246]. (B) Comparison of C≡C stretching Raman intensities in various tags computed using the Q-Chem quantum chemistry software [245]. Intensities were normalized to the highest intensity.

A

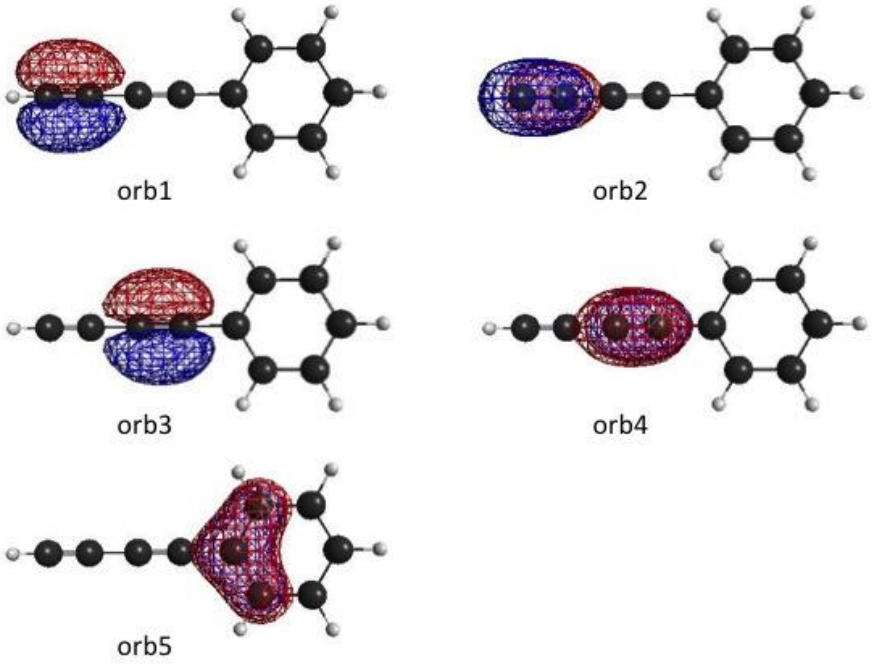
orb1
orb2
orb3
orb4
orb5

B

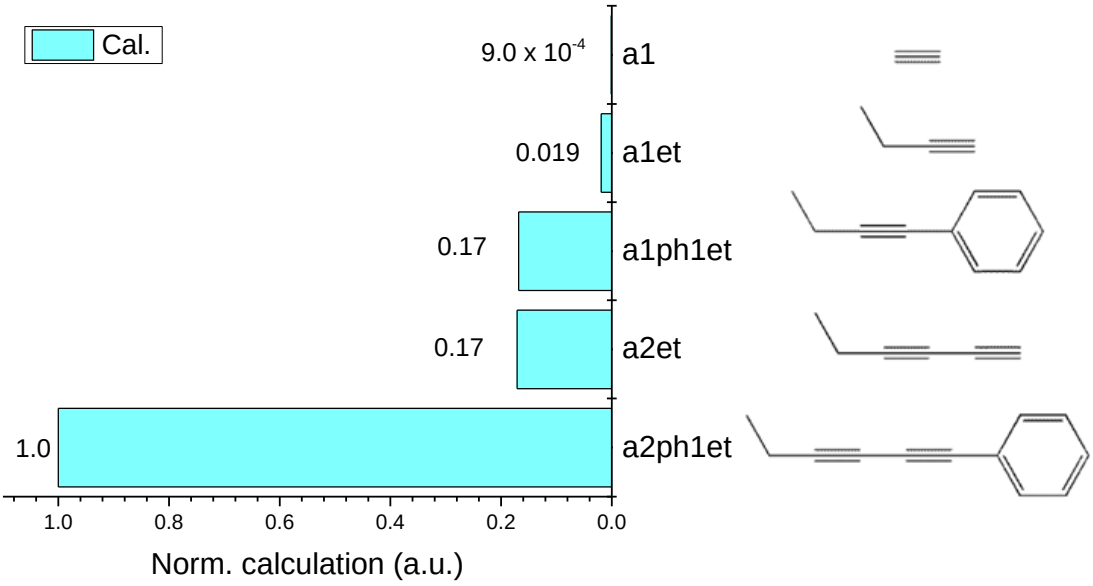
Cal.
9.0 x 10-4
a1
0.019
a1et
0.17
a1ph1et
0.17
a2et
1.0
a2ph1et
1.0
0.8
0.6
0.4
0.2
0.0
Norm. calculation (a.u.)

Table 3-1 Distributed polarizabilities of C≡C and phenyl moieties calculated as sums of polarizabilities of localized π-orbitals in various tags[b]

	XX[a]	average
C≡C	**2.82**	**1.60**
C≡C-Ph	**7.42**	**3.76**
C≡C	4.62	2.15
Ph	2.80	1.61
C≡C-C≡C	**8.70**	**3.54**
C≡C	4.35	1.77
C≡C	4.35	1.77
C≡C-C≡C-Ph	**16.70**	**7.37**
left C≡C	5.77	2.51
middle C≡C	7.20	2.95
Ph	3.73	1.91

[a] XX: the largest components

[b] The total polarizability of π-conjugated system increases as a result of the additive effect as well as non-linear boost in the polarizability of conjugated bonds.

3.3.2 Raman spectral analysis and SRS imaging of tagged cholesterol

To determine the Raman shift of the C≡C stretching vibrational mode and to compare the level of Raman signals from the tagged cholesterols, we prepared 50 mM of each compound in cyclohexanone and performed confocal Raman spectral analysis (**Figure 4.3**). The signal from CN-Chol was too weak to be detected. A-Chol showed its peak for C≡C vibrational mode at 2122 cm^{-1}; PhA-Chol at 2239 cm^{-1}; PhDY-Chol at 2254 cm^{-1} (**Figure 4.3A**). To evaluate the amplitude of the Raman scattering cross section, we fitted each Raman band with a Lorentzian profile and calculated the area under the fitted profile. Compared to the Raman peak of each tag to the 1714 cm^{-1} C=O Raman peak from the solvent (9.7 M for pure cyclohexanone), the alkyne, PhA, and PhDY groups were found to be 6, 15, and 88 times stronger in Raman cross section, respectively (**Figure 4.3B**). This result showed that the PhDY tag produces a spectrally-isolated peak, which is stronger than the C=O vibrational mode by two orders of magnitude.

To determine the SRS imaging sensitivity for PhDY-Chol, we used a femtosecond SRL microscope reported elsewhere [141]. Cyclohexanone solutions of PhDY-Chol were prepared by serial dilution, and SRS images of PhDY-Chol were recorded with the laser beating frequency tuned to be resonant with C≡C vibration at 2254 cm^{-1}. In solutions without PhDY-Chol, a residual background was detected, caused by cross-phase modulation. The SRS contrast, defined as (S – B) / B, where S and B denote SRS signal and background, was calculated as a function of PhDY-Chol molar concentration. At the speed of 200 µs per pixel, a linear relationship was observed (**Figure 4.3C**) and 13% and 4% contrasts were reached at 313 µM and 156 µM, respectively. To increase the detection sensitivity, we chirped the femtosecond lasers to 0.8 picoseconds with a SF-10 glass rod. This spectral focusing approach [151] maintained 85% of the SRS signal while reduced the cross-phase modulation background level by 3 times, to a level of 6.3×10^{-7} in terms of modulation depth. As a result, the SRS contrast became 14% at 31 µM, corresponding to ~1,800 molecules in the excitation volume (**Figure 4.3D**). We also depicted the modulation depth (ΔI/I) as a function of molar concentration (**Figure 4.4**), which is used for estimating the molar concentration of PhDY-Chol inside cells in following studies.

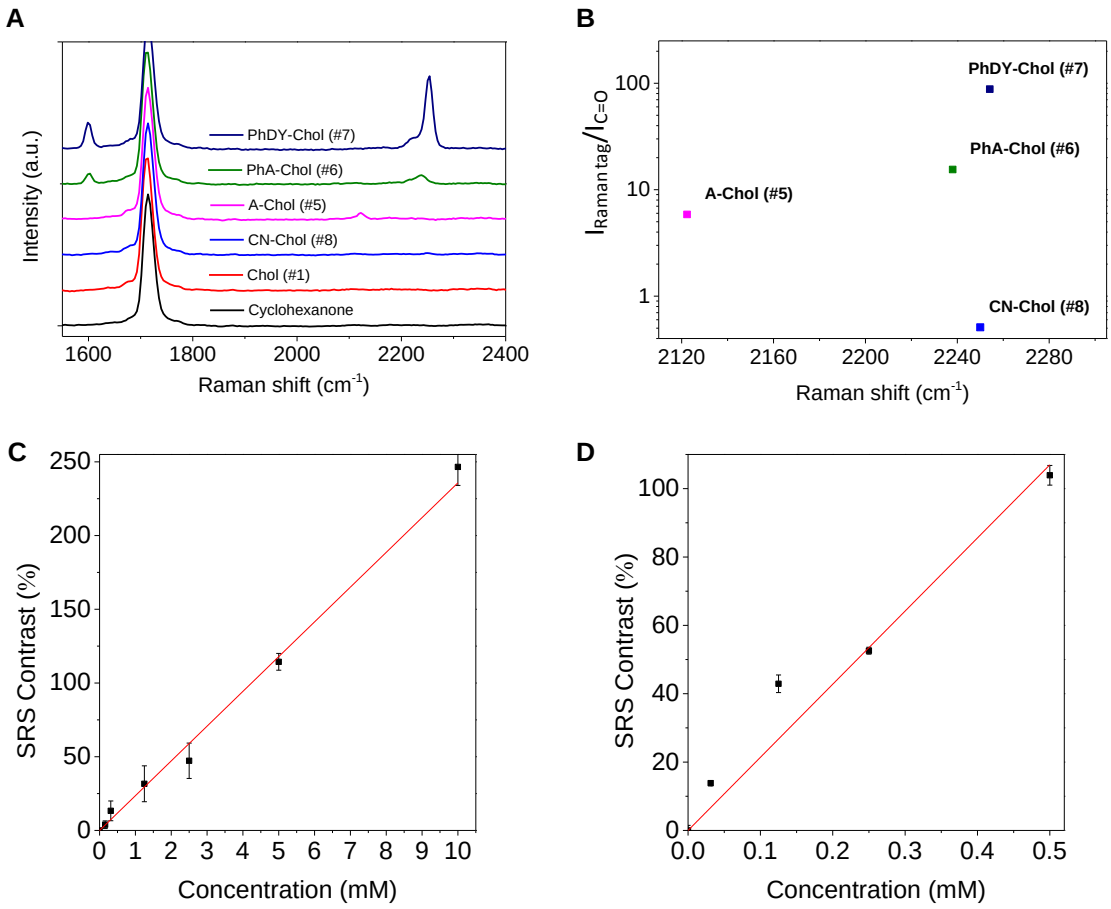

Figure 3.3 Raman spectral analysis of tagged cholesterol and SRS detection of PhDY-Chol. (A) Raman spectra of 50 mM tagged cholesterols in cyclohexanone (solvent). Spectral intensity was normalized by C=O vibration band at 1714 cm^{-1}. Spectral acquisition time: 10 s. (B) Plot of relative intensity of Raman tags versus solvent and Raman shifts of tagged cholesterols. Based on the molar concentration of the molecules (50 mM) and the solvent (9.7 M), the Raman cross section of C≡C from A-Chol, PhA-Chol, and PhDY-Chol are 6 times, 15 times, and 88 times larger than the C=O band from the solvent, respectively. CN: cyano; A: alkyne; PhA: phenyl-alkyne; PhDY: phenyl-diyne; Chol: cholesterol. (C) SRS contrast versus concentration plot of PhDY-Chol solutions. 13% contrast was reached at 313 µM and 4% contrast was reached at 156 µM. Image acquisition speed: 200 µs per pixel. Data represents the mean ± SEM in 3 measurements. $R^2 = 0.996$. (D) SRS contrast versus concentration plot of PhDY-Chol solutions using chirped femtosecond lasers with spectral focusing approach. 14% contrast was reached at 31 µM. Image acquisition speed: 200 µs per pixel. Data represents the mean ± SEM in 3 measurements. $R^2 = 0.980$. Contrast was defined as (S - B) / B. S: SRS signal; B: background.

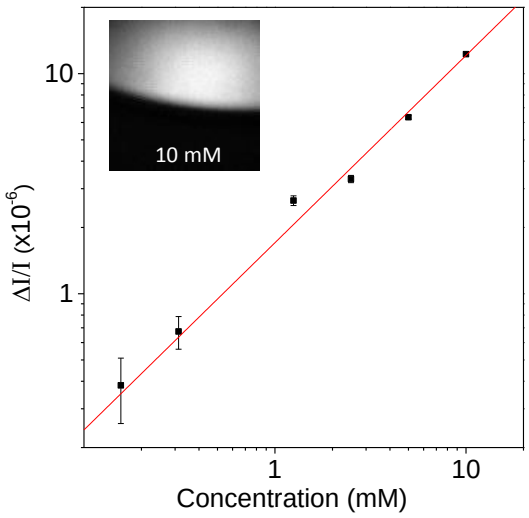

Figure 3.4 Linear correlation between PhDY-Chol concentration and modulation depth. Concentration of PhDY-Chol and modulation depth (ΔI/I) show linear correlation, which can be expressed as: $y = 0.85x - 5.77$ ($R^2 = 0.98$). Inset is an SRS image of 10 mM PhDY-Chol in cyclohexanone. Data acquisition speed: 200 µs per pixel. Error bars represent SEM.

3.3.3 Cytotoxicity caused by terminal alkyne is avoided by phenyl group

To evaluate the cytotoxicity of tagged cholesterols, we performed MTT cell-viability assays after treating CHO cells with tagged cholesterol. Various concentrations of tagged cholesterol were added to the culture media and the cells were incubated for 48 hr before the assays were conducted. A-Chol was found to be toxic to the cells with IC_{50} of 16 µM. Importantly, adding a phenyl group effectively reduced the cytotoxicity (**Figure 4.5A**). To directly visualize the toxic effect, we stained the cells with propidium iodide for late apoptosis and necrosis. Cells incubated with A-Chol showed reduced density and extensive apoptosis, whereas both PhA-Chol and PhDY-Chol caused minimum cell death (**Figure 4.5B**). This result presents another important role of the phenyl group, which is to reduce the toxicity caused by terminal alkyne. Based on the signal level and the severity of toxicity, we conclude that PhDY-Chol is the most suitable cholesterol analog for live-cell imaging, and we used PhDY-Chol in subsequent experiments.

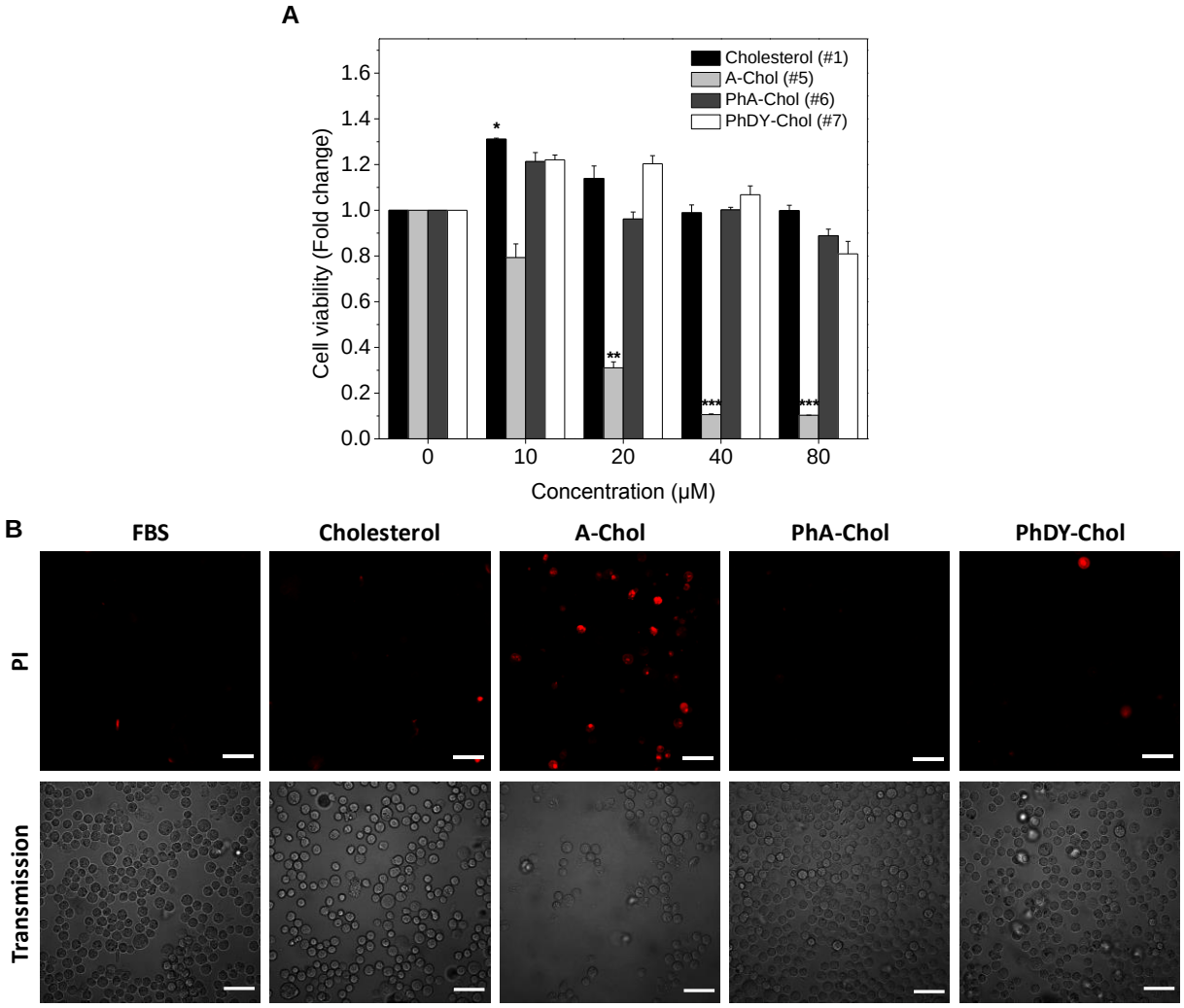

Figure 3.5 Phenyl group prevented cytotoxicity of the probe molecules.
(A) MTT Cell-viability assays. CHO cells were incubated with each probe in various concentrations for 48 hr before MTT cell-viability assays were conducted. Error bars represent SEM. n > 3, *: $p < 0.05$; **: $p < 0.005$; ***: $p < 0.0005$. (B) Propidium iodide staining for visualizing apoptosis and necrosis. Transmission images show reduced cell number in A-Chol treated CHO cells. A-Chol: alkyne cholesterol; PhA-Chol: phenyl-alkyne cholesterol; PhDY-Chol: phenyl-diyne cholesterol; PI: propidium iodide. Scale bar: 50 μm.

3.3.4 Membrane incorporation and esterification of PhDY-Chol in living cells

We chose CHO cells which are commonly used for cholesterol trafficking and metabolism studies [249]. To enhance cellular uptake of PhDY-Chol, the cells were pre-incubated in medium supplemented with lipoprotein-deficient serum to deplete medium cholesterol, after which the cells were incubated with 50 μM PhDY-Chol for 16 hr. By tuning the laser beating frequency to be

resonant with C≡C vibration (2254 cm^{-1}), SRL signals arose from PhDY-Chol. We also tuned the laser to be resonant with C-H vibration (2885 cm^{-1}) and obtained signals from C-H-rich lipid structures, such as LDs.

To show the incorporation of PhDY-Chol into the plasma membrane, we performed spectral focusing SRS imaging of living CHO cells after treating with PhDY-Chol for 1 hr with 6 µs per pixel speed. PhDY-Chol in the membrane was detected in the on-resonance image, and the contrast disappeared in the off-resonance image (**Figure 4.6A**). The membrane incorporation was confirmed by filipin staining of free cholesterol and Raman spectral analysis (**Figure 4.6B** and **C**). By focusing at the filipin-stained membrane, we have obtained the Raman spectrum showing the C=C band from filipin (**Figure 4.6D**), the amide I band from protein, and the C≡C band from the PhDY (**Figure 4.6C**). Inside living CHO cells, PhDY-Chol was colocalized with LDs found in the C-H vibrational region (**Figure 4.7A**). This colocalization was confirmed by TPEF imaging and Raman spectral analysis of BODIPY-stained LDs in fixed CHO cells. (**Figure 4.8**). The Raman spectra of the BODIPY-labeled LDs showed a 702 cm^{-1} peak from cholesterol ring and the C≡C band from the PhDY (**Figure 4.8B**), which further supports the localization of PhDY-Chol in LDs. Importantly, high imaging speed offered by SRS microscopy allowed real-time imaging of the trafficking of PhDY-Chol containing LDs within living cells.

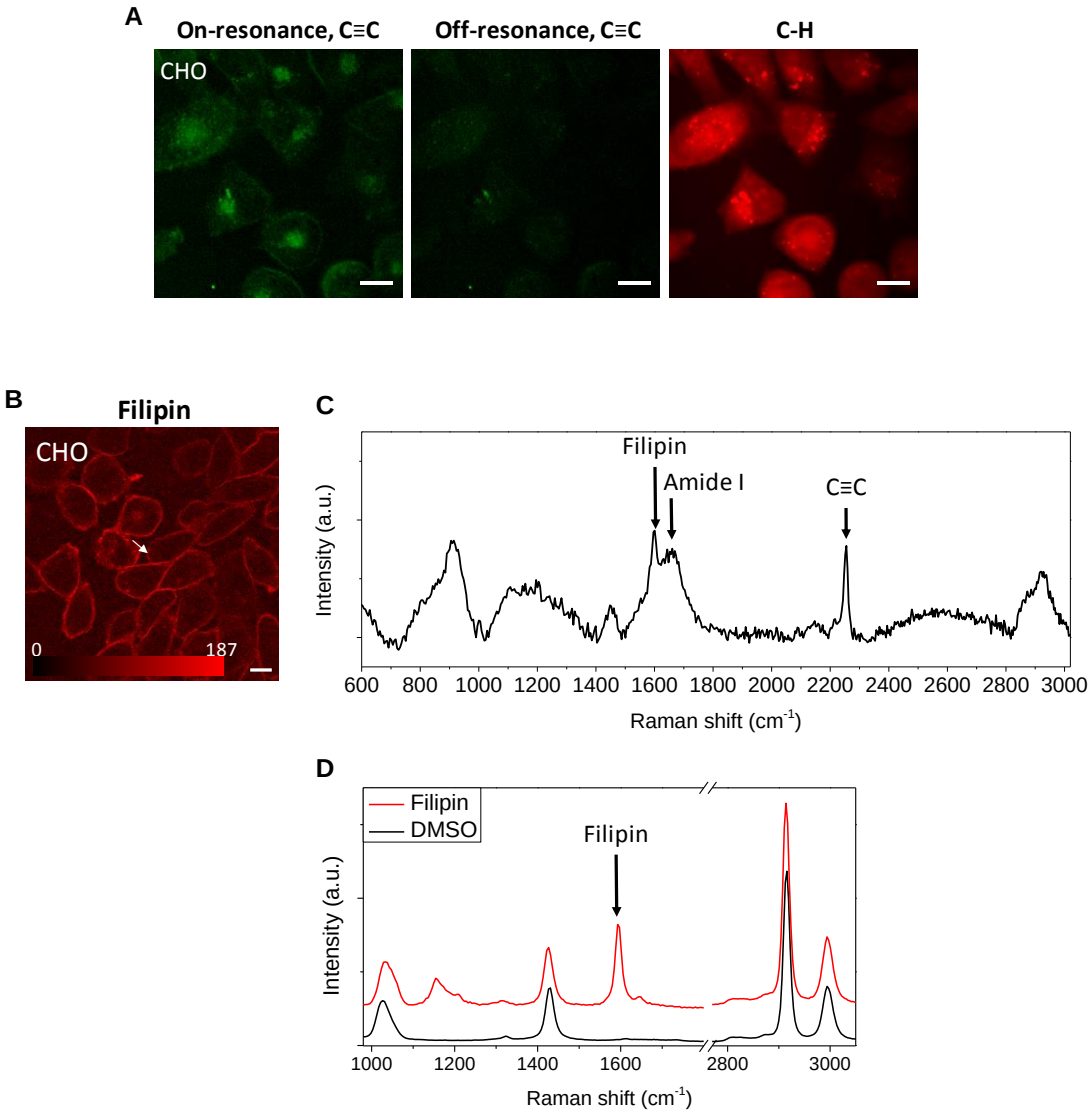

Figure 3.6 PhDY-Chol is incorporated into cellular membrane.
(A) SRS images of living CHO cells treated with PhDY-Chol for 1 hr. PhDY-Chol was seen in plasma membrane and intracellular structures. Data acquisition time: 6 µs per pixel for 512 × 512 pixels. Scale bar: 10 µm. (B) TPEF image of filipin-labeled CHO cells. Arrow indicates the point used for Raman spectral analysis. Red intensity bar represents the relative intensity of fluorescence. Scale bar: 10 µm. (C) Raman spectrum of filipin-labeled cell membrane acquired on the same TPEF microscope. The bands for filipin, protein (amide I), and C≡C vibrational mode are indicated by black arrows. Spectrum acquisition time: 30 s. (D) Raman spectrum of filipin and the solvent, DMSO. The bands for filipin is indicated by black arrows. Spectrum acquisition time: 10 s

Figure 3.7 SRS images of PhDY-Chol in living CHO cells and blockage of PhDY-Chol storage into LDs via ACAT inhibition.

(A) SRS images of living CHO cells treated with PhDY-Chol (50 μM) for 16 hr. C≡C vibrational mode at 2254 cm^{-1} was used for PhDY-Chol, and C-H vibrational mode at 2885 cm^{-1} was used for C-H-rich lipid structures. Lasers were also tuned away to 2099 cm^{-1} to show specificity of PhDY-Chol signal inside the cells. PhDY-Chol was found to accumulate in LDs (arrows). Image acquisition speed: 10 μs per pixel for 512 × 512 pixels. Scale bar: 10 μm. (B) Schematic graph showing the hypothesis of PhDY-Chol metabolism inside the cells. ACAT: Acyl-CoA:cholesterol acyltransferase. (C) SRS images of PhDY-Chol in CHO cells and ACAT inhibited CHO cells by avasimibe treatment. As shown in circles, PhDY-Chol was stored in LDs in CHO cells, but not in avasimibe treated CHO cells. Image acquisition speed: 100 μs per pixel for 400 × 400 pixels. Scale bar: 10 μm. Intensity bars in A and C show the ΔI/I of the SRS image. (D) Quantification of PhDY-rich and BODIPY-rich LDs in CHO cells before and after ACAT inhibition. The number of the LDs was normalized by the control group (n = 7). Error bars represent SD. *: $p < 0.05$. (E) TPEF images of BODIPY-cholesterol and SRS images C-H-rich structures in CHO cells and ACAT inhibited CHO cells. As shown in circles, BODIPY-cholesterol showed no difference between the two groups. Scalar bar: 10 μm.

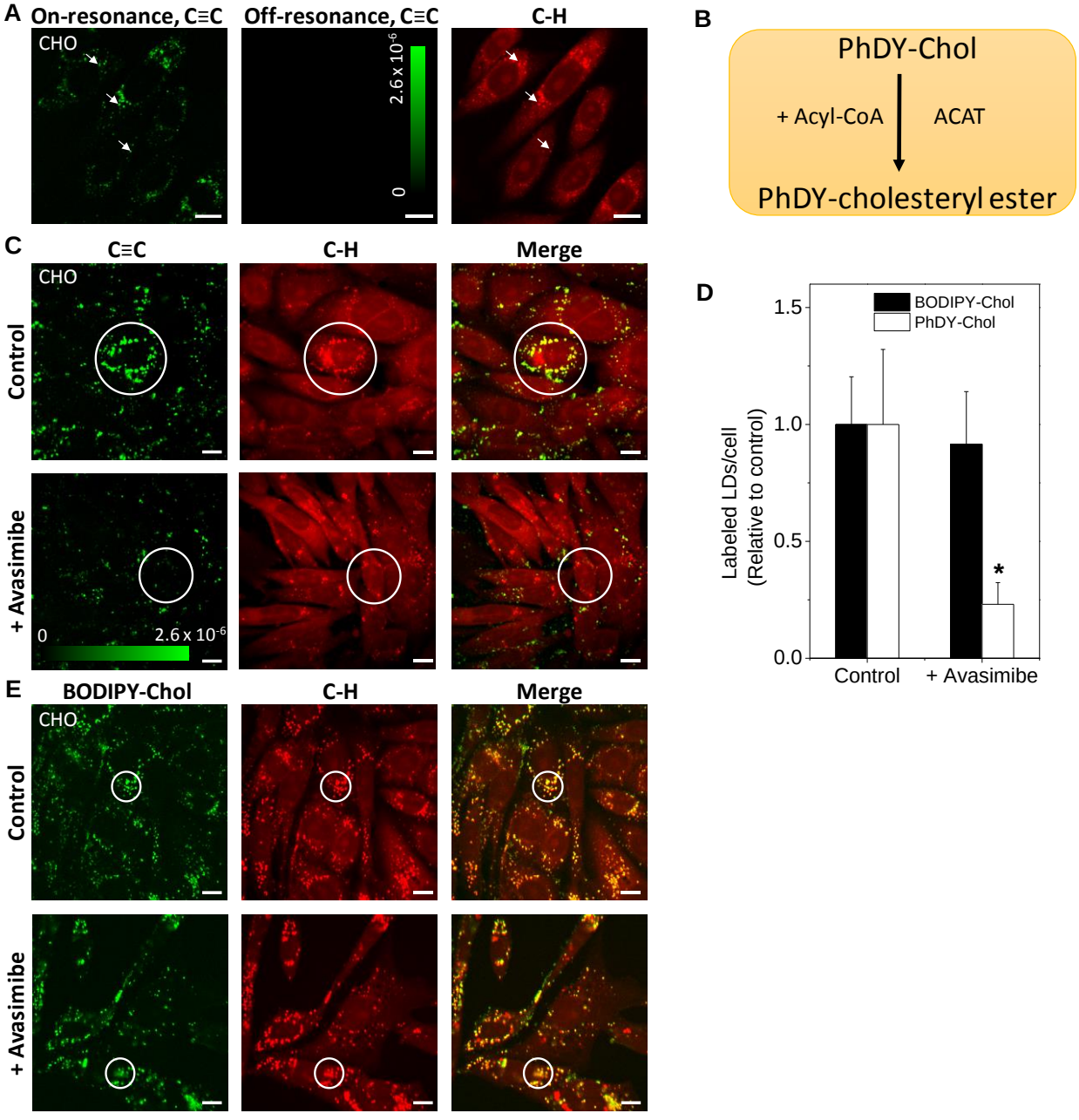
A
On-resonance, C≡C
Off-resonance, C≡C
C-H
CHO
2.6 x 10-6
0
B
PhDY-Chol
+ Acyl-CoA
ACAT
PhDY-cholesteryl ester
C
C≡C
C-H
Merge
Control
+ Avasimibe
0
2.6 x 10-6
D
BODIPY-Chol
PhDY-Chol
Labeled LDs/cell
(Relative to control)
1.5
1.0
0.5
0.0
*
Control
+ Avasimibe
E
BODIPY-Chol
C-H
Merge
Control
+ Avasimibe

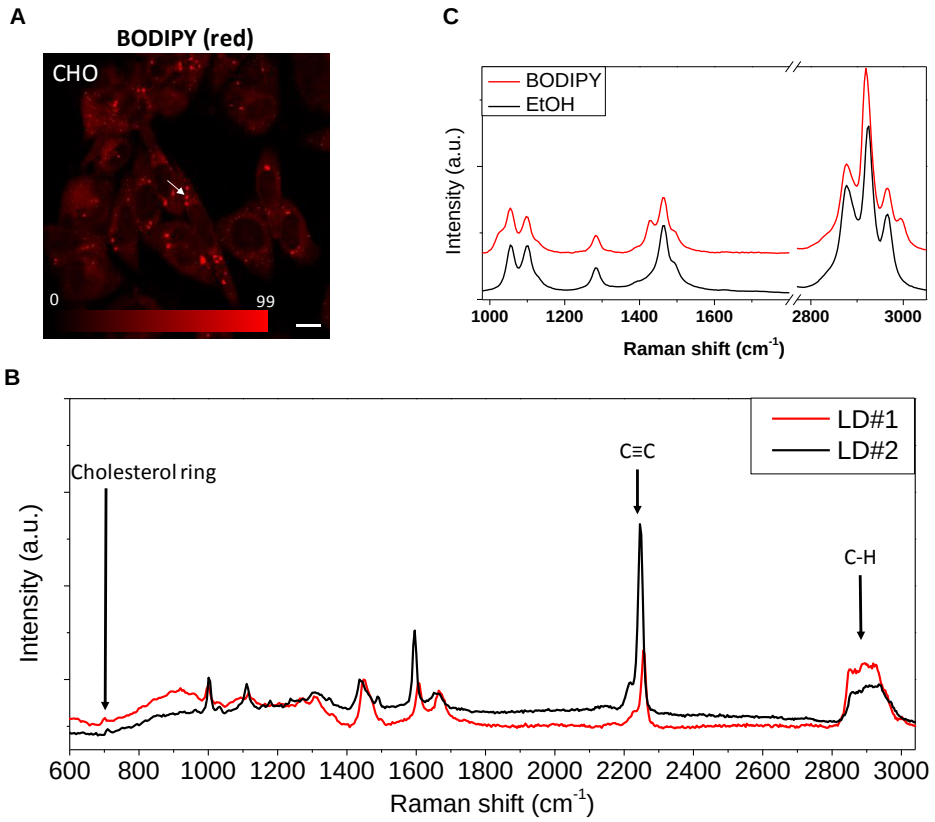

Figure 3.8 TPEF imaging and Raman spectral analysis to confirm PhDY-Chol storage into LDs. (A) TPEF image of BODIPY-labeled CHO cells. Arrow indicates the point used for Raman spectral analysis. Red intensity bar represents the relative intensity of fluorescence. Scale bar: 10 µm. (B) Raman spectrum of BODIPY-labeled LDs acquired on the same TPEF microscope. The bands for cholesterol ring, BODIPY, C≡C, and C-H vibrational modes are indicated by black arrows. Two representative spectra of LDs are shown. Spectrum acquisition time: 30 s. (C) Raman spectrum of BODIPY and the solvent, ethanol. Spectrum acquisition time: 10 s.

It is important to note that PhDY-Chol-rich structures inside the CHO cells could not be stained by filipin (**Figure 4.6B**), implicating that it is not in the free form. We hypothesize that PhDY-Chol is converted into PhDY-CE, by ACAT, the enzyme responsible for cholesterol esterification [63] (**Figure 4.7B**). To confirm the esterification of PhDY-Chol, we inhibited ACAT with avasimibe for 24 hr before addition of PhDY-Chol. After blocking cholesterol esterification, the amount of PhDY-Chol storage found in CHO cells significantly decreased (**Figure 4.7C**). Although LDs were still visible, the amount of PhDY-Chol signal found inside LDs reduced by 4 times (**Figure 4.7D**). ACAT-1 knockdown by shRNA was also conducted to specifically inhibit the enzyme. Similarly, we found decreased amount of PhDY-Chol in ACAT-1 knocked down CHO cells, and the amount of PhDY-Chol in LDs reduced significantly (**Figure 4.9A**). To

determine where PhDY-Chol accumulates after ACAT inhibition, we stained the cells with LysoTracker for lysosomes. Our result indicates that after ACAT inhibition, PhDY-Chol is partially located in lysosomes (**Figure 4.9B**). Collectively, these results show that PhDY-Chol can be transported into cells, converted into PhDY-CE by ACAT-1, and stored in LDs following the normal metabolic pathway of cholesterol. To emphasize the physiological compatibility of our PhDY tag, we treated CHO cells with BODIPY-cholesterol. The amount of BODIPY-cholesterol incorporated into LDs did not change after ACAT inhibition (**Figure 4.7D** and **E**), indicating that BODIPY-cholesterol directly labels the LDs without metabolic conversion into CE. It is known that excess cholesterol inside cells is stored into LDs through cholesterol esterification by ACAT proteins [63]. Therefore, PhDY-Chol reflects the intracellular cholesterol metabolism more faithfully compared to BODIPY-cholesterol.

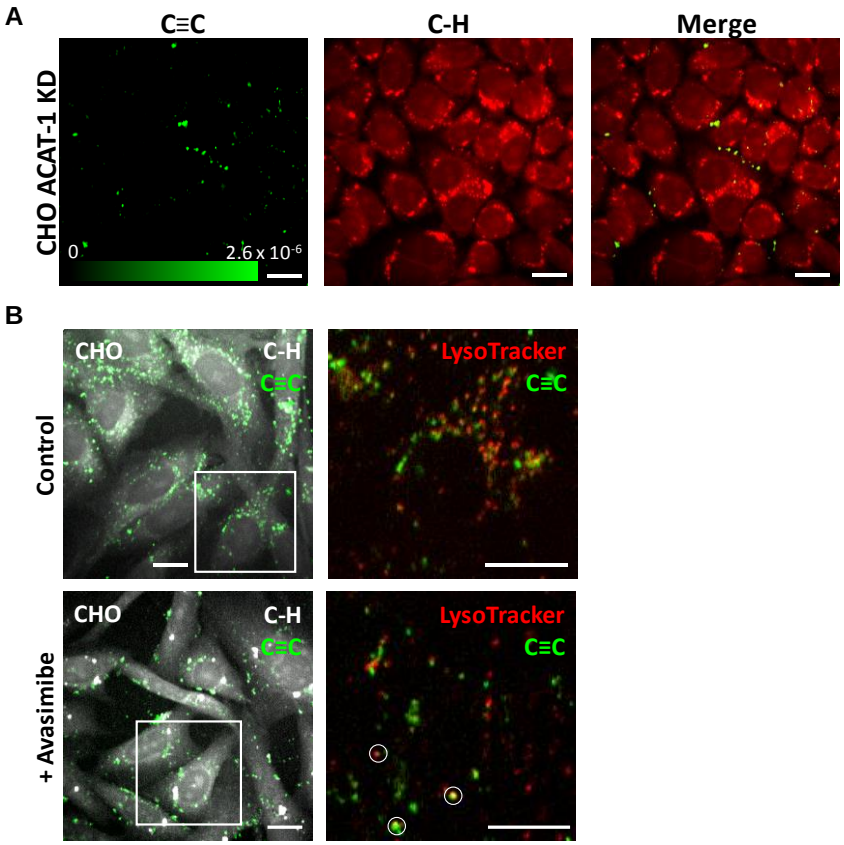

Figure 3.9 ACAT inhibition blocks PhDY-CHOL storage into LDs.
(A) SRS images of ACAT-1 knocked down CHO cells. Intensity bar shows the ΔI/I value of the SRS image. Image acquisition speed: 10 µs per pixel for 400 × 400 pixels. Scale bar: 10 µm. (B) SRS images of PhDY-Chol and TPEF images of LysoTracker-stained organelles in CHO cells and ACAT inhibited CHO cells by avasimibe treatment. Circles indicate PhDY-Chol overlapped with LysoTracker-stained organelles. Image acquisition speed: 10 µs per pixel for 400 × 400 pixels. Scale bar: 10 µm.

3.3.5 Lysosomal accumulation and relocation of PhDY-Chol to LDs in NP-C disease model

Next, we explored the potential of PhDY-Chol for studying cholesterol transport in NP-C disease, a disorder featured by abnormal cholesterol accumulation in late endosome/lysosome caused by mutation in NPC1 or 2 gene [250]. M12 cells, mutant CHO cells that contain a deletion of the NPC1 locus, were established as a cellular model of the NP-C disease [247]. By combining SRL imaging of PhDY with TPEF imaging of filipin, we observed that, unlike wildtype CHO cells, the PhDY-Chol-rich structures were stained by filipin, indicating that these PhDY-Chol molecules are located in lysosomes. (**Figure 4.10A**, **Figure 4.11A** and **B**). Moreover, we observed some filipin labeled structures that do not contain PhDY-Chol. This result is reasonable given that filipin has been shown to label other lipid molecules, such as glycosphingolipids [239]. As additional evidence, we incubated M12 cells with PhDY-Chol and stained the cells with LysoTracker. It was found that all PhDY-Chol-rich areas were localized in LysoTracker-stained organelles (**Figure 4.11C**). Collectively, these results showed that PhDY-Chol selectively represents the lysosomal storage of cholesterol in the NP-C disease model.

We then treated the PhDY-Chol-labeled M12 cells with a cholesterol-mobilizing drug, HPβCD [251]. This drug is known to mediate lysosomal escape of cholesterol, and promote storage of excess cholesterol into LDs [252]. After treating with HPβCD, the amount of PhDY-Chol in M12 cells decreased by half (**Figure 4.10B** and **C**). Interestingly, we observed that some PhDY-Chol-rich areas were not labeled by filipin after HPβCD treatment (arrow heads in **Figure 4.10B**). These areas likely represent PhDY-CE stored in LDs. To confirm this possibility, we stained the cells with BODIPY for localization of LDs. The result clearly showed that PhDY-Chol has moved into LDs after HPβCD treatment, and the number of PhDY-rich LDs increased significantly (**Figure 4.10D** and **E**). Together, these data indicate that PhDY-Chol can be used as a reliable cholesterol analog to study cholesterol mobilization inside living cells.

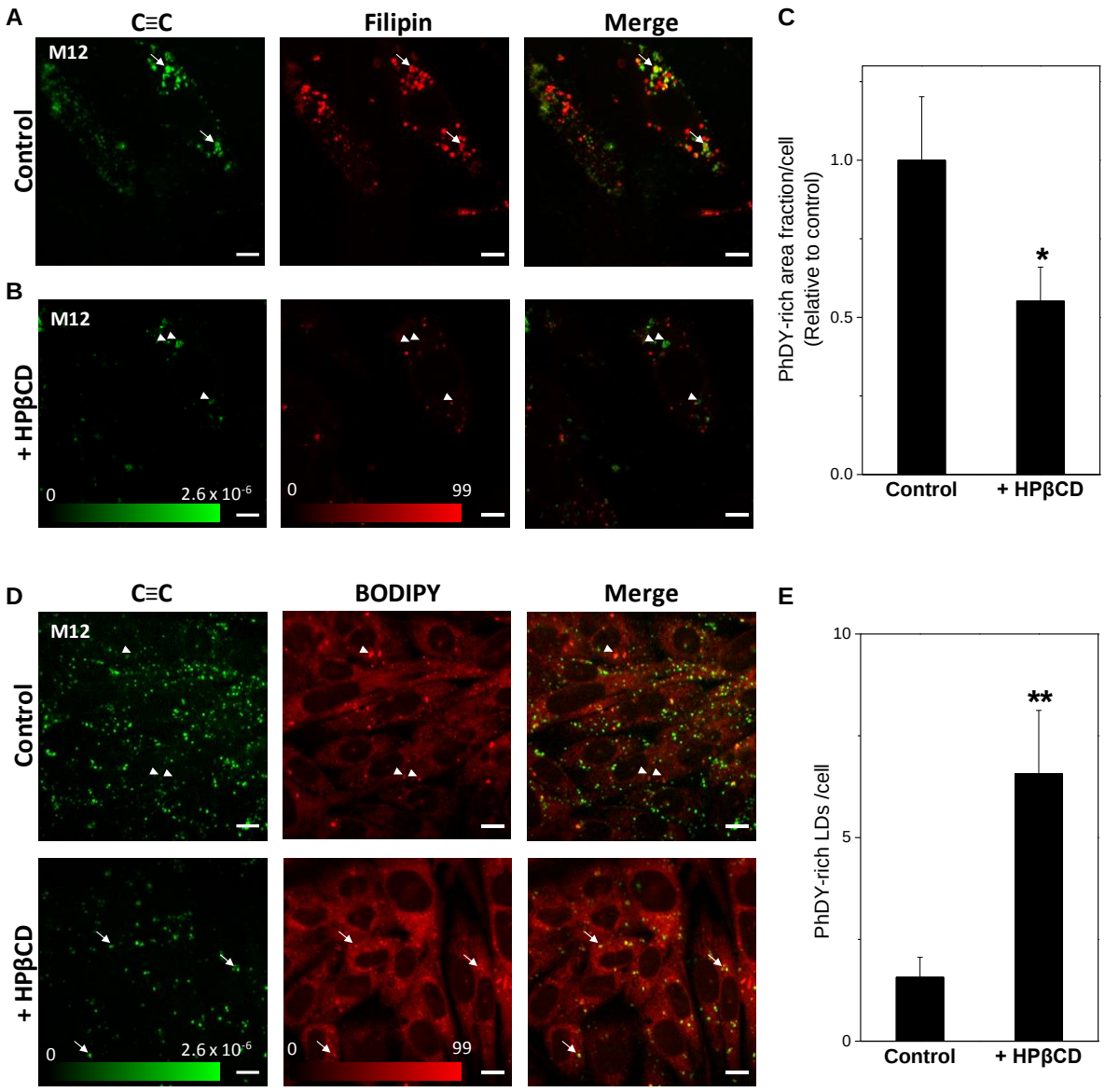

Figure 3.10 Restored cholesterol transport in M12 cells treated with HPβCD. TPEF images of filipin and SRS images of PhDY-Chol in (A) PhDY-Chol-loaded M12 cells, and (B) the same cells treated with HPβCD (500 μM) for 30 h. Arrows indicate PhDY-rich area labeled by filipin before treatment (non-esterified PhDY-Chol), and arrow heads indicate PhDY-rich area not labeled by filipin after treatment (esterified PhDY-Chol). (C) Quantification of PhDY-rich area in the cells before and after HPβCD treatment (n = 7). (D) TPEF images of BODIPY and SRS images of PhDY-Chol in M12 cells treated with or without HPβCD (500 μM) for 30 h. Arrow heads indicate LDs without PhDY-Chol before treatment, and arrows indicate LDs with PhDY-Chol after treatment. (E) Quantification of PhDY-rich LDs in the cells before and after HPβCD treatment (n = 7). Green intensity bar shows the ΔI/I value of the SRS image; red intensity bar represents the relative intensity of fluorescence. Image acquisition speed: 100 μs per pixel for 400 × 400 pixels. Scale bar: 10 μm. Error bars represent SD. *: $p < 0.05$, ** : $p < 0.005$.

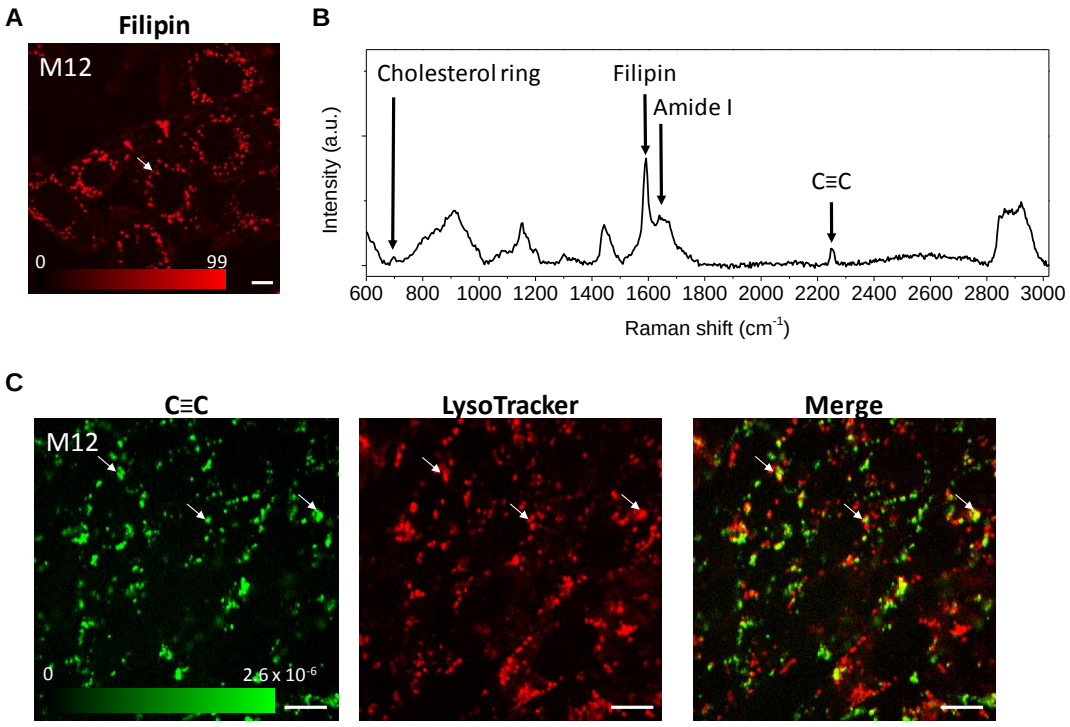

Figure 3.11 PhDY-Chol reflects lysosomal cholesterol accumulation in M12 cells. (A) TPEF image of filipin-labeled M12 cells. Arrow indicates the point used for Raman spectral analysis. Red intensity bar represents the relative intensity of fluorescence. (B) Raman spectrum of the filipin-labeled organelle acquired on the same TPEF microscope. The bands for cholesterol ring, filipin, protein (amide I), and C≡C vibrational mode are indicated by black arrows. Spectrum acquisition time: 30 s. (C) SRS image of PhDY-Chol and TPEF image of LysoTracker-stained organelles in M12 cells. All PhDY-CHOL was found inside lysosomes. Arrows representatively indicate that PhDY-Chol is accumulated in lysosomes. Intensity bar shows the ΔI/I value of the image. Image acquisition speed: 10 µs per pixel for 400 × 400 pixels. Scale bar: 10 µm.

3.3.6 Cholesterol uptake and storage in intestinal cells in *C. elegans* visualized by PhDY-Chol

Finally, to demonstrate the capability of monitoring cholesterol uptake and distribution *in vivo*, we used *C. elegans* as an animal model to study cholesterol uptake and storage. We fed N2 wildtype *C. elegans* with PhDY-Chol-labeled *E. coli* and imaged PhDY-Chol storage in the worms using our SRL microscope at speed of 40 µs per pixel. PhDY-Chol was found most abundantly in the intestinal cells inside the wildtype worms (**Figure 4.12A**). To confirm the uptake of PhDY-Chol by intestinal cells, we fed ChUP-1 mutant *C. elegans*, in which dietary cholesterol uptake is inhibited by ChUP-1 deletion [253], with PhDY-Chol. We did not observe PhDY-Chol inside this

strain (**Figure 4.12B**), which indicates that the PhDY tag did not affect the cholesterol uptake process, which is mediated by ChUP-1.

Then, we tuned the laser to be resonant with C-H vibration for lipid-rich LDs. Unlike CHO cells, the PhDY-Chol-rich compartments were found to be distinguished from LDs in wildtype worms (**Figure 4.12A**). To explore the nature of PhDY-Chol-rich compartments found in our study, we used hjIs9 worms that contain GFP targeted to lysosome-related organelles (LROs) in intestinal cells [254]. Dual-modality SRS and TPEF imaging showed that PhDY-Chol is stored in the LROs (**Figure 4.13**). We further confirmed the cholesterol storage in intestinal LROs by combining TPEF imaging of GFP targeted LROs and Raman spectral analysis of hjIs9 worms fed with normal cholesterol (**Figure 4.14**). Raman spectrum of LROs showed peaks for sterol C=C bond at 1667 cm^{-1} and Fermi resonance between asymmetrical CH_2 vibrational modes at 2875 cm^{-1}, indicating the presence of cholesterol in this organelle (**Figure 4.14B**). Collectively, these results suggest that, unlike mammalian CHO cells, *C. elegans* stores cholesterol in LROs, but not in LDs in the intestine.

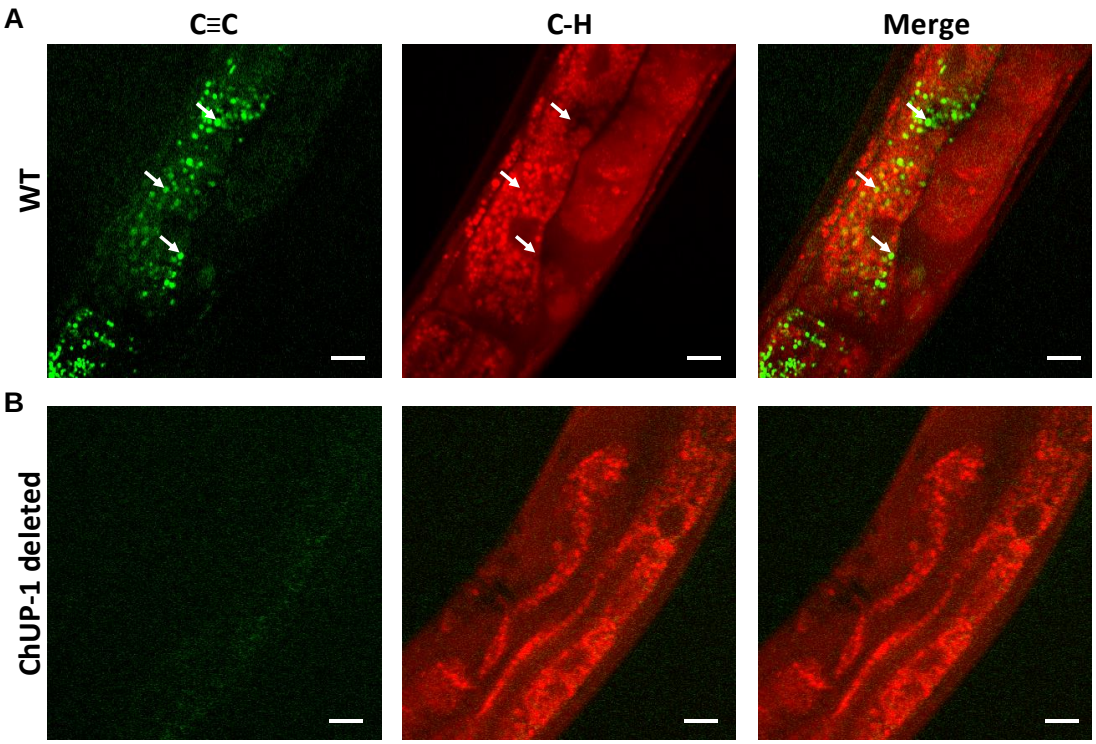

Figure 3.12 SRS imaging of PhDY-Chol visualizes cholesterol uptake in living *C. elegans*.
SRS images of living (A) wildtype and (B) ChUP-1 deleted *C. elegans* fed with PhDY-Chol (500 μM) for 3 days. Arrows indicate PhDY-rich particles in the intestine. Image acquisition speed: 40 μs per pixel for 400 × 400 pixels. Scale bar: 10 μm.

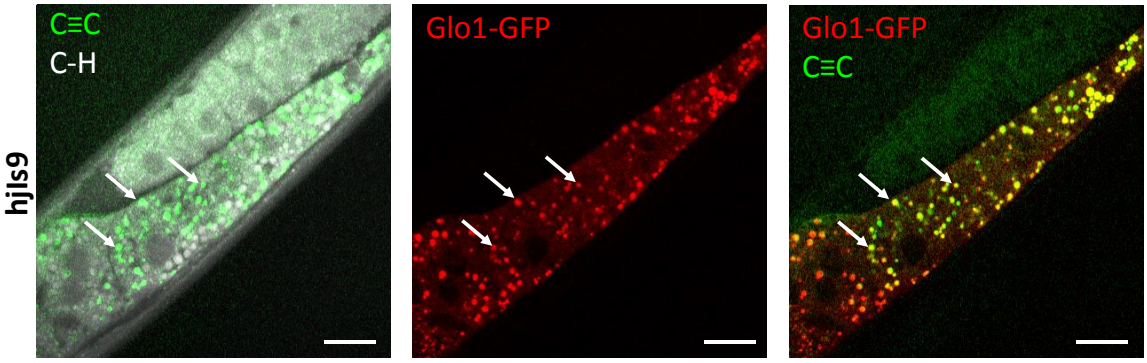

Figure 3.13 SRS imaging of PhDY-Chol visualizes compartments of cholesterol storage in live *C. elegans*.
TPEF and SRS images of live hjIs9 worm fed with PhDY-Chol (500 μM) for 3 days. Arrows indicate the PhDY-rich particles in LROs. Image acquisition speed: 40 μs per pixel for 400 × 400 pixels. Scale bar: 10 μm.

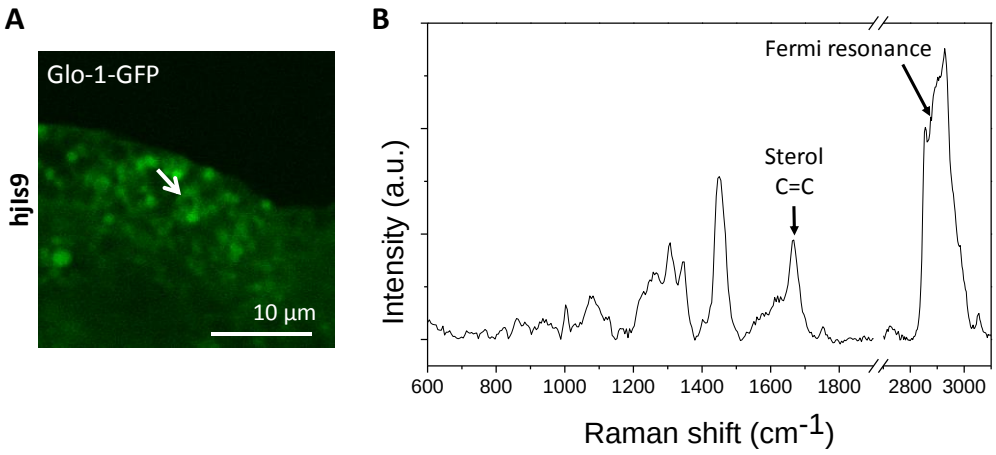

Figure 3.14 TPEF imaging and Raman spectral analysis to confirm cholesterol storage in LROs. (A) TPEF image of hjIs9 worm, which contains GFP targeted to LROs in intestinal cells. Arrow indicates the point used for Raman spectral analysis. (B) Raman spectrum of GFP surrounded LROs acquired on the same TPEF microscope. The bands for sterol C=C, and Fermi resonance between asymmetrical CH_2 vibrational modes are indicated by black arrow. Spectrum acquisition time: 10 s.

3.4 Discussion

In this study, we have developed a series of tagged cholesterols based on quantum chemistry calculations and chemical synthesis. By using PhDY to replace the aliphatic chain in cholesterol, we produced a cholesterol analog, PhDY-Chol, with a Raman signal that is two orders of magnitude stronger than the C=O group. By SRS imaging of living CHO cells, PhDY-Chol was found to be incorporated into the membrane, and converted to PhDY-CE for storage in LDs. With this cholesterol analog, we experimentally validated that after ACAT inhibition, cholesterol partly accumulates in lysosomes. In living NPC1-deleted CHO cells, PhDY-Chol selectively represented lysosomal accumulation of cholesterol in untreated cells, and esterification and relocation to LDs after HPβCD treatment.

Essential parameters of a valid Raman tag include its amplitude of Raman scattering cross section, cytotoxicity, and biocompatibility. Although the C-D bond can be used to replace C-H bonds without changing the structures of the molecules, it gives relatively weak Raman intensities. Raman signal from alkyne bond is stronger than that from C-D bond by one order of magnitude [185], and detection at hundreds of micromolar of alkyne-containing molecules by SRS microscopy was reported [186, 187]. It should be noted that terminal alkyne is known to react with

the cysteine residues in proteins [255], which might induce cytotoxicity at micromolar concentrations. In our study, through rational design and synthesis of a PhDY tag, we increased the Raman scattering cross section by 15 times compared to the alkyne group, and 88 times compared to the endogenous C=O group. This enhancement is a result of conjugation of π-electrons among the two C≡C bonds and the phenyl group. As a result, we have been able to detect ~30 μM of PhDY-Chol molecules (~1,800 molecules at excitation volume), and demonstrated SRS imaging of PhDY-Chol in single membrane at speed of 6 μs per pixel, and a real-time movie of PhDY-Chol containing LDs. Importantly, this design also shielded the activity of terminal alkyne and significantly reduced cytotoxicity. Moreover, PhDY-Chol structurally mimics cholesterol, using the same physiological process for cholesterol transport and metabolism inside cells. Cell membrane morphology did not alter when PhDY-Chol was supplemented at high concentrations when compared to the cells supplemented with the same concentrations of cholesterol (**Figure 4.5**). Moreover, the fluorescent property of pyrenedecanoic acid, a membrane fluidity indicator [256], did not change after CHO cells were treated with 50 μM of PhDY-Chol or 50 μM of cholesterol for 16 h. These evaluations suggest that the membrane property of the cells was not significantly affected by addition of PhDY-Chol or cholesterol under our experimental conditions. We note that using the same strategy, other Raman tag molecules can be designed for sensitive and biocompatible probing of biomolecules in living cells.

The potential value of a Raman tag is also related to the detection sensitivity of SRS microscopy. One limitation comes from the cross-phase modulation, which produces a background that reduces the contrast for the tag molecules. Although broadband femtosecond lasers provide high peak intensity to enhance the SRS signal [141], they also increase the amplitude of the cross-phase modulation. As shown in our study, this background can be reduced by 3 times using spectral focusing [151]. The spectral focusing approach also increases the spectral selectivity, reduces the photodamage, and provides opportunities to conduct hyperspectral SRS imaging [149].

In this study, we compared BODIPY-cholesterol [120] and PhDY-Chol. Our results show that PhDY-Chol is stored in LDs via esterification which can be blocked by ACAT inhibition. In contrast, BODIPY-cholesterol labels LDs even after ACAT inhibition. This result may be due to the strong hydrophobic interaction of BODIPY with LDs, and is consistent with previous studies

showing that BODIPY-cholesterol is hardly esterified by ACAT inside the cells [120]. These results demonstrate that PhDY-Chol, but not BODIPY-cholesterol, reflects the intracellular behavior of free cholesterol. We also showed that PhDY-Chol reflects the location of the cholesterol in real-time, unlike filipin staining, which requires fixation. Lastly, SRS microscopy utilizes chemical-bond vibrational signals for visualization. Thus, unlike fluorophores, the PhDY tag does not undergo photo-bleaching (**Figure 4.12**), in contrast to BODIPY-cholesterol and DHE [112] which is known to have a rapid photo-bleaching rate. Combining these unique properties, PhDY-Chol allows quantitative imaging of intracellular cholesterol, and repetitive observation of the same sample before and after treatment.

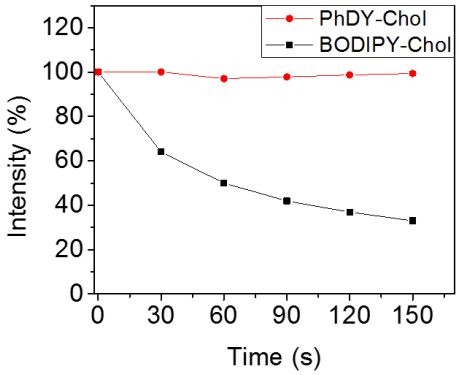

Figure 3.15 The photostability of PhDY-Chol and the photo-bleaching of BODIPY-Chol. The SRS images of 50 mM PhDY-Chol solution and TPEF images of 50 mM BODIPY-Chol solution were acquired continuously for 150 s (one acquisition every 30 s). No significant change of the SRS signal was observed for PhDY-Chol, and a rapid photo-bleaching was observed for BODIPY-Chol.

Our work opens new opportunities for mechanistic study of the NP-C disease, a fatal neurodegenerative disease that shows extensive lysosomal accumulation of cholesterol. Early detection methods and treatment strategies of this disease are still under development [72]. The involvement of lysosomal cholesterol accumulation to the neurodegeneration is still unclear [73]. Our *in vitro* study shows the cholesterol trafficking and metabolism in a cellular model. This can be extended to *in vivo* studies using suitable mouse models to understand the progression of the disease and impact of potential therapeutic strategies, especially in central nervous system.

C. elegans is an important model for genetic and chemical screening in many diseases [257]. It has been proposed that the intracellular sterol trafficking pathway might be conserved in nematodes

[258], making it a good model for exploring the genetics of fat storage and lipid metabolism [259]. However, lipid storage in *C. elegans* has been a debate because of limitations and controversies of the visualization tool for lipids [176, 177], especially cholesterol. Filipin labeling causes sterol extraction and some tissues were not accessible with staining [119, 260]. Imaging fluorescent cholesterol in *C. elegans* is a challenge due to strong and spectrally overlapping autofluorescence from the worm [118]. Using label-free CARS microscopy, fat storage compartments in *C. elegans* were studied [167, 261]. However, single color CARS microscopy based on the signal from C-H stretch vibrations cannot tell the compositions of the LDs, and so far it is not clear where the cholesterol is stored inside the worms. By combination of chemical synthesis of PhDY-Chol and real-time SRS imaging, we found evidences suggesting the cholesterol storage in LROs. Label-free Raman spectral analysis was performed to validate the finding. Sterol uptake and transport in worms are still poorly understood [253], and SRS imaging of PhDY-Chol opens an avenue to directly assess cholesterol uptake and transport for genome-wide RNA interference screening of cholesterol transport and storage genes in this animal model. Finally, our work also opens new opportunities to study cholesterol trafficking and metabolism in other animal models such as zebrafish and mice.

4. OUTLOOK

4.1 Cholesterol metabolism in cancer

Our study identified CE as a metabolic marker of metastatic PCa, and demonstrated therapeutic potential of targeting cholesterol esterification to suppress development and growth of metastatic cancer. Our next step is to validate the correlation between CE accumulation in PCa patient tissues and the clinical outcomes. At the same time, we will compare the therapeutic efficacy of targeting cholesterol esterification with the current treatment approaches, e.g. docetaxel or abiraterone, in preclinical animal models of PCa. It is our expectation that we will provide strong evidence to support the potential of using cholesterol esterification as a therapeutic target for metastatic PCa. Notably, avasimibe is a FDA-approved drug for atherosclerosis, which failed due to the lack of effectiveness. Our study re-purposed the existing drug to treat metastatic PCa, which potentially saves a lot of cost and risks of drug development. Lastly, the mechanistic study shown in Chapter 2 will contribute to a deeper understanding of altered cholesterol homeostasis in prostate cancer, and provide a link between abnormal lipid metabolism and oncogenic pathway during cancer metastasis. Together, these results will serve as a foundation for moving into clinical studies.

4.2 Visualizing cholesterol dynamics

We have developed PhDY-Chol and demonstrated its application in studying cholesterol trafficking in the NP-C disease model and in *C. elegans*. This study opens new opportunities in several directions. First, visualizing cholesterol dynamics in living cells and organisms would enable the discovery of the mechanism of cholesterol trafficking and regulation of cholesterol metabolism. There are still many processes in intracellular cholesterol transport that are unknown due to difficulties in monitoring the fate of cholesterol in cells. We expect that SRS imaging of PhDY-Chol will serve as a novel platform to study the physiological functions of various cholesterol-binding proteins and to discover novel cholesterol transport mechanisms. New regulators of cholesterol homeostasis and trafficking can be further identified by combining with genome-wide RNA interference screening. Second, PhDY-Chol can be applied to study the functional roles abnormal cholesterol transport and metabolism in other diseases, such as atherosclerosis and Tangier disease, to facilitate the development of new therapeutic approaches.

Third, high-throughput screening of cellular response to drugs for treating cholesterol-related diseases, such as NP-C disease or cancer, would allow discovery of new therapeutic targets and mechanisms. SRS imaging of PhDY-Chol allows real-time assessment of cholesterol trafficking and metabolism, which can provide faster readouts after the treatment. Lastly, by incorporating PhDY tag, dynamics of other essential sterols, such as oxysterols, can be visualized in living cells. In summary, future studies on cholesterol trafficking and metabolism using SRS imaging of PhDY-Chol will contribute to more complete understanding of cholesterol dynamics, which is an indispensable lipid in mammalian cells.

4.3 Imaging small molecules using Raman tag

Using the strategy described in Chapter 3, other Raman tag molecules can be designed for imaging small molecules in living cells. Most of fluorescent labeling introduce bulky fluorophores or fluorescent proteins to molecules of interest, which sometimes interfere with its functions. Designing and incorporation of a smaller labeling group, such as Raman tag, is especially advantageous to labeling of small molecules for minimal perturbation. We expect that this technique would enable characterization of the distribution of small metabolites or proteins with its physiological functions. It would be also important to develop novel Raman tags that can be used to measure *in vivo* activities of target molecules such as enzymes or receptors. In summary, Raman spectroscopic imaging is a valuable tool in studying chemistry *in situ* inside living cells and organisms.

REFERENCES

[1] Yeagle, P. L. 1985. Cholesterol and the cell membrane. *Biochim. Biophys. Acta* **822**: 267-287.

[2] Lingwood, D., Simons, K. 2010. Lipid rafts as a membrane-organizing principle. *Science* **327**: 46-50.

[3] Miller, W. L., Auchus, R. J. 2011. The molecular biology, biochemistry, and physiology of human steroidogenesis and its disorders. *Endocr. Rev.* **32**: 81-151.

[4] Wang, P. Y., Weng, J., Anderson, R. G. 2005. OSBP is a cholesterol-regulated scaffolding protein in control of ERK 1/2 activation. *Science* **307**: 1472-1476.

[5] Sheng, R., Chen, Y., Yung Gee, H., Stec, E., Melowic, H. R., Blatner, N. R., et al. 2012. Cholesterol modulates cell signaling and protein networking by specifically interacting with PDZ domain-containing scaffold proteins. *Nat. Commun.* **3**: 1249.

[6] Mann, R. K., Beachy, P. A. 2000. Cholesterol modification of proteins. *Biochim. Biophys. Acta* **1529**: 188-202.

[7] Mann, R. K., Beachy, P. A. 2004. Novel lipid modifications of secreted protein signals. *Annu. Rev. Biochem.* **73**: 891-923.

[8] Goldstein, J. L., DeBose-Boyd, R. A., Brown, M. S. 2006. Protein sensors for membrane sterols. *Cell* **124**: 35-46.

[9] Chang, T. Y., Chang, C. C., Ohgami, N., Yamauchi, Y. 2006. Cholesterol sensing, trafficking, and esterification. *Annu. Rev. Cell Dev. Biol.* **22**: 129-157.

[10] Ikonen, E. 2008. Cellular cholesterol trafficking and compartmentalization. *Nat. Rev. Mol. Cell Biol.* **9**: 125-138.

[11] Bloch, K. 1965. The biological synthesis of cholesterol. *Science* **150**: 19-28.

[12] Brown, M. S., Goldstein, J. L. 1986. A receptor-mediated pathway for cholesterol homeostasis. *Science* **232**: 34-47.

[13] Phillips, M. C. 2014. Molecular mechanisms of cellular cholesterol efflux. *J. Biol. Chem.* **289**: 24020-24029.

[14] Lusa, S., Heino, S., Ikonen, E. 2003. Differential mobilization of newly synthesized cholesterol and biosynthetic sterol precursors from cells. *J. Biol. Chem.* **278**: 19844-19851.

[15] Baumann, N. A., Sullivan, D. P., Ohvo-Rekila, H., Simonot, C., Pottekat, A., Klaassen, Z., et al. 2005. Transport of newly synthesized sterol to the sterol-enriched plasma membrane occurs via nonvesicular equilibration. *Biochemistry* **44**: 5816-5826.

[16] Heino, S., Lusa, S., Somerharju, P., Ehnholm, C., Olkkonen, V. M., Ikonen, E. 2000. Dissecting the role of the golgi complex and lipid rafts in biosynthetic transport of cholesterol to the cell surface. *Proc. Natl. Acad. Sci. U. S. A.* **97**: 8375-8380.

[17] Maxfield, F. R., Mondal, M. 2006. Sterol and lipid trafficking in mammalian cells. *Biochem. Soc. Trans.* **34**: 335-339.

[18] Smart, E. J., Ying, Y., Donzell, W. C., Anderson, R. G. 1996. A role for caveolin in transport of cholesterol from endoplasmic reticulum to plasma membrane. *J. Biol. Chem.* **271**: 29427-29435.

[19] Matveev, S., Li, X., Everson, W., Smart, E. J. 2001. The role of caveolae and caveolin in vesicle-dependent and vesicle-independent trafficking. *Adv. Drug Deliv. Rev.* **49**: 237-250.

[20] Olkkonen, V. M. 2004. Oxysterol binding protein and its homologues: new regulatory factors involved in lipid metabolism. *Curr. Opin. Lipidol.* **15**: 321-327.

[21] Alpy, F., Tomasetto, C. 2005. Give lipids a START: the StAR-related lipid transfer (START) domain in mammals. *J. Cell Sci.* **118**: 2791-2801.
[22] Sugii, S., Reid, P. C., Ohgami, N., Du, H., Chang, T. Y. 2003. Distinct endosomal compartments in early trafficking of low density lipoprotein-derived cholesterol. *J. Biol. Chem.* **278**: 27180-27189.
[23] Cruz, J. C., Sugii, S., Yu, C., Chang, T. Y. 2000. Role of Niemann-Pick type C1 protein in intracellular trafficking of low density lipoprotein-derived cholesterol. *J. Biol. Chem.* **275**: 4013-4021.
[24] Resh, M. D. 2013. Covalent lipid modifications of proteins. *Curr. Biol.* **23**: R431-435.
[25] Pfeffer, S., Aivazian, D. 2004. Targeting Rab GTPases to distinct membrane compartments. *Nat. Rev. Mol. Cell Biol.* **5**: 886-896.
[26] Stocco, D. M. 2001. StAR protein and the regulation of steroid hormone biosynthesis. *Annu. Rev. Physiol.* **63**: 193-213.
[27] Bose, H. S., Lingappa, V. R., Miller, W. L. 2002. Rapid regulation of steroidogenesis by mitochondrial protein import. *Nature* **417**: 87-91.
[28] Flis, V. V., Daum, G. 2013. Lipid transport between the endoplasmic reticulum and mitochondria. *Cold Spring Harb. Perspect. Biol.* **5**.
[29] Miller, W. L. 2007. Steroidogenic acute regulatory protein (StAR), a novel mitochondrial cholesterol transporter. *Biochim. Biophys. Acta* **1771**: 663-676.
[30] Stocco, D. M. 2001. Tracking the role of a star in the sky of the new millennium. *Mol. Endocrinol.* **15**: 1245-1254.
[31] Li, H., Yao, Z., Degenhardt, B., Teper, G., Papadopoulos, V. 2001. Cholesterol binding at the cholesterol recognition/ interaction amino acid consensus (CRAC) of the peripheral-type benzodiazepine receptor and inhibition of steroidogenesis by an HIV TAT-CRAC peptide. *Proc. Natl. Acad. Sci. U. S. A.* **98**: 1267-1272.
[32] Tabas, I. 2002. Consequences of cellular cholesterol accumulation: basic concepts and physiological implications. *J. Clin. Invest.* **110**: 905-911.
[33] Simons, K., Ikonen, E. 2000. How cells handle cholesterol. *Science* **290**: 1721-1726.
[34] Yeagle, P. L. 1991. Modulation of membrane function by cholesterol. *Biochimie* **73**: 1303-1310.
[35] Kellner-Weibel, G., Yancey, P. G., Jerome, W. G., Walser, T., Mason, R. P., Phillips, M. C., Rothblat, G. H. 1999. Crystallization of free cholesterol in model macrophage foam cells. *Arterioscler. Thromb. Vasc. Biol.* **19**: 1891-1898.
[36] Brown, A. J., Jessup, W. 1999. Oxysterols and atherosclerosis. *Atherosclerosis* **142**: 1-28.
[37] Bjorkhem, I. 2002. Do oxysterols control cholesterol homeostasis? *J. Clin. Invest.* **110**: 725-730.
[38] Yao, P. M., Tabas, I. 2000. Free cholesterol loading of macrophages induces apoptosis involving the fas pathway. *J. Biol. Chem.* **275**: 23807-23813.
[39] Yao, P. M., Tabas, I. 2001. Free cholesterol loading of macrophages is associated with widespread mitochondrial dysfunction and activation of the mitochondrial apoptosis pathway. *J. Biol. Chem.* **276**: 42468-42476.
[40] Sozen, E., Ozer, N. K. 2017. Impact of high cholesterol and endoplasmic reticulum stress on metabolic diseases: An updated mini-review. *Redox Biol.* **12**: 456-461.
[41] Brown, M. S., Goldstein, J. L. 2009. Cholesterol feedback: from Schoenheimer's bottle to Scap's MELADL. *J. Lipid Res.* **50**: S15-S27.

[42] Hua, X., Nohturfft, A., Goldstein, J. L., Brown, M. S. 1996. Sterol resistance in CHO cells traced to point mutation in SREBP cleavage-activating protein. *Cell* **87**: 415-426.

[43] Yang, T., Goldstein, J. L., Brown, M. S. 2000. Overexpression of membrane domain of SCAP prevents sterols from inhibiting SCAP.SREBP exit from endoplasmic reticulum. *J. Biol. Chem.* **275**: 29881-29886.

[44] Sever, N., Yang, T., Brown, M. S., Goldstein, J. L., DeBose-Boyd, R. A. 2003. Accelerated degradation of HMG CoA reductase mediated by binding of insig-1 to its sterol-sensing domain. *Mol. Cell* **11**: 25-33.

[45] Gil, G., Faust, J. R., Chin, D. J., Goldstein, J. L., Brown, M. S. 1985. Membrane-bound domain of HMG CoA reductase is required for sterol-enhanced degradation of the enzyme. *Cell* **41**: 249-258.

[46] Brown, M. S., Goldstein, J. L. 1997. The SREBP pathway: regulation of cholesterol metabolism by proteolysis of a membrane-bound transcription factor. *Cell* **89**: 331-340.

[47] Horton, J. D., Goldstein, J. L., Brown, M. S. 2002. SREBPs: activators of the complete program of cholesterol and fatty acid synthesis in the liver. *J. Clin. Invest.* **109**: 1125-1131.

[48] Brown, A. J., Sun, L., Feramisco, J. D., Brown, M. S., Goldstein, J. L. 2002. Cholesterol addition to ER membranes alters conformation of SCAP, the SREBP escort protein that regulates cholesterol metabolism. *Mol. Cell* **10**: 237-245.

[49] Amemiya-Kudo, M., Shimano, H., Hasty, A. H., Yahagi, N., Yoshikawa, T., Matsuzaka, T., et al. 2002. Transcriptional activities of nuclear SREBP-1a, -1c, and -2 to different target promoters of lipogenic and cholesterogenic genes. *J. Lipid Res.* **43**: 1220-1235.

[50] Horton, J. D., Shah, N. A., Warrington, J. A., Anderson, N. N., Park, S. W., Brown, M. S., Goldstein, J. L. 2003. Combined analysis of oligonucleotide microarray data from transgenic and knockout mice identifies direct SREBP target genes. *Proc. Natl. Acad. Sci. U. S. A.* **100**: 12027-12032.

[51] Tabor, D. E., Kim, J. B., Spiegelman, B. M., Edwards, P. A. 1999. Identification of conserved cis-elements and transcription factors required for sterol-regulated transcription of stearoyl-CoA desaturase 1 and 2. *J. Biol. Chem.* **274**: 20603-20610.

[52] Paton, C. M., Ntambi, J. M. 2009. Biochemical and physiological function of stearoyl-CoA desaturase. *Am. J. Physiol. Endocrinol. Metab.* **297**: E28-37.

[53] Eberle, D., Hegarty, B., Bossard, P., Ferre, P., Foufelle, F. 2004. SREBP transcription factors: master regulators of lipid homeostasis. *Biochimie* **86**: 839-848.

[54] Zhao, C., Dahlman-Wright, K. 2010. Liver X receptor in cholesterol metabolism. *J. Endocrinol.* **204**: 233-240.

[55] Hu, X., Li, S., Wu, J., Xia, C., Lala, D. S. 2003. Liver X receptors interact with corepressors to regulate gene expression. *Mol. Endocrinol.* **17**: 1019-1026.

[56] Janowski, B. A., Willy, P. J., Devi, T. R., Falck, J. R., Mangelsdorf, D. J. 1996. An oxysterol signalling pathway mediated by the nuclear receptor LXR alpha. *Nature* **383**: 728-731.

[57] Glass, C. K., Rosenfeld, M. G. 2000. The coregulator exchange in transcriptional functions of nuclear receptors. *Genes Dev.* **14**: 121-141.

[58] Joseph, S. B., Laffitte, B. A., Patel, P. H., Watson, M. A., Matsukuma, K. E., Walczak, R., et al. 2002. Direct and indirect mechanisms for regulation of fatty acid synthase gene expression by liver X receptors. *J. Biol. Chem.* **277**: 11019-11025.

[59] Repa, J. J., Liang, G., Ou, J., Bashmakov, Y., Lobaccaro, J. M., Shimomura, I., et al. 2000. Regulation of mouse sterol regulatory element-binding protein-1c gene (SREBP-1c) by oxysterol receptors, LXRalpha and LXRbeta. *Genes Dev.* **14**: 2819-2830.

[60] Tall, A. R., Costet, P., Wang, N. 2002. Regulation and mechanisms of macrophage cholesterol efflux. *J. Clin. Invest.* **110**: 899-904.

[61] Zelcer, N., Hong, C., Boyadjian, R., Tontonoz, P. 2009. LXR regulates cholesterol uptake through Idol-dependent ubiquitination of the LDL receptor. *Science* **325**: 100-104.

[62] Farese, R. V., Jr., Walther, T. C. 2009. Lipid droplets finally get a little R-E-S-P-E-C-T. *Cell* **139**: 855-860.

[63] Chang, T. Y., Li, B. L., Chang, C. C. Y., Urano, Y. 2009. Acyl-coenzyme A:cholesterol acyltransferases. *Am. J. Physiol. Endocrinol. Metab.* **297**: E1-9.

[64] Zhang, Y., Yu, C., Liu, J., Spencer, T. A., Chang, C. C., Chang, T. Y. 2003. Cholesterol is superior to 7-ketocholesterol or 7 alpha-hydroxycholesterol as an allosteric activator for acyl-coenzyme A:cholesterol acyltransferase 1. *J. Biol. Chem.* **278**: 11642-11647.

[65] Liu, J., Chang, C., Westover, E., Covey, D., Chang, T. Y. 2005. Investigating the allosterism of acyl-CoA:cholesterol acyltransferase (ACAT) by using various sterols: in vitro and intact cell studies. *Biochem. J.* **391**: 389-397.

[66] Platt, F. M., Wassif, C., Colaco, A., Dardis, A., Lloyd-Evans, E., Bembi, B., Porter, F. D. 2014. Disorders of cholesterol metabolism and their unanticipated convergent mechanisms of disease. *Annu. Rev. Genomics Hum. Genet.* **15**: 173-194.

[67] Kuzu, O. F., Noory, M. A., Robertson, G. P. 2016. The Role of Cholesterol in Cancer. *Cancer Res.* **76**: 2063.

[68] Glass, C. K., Witztum, J. L. 2001. Atherosclerosis. the road ahead. *Cell* **104**: 503-516.

[69] Ross, R. 1995. Cell biology of atherosclerosis. *Annu. Rev. Physiol.* **57**: 791-804.

[70] Katz, S. S., Shipley, G. G., Small, D. M. 1976. Physical chemistry of the lipids of human atherosclerotic lesions. Demonstration of a lesion intermediate between fatty streaks and advanced plaques. *J. Clin. Invest.* **58**: 200-211.

[71] Irons, M., Elias, E. R., Salen, G., Tint, G. S., Batta, A. K. 1993. Defective cholesterol biosynthesis in Smith-Lemli-Opitz syndrome. *Lancet* **341**: 1414.

[72] Patterson, M. C. 2003. A riddle wrapped in a mystery: understanding Niemann-Pick disease, type C. *Neurologist* **9**: 301-310.

[73] Pfrieger, F. W. 2003. Cholesterol homeostasis and function in neurons of the central nervous system. *Cell. Mol. Life Sci.* **60**: 1158-1171.

[74] Puntoni, M., Sbrana, F., Bigazzi, F., Sampietro, T. 2012. Tangier disease: epidemiology, pathophysiology, and management. *Am. J. Cardiovasc. Drugs* **12**: 303-311.

[75] White, C. P. 1909. On the occurrence of crystals in tumours. *J. Pathol. Bacteriol.* **13**: 3-10.

[76] Pelton, K., Freeman, M. R., Solomon, K. R. 2012. Cholesterol and prostate cancer. *Curr. Opin. Pharmacol.* **12**: 751-759.

[77] Allott, E. H., Howard, L. E., Cooperberg, M. R., Kane, C. J., Aronson, W. J., Terris, M. K., et al. 2014. Serum lipid profile and risk of prostate cancer recurrence: Results from the SEARCH database. *Cancer Epidemiol. Biomarkers Prev.* **23**: 2349-2356.

[78] Brown, A. J. 2007. Cholesterol, statins and cancer. *Clin. Exp. Pharmacol. Physiol.* **34**: 135-141.

[79] Strohmaier, S., Edlinger, M., Manjer, J., Stocks, T., Bjorge, T., Borena, W., et al. 2013. Total serum cholesterol and cancer incidence in the Metabolic syndrome and Cancer Project (Me-Can). *PLoS One* **8**: e54242.

[80] Cholesterol Treatment Trialists, C. 2010. Efficacy and safety of more intensive lowering of LDL cholesterol: a meta-analysis of data from 170 000 participants in 26 randomised trials. *Lancet* **376**: 1670-1681.

[81] Ravnskov, U., McCully, K. S., Rosch, P. J. 2012. The statin-low cholesterol-cancer conundrum. *QJM* **105**: 383-388.

[82] Pedersen, T. R., Wilhelmsen, L., Faergeman, O., Strandberg, T. E., Thorgeirsson, G., Troedsson, L., et al. 2000. Follow-up study of patients randomized in the Scandinavian simvastatin survival study (4S) of cholesterol lowering. *Am. J. Cardiol.* **86**: 257-262.

[83] Llaverias, G., Danilo, C., Mercier, I., Daumer, K., Capozza, F., Williams, T. M., et al. 2011. Role of cholesterol in the development and progression of breast cancer. *Am. J. Pathol.* **178**: 402-412.

[84] Vassilev, B., Sihto, H., Li, S., Holtta-Vuori, M., Ilola, J., Lundin, J., et al. 2015. Elevated levels of StAR-related lipid transfer protein 3 alter cholesterol balance and adhesiveness of breast cancer cells: potential mechanisms contributing to progression of HER2-positive breast cancers. *Am. J. Pathol.* **185**: 987-1000.

[85] Weinstein, J. N., Collisson, E. A., Mills, G. B., Shaw, K. R., Ozenberger, B. A., Ellrott, K., et al. 2013. The Cancer Genome Atlas Pan-Cancer analysis project. *Nat. Genet.* **45**: 1113-1120.

[86] Porstmann, T., Santos, C. R., Griffiths, B., Cully, M., Wu, M., Leevers, S., et al. 2008. SREBP activity is regulated by mTORC1 and contributes to Akt-dependent cell growth. *Cell Metab.* **8**: 224-236.

[87] Dong, F., Mo, Z., Eid, W., Courtney, K. C., Zha, X. 2014. Akt inhibition promotes ABCA1-mediated cholesterol efflux to ApoA-I through suppressing mTORC1. *PLoS One* **9**: e113789.

[88] Yue, S., Li, J., Lee, S.-Y., Lee, H. J., Shao, T., Song, B., et al. 2014. Cholesteryl ester accumulation induced by PTEN loss and PI3K/AKT activation underlies human prostate cancer aggressiveness. *Cell Metab.* **19**: 393-406.

[89] Porstmann, T., Griffiths, B., Chung, Y. L., Delpuech, O., Griffiths, J. R., Downward, J., Schulze, A. 2005. PKB/Akt induces transcription of enzymes involved in cholesterol and fatty acid biosynthesis via activation of SREBP. *Oncogene* **24**: 6465-6481.

[90] Freed-Pastor, W. A., Mizuno, H., Zhao, X., Langerod, A., Moon, S. H., Rodriguez-Barrueco, R., et al. 2012. Mutant p53 disrupts mammary tissue architecture via the mevalonate pathway. *Cell* **148**: 244-258.

[91] Zhuang, L., Lin, J., Lu, M. L., Solomon, K. R., Freeman, M. R. 2002. Cholesterol-rich lipid rafts mediate akt-regulated survival in prostate cancer cells. *Cancer Res.* **62**: 2227-2231.

[92] Zhuang, L., Kim, J., Adam, R. M., Solomon, K. R., Freeman, M. R. 2005. Cholesterol targeting alters lipid raft composition and cell survival in prostate cancer cells and xenografts. *J. Clin. Invest.* **115**: 959-968.

[93] Freeman, M. R., Cinar, B., Kim, J., Mukhopadhyay, N. K., Di Vizio, D., Adam, R. M., Solomon, K. R. 2007. Transit of hormonal and EGF receptor-dependent signals through cholesterol-rich membranes. *Steroids* **72**: 210-217.

[94] Smith, B., Land, H. 2012. Anticancer activity of the cholesterol exporter ABCA1 gene. *Cell Rep.* **2**: 580-590.

[95] Montero, J., Morales, A., Llacuna, L., Lluis, J. M., Terrones, O., Basanez, G., et al. 2008. Mitochondrial cholesterol contributes to chemotherapy resistance in hepatocellular carcinoma. *Cancer Res.* **68**: 5246-5256.

[96] Adam, R. M., Mukhopadhyay, N. K., Kim, J., Di Vizio, D., Cinar, B., Boucher, K., et al. 2007. Cholesterol sensitivity of endogenous and myristoylated Akt. *Cancer Res.* **67**: 6238-6246.

[97] Sorrentino, G., Ruggeri, N., Specchia, V., Cordenonsi, M., Mano, M., Dupont, S., et al. 2014. Metabolic control of YAP and TAZ by the mevalonate pathway. *Nat. Cell Biol.* **16**: 357-366.

[98] Xiao, X., Tang, J. J., Peng, C., Wang, Y., Fu, L., Qiu, Z. P., et al. 2017. Cholesterol modification of smoothened is required for hedgehog signaling. *Mol. Cell* **66**: 154-162.e110.

[99] Wicking, C., McGlinn, E. 2001. The role of hedgehog signalling in tumorigenesis. *Cancer Lett.* **173**: 1-7.

[100] Fernandez, C., Martin, M., Gomez-Coronado, D., Lasuncion, M. A. 2005. Effects of distal cholesterol biosynthesis inhibitors on cell proliferation and cell cycle progression. *J. Lipid Res.* **46**: 920-929.

[101] Dong, P., Flores, J., Pelton, K., Solomon, K. R. 2010. Prohibitin is a cholesterol-sensitive regulator of cell cycle transit. *J. Cell. Biochem.* **111**: 1367-1374.

[102] Locke, J. A., Guns, E. S., Lubik, A. A., Adomat, H. H., Hendy, S. C., Wood, C. A., et al. 2008. Androgen levels increase by intratumoral de novo steroidogenesis during progression of castration-resistant prostate cancer. *Cancer Res.* **68**: 6407-6415.

[103] Leon, C. G., Locke, J. A., Adomat, H. H., Etinger, S. L., Twiddy, A. L., Neumann, R. D., et al. 2010. Alterations in cholesterol regulation contribute to the production of intratumoral androgens during progression to castration-resistant prostate cancer in a mouse xenograft model. *Prostate* **70**: 390-400.

[104] Mostaghel, E. A., Solomon, K. R., Pelton, K., Freeman, M. R., Montgomery, R. B. 2012. Impact of circulating cholesterol levels on growth and intratumoral androgen concentration of prostate tumors. *PLoS One* **7**: e30062.

[105] Clendening, J. W., Penn, L. Z. 2012. Targeting tumor cell metabolism with statins. *Oncogene* **31**: 4967-4978.

[106] Maione, F., Oliaro-Bosso, S., Meda, C., Di Nicolantonio, F., Bussolino, F., Balliano, G., et al. 2015. The cholesterol biosynthesis enzyme oxidosqualene cyclase is a new target to impair tumour angiogenesis and metastasis dissemination. *Sci. Rep.* **5**: 9054.

[107] Guillaumond, F., Bidaut, G., Ouaissi, M., Servais, S., Gouirand, V., Olivares, O., et al. 2015. Cholesterol uptake disruption, in association with chemotherapy, is a promising combined metabolic therapy for pancreatic adenocarcinoma. *Proc. Natl. Acad. Sci. U. S. A.* **112**: 2473-2478.

[108] Harisa, G. I., Alanazi, F. K. 2014. Low density lipoprotein bionanoparticles: From cholesterol transport to delivery of anti-cancer drugs. *Saudi Pharm. J.* **22**: 504-515.

[109] Li, J., Gu, D., Lee, S. S., Song, B., Bandyopadhyay, S., Chen, S., et al. 2016. Abrogating cholesterol esterification suppresses growth and metastasis of pancreatic cancer. *Oncogene* **35**: 6378-6388.

[110] Lee, S. S., Li, J., Tai, J. N., Ratliff, T. L., Park, K., Cheng, J. X. 2015. Avasimibe encapsulated in human serum albumin blocks cholesterol esterification for selective cancer treatment. *ACS Nano* **9**: 2420-2432.

[111] Kuzu, O. F., Gowda, R., Noory, M. A., Robertson, G. P. 2017. Modulating cancer cell survival by targeting intracellular cholesterol transport. *Br. J. Cancer* **117**: 513-524.

[112] Gimpl, G., Gehrig-Burger, K. 2007. Cholesterol reporter molecules. *Biosci. Rep.* **27**: 335-358.

[113] MacLachlan, J., Wotherspoon, A. T., Ansell, R. O., Brooks, C. J. 2000. Cholesterol oxidase: sources, physical properties and analytical applications. *J. Steroid Biochem. Mol. Biol.* **72**: 169-195.

[114] Butler, J. D., Blanchette-Mackie, J., Goldin, E., O'Neill, R. R., Carstea, G., Roff, C. F., et al. 1992. Progesterone blocks cholesterol translocation from lysosomes. *J. Biol. Chem.* **267**: 23797-23805.

[115] Reid, P. C., Sakashita, N., Sugii, S., Ohno-Iwashita, Y., Shimada, Y., Hickey, W. F., Chang, T. Y. 2004. A novel cholesterol stain reveals early neuronal cholesterol accumulation in the Niemann-Pick type C1 mouse brain. *J. Lipid Res.* **45**: 582-591.

[116] Sugii, S., Reid, P. C., Ohgami, N., Shimada, Y., Maue, R. A., Ninomiya, H., et al. 2003. Biotinylated theta-toxin derivative as a probe to examine intracellular cholesterol-rich domains in normal and Niemann-Pick type C1 cells. *J. Lipid Res.* **44**: 1033-1041.

[117] Mukherjee, S., Zha, X., Tabas, I., Maxfield, F. R. 1998. Cholesterol distribution in living cells: fluorescence imaging using dehydroergosterol as a fluorescent cholesterol analog. *Biophys. J.* **75**: 1915-1925.

[118] Wustner, D., Landt Larsen, A., Faergeman, N. J., Brewer, J. R., Sage, D. 2010. Selective visualization of fluorescent sterols in Caenorhabditis elegans by bleach-rate-based image segmentation. *Traffic* **11**: 440-454.

[119] Matyash, V., Geier, C., Henske, A., Mukherjee, S., Hirsh, D., Thiele, C., et al. 2001. Distribution and transport of cholesterol in Caenorhabditis elegans. *Mol. Biol. Cell* **12**: 1725-1736.

[120] Holtta-Vuori, M., Uronen, R. L., Repakova, J., Salonen, E., Vattulainen, I., Panula, P., et al. 2008. BODIPY-cholesterol: a new tool to visualize sterol trafficking in living cells and organisms. *Traffic* **9**: 1839-1849.

[121] Solanko, L. M., Honigmann, A., Midtiby, H. S., Lund, F. W., Brewer, J. R., Dekaris, V., et al. 2013. Membrane orientation and lateral diffusion of BODIPY-cholesterol as a function of probe structure. *Biophys. J.* **105**: 2082-2092.

[122] Hulce, J. J., Cognetta, A. B., Niphakis, M. J., Tully, S. E., Cravatt, B. F. 2013. Proteome-wide mapping of cholesterol-interacting proteins in mammalian cells. *Nat. Methods* **10**: 259-264.

[123] Hofmann, K., Thiele, C., Schott, H. F., Gaebler, A., Schoene, M., Kiver, Y., et al. 2014. A novel alkyne cholesterol to trace cellular cholesterol metabolism and localization. *J. Lipid Res.* **55**: 583-591.

[124] Lee, H. J., Cheng, J. X. 2017. Imaging chemistry inside living cells by stimulated Raman scattering microscopy. *Methods* **128**: 119-128.

[125] Zhang, Y., Hong, H., Cai, W. 2010. Imaging with Raman spectroscopy. *Curr. Pharm. Biotechnol.* **11**: 654-661.

[126] Georgakoudi, I., Quinn, K. P. 2012. Optical imaging using endogenous contrast to assess metabolic state. *Annu. Rev. Biomed. Eng.* **14**: 351-367.

[127] Croce, A., Bottiroli, G. 2014. Autofluorescence spectroscopy and imaging: a tool for biomedical research and diagnosis. *Eur. J. Histochem.* **58**.

[128] Walsh, A. J., Cook, R. S., Sanders, M. E., Aurisicchio, L., Ciliberto, G., Arteaga, C. L., Skala, M. C. 2014. Quantitative optical imaging of primary tumor organoid metabolism predicts drug response in breast cancer. *Cancer Res.* **74**: 5184-5194.

[129] Cheng, J.-X., Xie, X. S., *Coherent Raman scattering microscopy*, CRC Press, Boca Raton, FL, **2012**.
[130] Evans, C. L., Xie, X. S. 2008. Coherent anti-Stokes Raman scattering microscopy: chemical imaging for biology and medicine. *Annu. Rev. Anal. Chem.* **1**: 883-909.
[131] Cheng, J.-X., Xie, X. S. 2004. Coherent anti-Stokes Raman scattering microscopy: instrumentation, theory, and applications. *J. Phys. Chem. B* **108**: 827.
[132] Freudiger, C. W., Min, W., Saar, B. G., Lu, S., Holtom, G. R., He, C., et al. 2008. Label-free biomedical imaging with high sensitivity by stimulated Raman scattering microscopy. *Science* **322**: 1857-1861.
[133] Zhang, D., Wang, P., Slipchenko, M. N., Cheng, J. X. 2014. Fast vibrational imaging of single cells and tissues by stimulated Raman scattering microscopy. *Acc. Chem. Res.* **47**: 2282-2290.
[134] Min, W., Freudiger, C. W., Lu, S., Xie, X. S. 2011. Coherent nonlinear optical imaging: beyond fluorescence microscopy. *Annu. Rev. Phys. Chem.* **62**: 507-530.
[135] Palonpon, A. F., Sodeoka, M., Fujita, K. 2013. Molecular imaging of live cells by Raman microscopy. *Curr. Opin. Chem. Biol.* **17**: 708-715.
[136] Jr, C. H. C., Cicerone, M. T. 2015. Chemically sensitive bioimaging with coherent Raman scattering. *Nat. Photon.* **9**: 295-305.
[137] Krafft, C., Schie, I. W., Meyer, T., Schmitt, M., Popp, J. 2016. Developments in spontaneous and coherent Raman scattering microscopic imaging for biomedical applications. *Chem. Soc. Rev.* **45**: 1819-1849.
[138] Tipping, W. J., Lee, M., Serrels, A., Brunton, V. G., Hulme, A. N. 2016. Stimulated Raman scattering microscopy: an emerging tool for drug discovery. *Chem. Soc. Rev.* **45**: 2075-2089.
[139] Wei, L., Hu, F., Chen, Z., Shen, Y., Zhang, L., Min, W. 2016. Live-cell bioorthogonal chemical imaging: stimulated Raman scattering microscopy of vibrational probes. *Acc. Chem. Res.* **49**: 1494-1502.
[140] Prince, R. C., Frontiera, R. R., Potma, E. O. 2017. Stimulated Raman scattering: from bulk to nano. *Chem. Rev.* **117**: 5070-5094.
[141] Zhang, D., Slipchenko, M. N., Cheng, J. X. 2011. Highly sensitive vibrational imaging by femtosecond pulse stimulated Raman loss. *J. Phys. Chem. Lett.* **2**: 1248-1253.
[142] Jones, D. J., Potma, E. O., Cheng, J.-x., Burfeindt, B., Pang, Y., Ye, J., Xie, X. S. 2002. Synchronization of two passively mode-locked, picosecond lasers within 20 fs for coherent anti-Stokes Raman scattering microscopy. *Rev. Sci. Instrum.* **73**: 2843-2848.
[143] Ganikhanov, F., Carrasco, S., Sunney Xie, X., Katz, M., Seitz, W., Kopf, D. 2006. Broadly tunable dual-wavelength light source for coherent anti-Stokes Raman scattering microscopy. *Opt. Lett.* **31**: 1292-1294.
[144] Ozeki, Y., Dake, F., Kajiyama, S., Fukui, K., Itoh, K. 2009. Analysis and experimental assessment of the sensitivity of stimulated Raman scattering microscopy. *Opt. Express* **17**: 3651-3658.
[145] Zhang, D., Slipchenko, M. N., Leaird, D. E., Weiner, A. M., Cheng, J.-X. 2013. Spectrally modulated stimulated Raman scattering imaging with an angle-to-wavelength pulse shaper. *Opt. Express* **21**: 13864-13874.
[146] Slipchenko, M. N., Oglesbee, R. A., Zhang, D., Wu, W., Cheng, J. X. 2012. Heterodyne detected nonlinear optical imaging in a lock-in free manner. *J. Biophoton.* **5**: 801-807.

[147] Suhalim, J. L., Chung, C. Y., Lilledahl, M. B., Lim, R. S., Levi, M., Tromberg, B. J., Potma, E. O. 2012. Characterization of cholesterol crystals in atherosclerotic plaques using stimulated Raman scattering and second-harmonic generation microscopy. *Biophys. J.* **102**: 1988-1995.

[148] Mansfield, J. C., Littlejohn, G. R., Seymour, M. P., Lind, R. J., Perfect, S., Moger, J. 2013. Label-free chemically specific imaging in planta with stimulated Raman scattering microscopy. *Anal. Chem.* **85**: 5055-5063.

[149] Fu, D., Holtom, G., Freudiger, C., Zhang, X., Xie, X. S. 2013. Hyperspectral imaging with stimulated Raman scattering by chirped femtosecond lasers. *J. Phys. Chem. B* **117**: 4634-4640.

[150] Fu, D., Zhou, J., Zhu, W. S., Manley, P. W., Wang, Y. K., Hood, T., et al. 2014. Imaging the intracellular distribution of tyrosine kinase inhibitors in living cells with quantitative hyperspectral stimulated Raman scattering. *Nat. Chem.* **6**: 614-622.

[151] Hellerer, T., Enejder, A. M. K., Zumbusch, A. 2004. Spectral focusing: High spectral resolution spectroscopy with broad-bandwidth laser pulses. *Appl. Phys. Lett.* **85**.

[152] Zhang, D., Wang, P., Slipchenko, M. N., Ben-Amotz, D., Weiner, A. M., Cheng, J. X. 2013. Quantitative vibrational imaging by hyperspectral stimulated Raman scattering microscopy and multivariate curve resolution analysis. *Anal. Chem.* **85**: 98-106.

[153] Wang, K., Zhang, D., Charan, K., Slipchenko, M. N., Wang, P., Xu, C., Cheng, J. X. 2013. Time-lens based hyperspectral stimulated Raman scattering imaging and quantitative spectral analysis. *J. Biophoton.* **6**: 815-820.

[154] Ozeki, Y., Umemura, W., Otsuka, Y., Satoh, S., Hashimoto, H., Sumimura, K., et al. 2012. High-speed molecular spectral imaging of tissue with stimulated Raman scattering. *Nat. Photon.* **6**: 845-851.

[155] Ozeki, Y., Umemura, W., Sumimura, K., Nishizawa, N., Fukui, K., Itoh, K. 2012. Stimulated Raman hyperspectral imaging based on spectral filtering of broadband fiber laser pulses. *Opt. Lett.* **37**: 431-433.

[156] Marx, B., Czerwinski, L., Light, R., Somekh, M., Gilch, P. 2014. Multichannel detectors for femtosecond stimulated Raman microscopy – ideal and real ones. *J. Raman Spectrosc.* **45**: 521-527.

[157] Lu, F. K., Ji, M., Fu, D., Ni, X., Freudiger, C. W., Holtom, G., Xie, X. S. 2012. Multicolor stimulated Raman scattering (SRS) microscopy. *Mol. Phys.* **110**: 1927-1932.

[158] Seto, K., Okuda, Y., Tokunaga, E., Kobayashi, T. 2013. Development of a multiplex stimulated Raman microscope for spectral imaging through multi-channel lock-in detection. *Rev. Sci. Instrum.* **84**: 083705.

[159] Liao, C.-S., Slipchenko, M. N., Wang, P., Li, J., Lee, S.-Y., Oglesbee, R. A., Cheng, J.-X. 2015. Microsecond scale vibrational spectroscopic imaging by multiplex stimulated Raman scattering microscopy. *Light Sci. Appl.* **4**: e265.

[160] Fu, D., Lu, F. K., Zhang, X., Freudiger, C., Pernik, D. R., Holtom, G., Xie, X. S. 2012. Quantitative chemical imaging with multiplex stimulated Raman scattering microscopy. *J. Am. Chem. Soc.* **134**: 3623-3626.

[161] Liao, C. S., Wang, P., Li, J., Lee, H. J., Eakins, G., Cheng, J. X. 2015. Spectrometer-free vibrational imaging by retrieving stimulated Raman signal from highly scattered photons. *Sci. Adv.* **1**: e1500738.

[162] Fu, D., Xie, X. S. 2014. Reliable cell segmentation based on spectral phasor analysis of hyperspectral stimulated Raman scattering imaging data. *Anal. Chem.* **86**: 4115-4119.

[163] Wang, P., Liu, B., Zhang, D., Belew, M. Y., Tissenbaum, H. A., Cheng, J. X. 2014. Imaging lipid metabolism in live Caenorhabditis elegans using fingerprint vibrations. *Angew. Chem. Int. Ed. Engl.* **53**: 11787-11792.

[164] Liu, B., Wang, P., Kim, J. I., Zhang, D., Xia, Y., Chapple, C., Cheng, J. X. 2015. Vibrational fingerprint mapping reveals spatial distribution of functional groups of lignin in plant cell wall. *Anal. Chem.* **87**: 9436-9442.

[165] Saar, B. G., Freudiger, C. W., Stanley, C. M., Holtom, G. R., Xie, X. S. 2010. Video-rate molecular imaging in vivo with stimulated Raman scattering. *Science* **330**: 1368-1370.

[166] Ji, M., Orringer, D. A., Freudiger, C. W., Ramkissoon, S., Liu, X., Lau, D., et al. 2013. Rapid, label-free detection of brain tumors with stimulated Raman scattering microscopy. *Sci. Transl. Med.* **5**: 201-119.

[167] Le, T. T., Duren, H. M., Slipchenko, M. N., Hu, C. D., Cheng, J. X. 2010. Label-free quantitative analysis of lipid metabolism in living Caenorhabditis elegans[S]. *J. Lipid Res.* **51**: 672-677.

[168] Wang, M. C., Min, W., Freudiger, C. W., Ruvkun, G., Xie, X. S. 2011. RNAi screening for fat regulatory genes with SRS microscopy. *Nat. Methods* **8**: 135-138.

[169] Dou, W., Zhang, D., Jung, Y., Cheng, J. X., Umulis, D. M. 2012. Label-free imaging of lipid-droplet intracellular motion in early Drosophila embryos using femtosecond-stimulated Raman loss microscopy. *Biophys. J.* **102**: 1666-1675.

[170] Zhang, X., Roeffaers, M. B., Basu, S., Daniele, J. R., Fu, D., Freudiger, C. W., et al. 2012. Label-free live-cell imaging of nucleic acids using stimulated Raman scattering microscopy. *Chemphyschem.* **13**: 1054-1059.

[171] Hu, C. R., Zhang, D., Slipchenko, M. N., Cheng, J. X., Hu, B. 2014. Label-free real-time imaging of myelination in the Xenopus laevis tadpole by in vivo stimulated Raman scattering microscopy. *J. Biomed. Opt.* **19**: 086005.

[172] Li, J., Condello, S., Thomes-Pepin, J., Ma, X., Xia, Y., Hurley, T. D., et al. 2016. Lipid desaturation is a metabolic marker and therapeutic target of ovarian cancer stem cells. *Cell Stem Cell*.

[173] Lu, F. K., Calligaris, D., Olubiyi, O. I., Norton, I., Yang, W., Santagata, S., et al. 2016. Label-free neurosurgical pathology with stimulated Raman imaging. *Cancer Res.* **76**: 3451-3462.

[174] Wang, P., Li, J., Hu, C. R., Zhang, D., Sturek, M., Cheng, J. X. 2013. Label-free quantitative imaging of cholesterol in intact tissues by hyperspectral stimulated Raman scattering microscopy. *Angew. Chem. Int. Ed. Engl.* **52**: 13042-13046.

[175] Freudiger, C. W., Pfannl, R., Orringer, D. A., Saar, B. G., Ji, M., Zeng, Q., et al. 2012. Multicolored stain-free histopathology with coherent Raman imaging. *Lab Invest.* **92**: 1492-1502.

[176] O'Rourke, E. J., Soukas, A. A., Carr, C. E., Ruvkun, G. 2009. C. elegans major fats are stored in vesicles distinct from lysosome-related organelles. *Cell Metab.* **10**: 430-435.

[177] Mak, H. Y. 2012. Lipid droplets as fat storage organelles in Caenorhabditis elegans: Thematic review series: lipid droplet synthesis and metabolism: from yeast to man. *J. Lipid Res.* **53**: 28-33.

[178] Li, J., Cheng, J.-X. 2014. Direct visualization of de novo lipogenesis in single living cells. *Sci. Rep.* **4**: 6807.

[179] Wei, L., Yu, Y., Shen, Y., Wang, M. C., Min, W. 2013. Vibrational imaging of newly synthesized proteins in live cells by stimulated Raman scattering microscopy. *Proc. Natl. Acad. Sci. U. S. A.* **110**: 11226-11231.

[180] Wei, L., Shen, Y., Xu, F., Hu, F., Harrington, J. K., Targoff, K. L., Min, W. 2015. Imaging complex protein metabolism in live organisms by stimulated Raman scattering microscopy with isotope labeling. *ACS Chem. Biol.* **10**: 901-908.

[181] Hu, F., Wei, L., Zheng, C., Shen, Y., Min, W. 2014. Live-cell vibrational imaging of choline metabolites by stimulated Raman scattering coupled with isotope-based metabolic labeling. *Analyst* **139**: 2312-2317.

[182] Fu, D., Yu, Y., Folick, A., Currie, E., Farese, R. V., Jr., Tsai, T. H., et al. 2014. In vivo metabolic fingerprinting of neutral lipids with hyperspectral stimulated Raman scattering microscopy. *J. Am. Chem. Soc.* **136**: 8820-8828.

[183] Alfonso-Garcia, A., Pfisterer, S. G., Riezman, H., Ikonen, E., Potma, E. O. 2016. D38-cholesterol as a Raman active probe for imaging intracellular cholesterol storage. *J. Biomed. Opt.* **21**: 61003.

[184] Saar, B. G., Contreras-Rojas, L. R., Xie, X. S., Guy, R. H. 2011. Imaging drug delivery to skin with stimulated Raman scattering microscopy. *Mol. Pharm.* **8**: 969-975.

[185] Yamakoshi, H., Dodo, K., Palonpon, A., Ando, J., Fujita, K., Kawata, S., Sodeoka, M. 2012. Alkyne-tag Raman imaging for visualization of mobile small molecules in live cells. *J. Am. Chem. Soc.* **134**: 20681-20689.

[186] Wei, L., Hu, F., Shen, Y., Chen, Z., Yu, Y., Lin, C. C., et al. 2014. Live-cell imaging of alkyne-tagged small biomolecules by stimulated Raman scattering. *Nat. Methods* **11**: 410-412.

[187] Hong, S., Chen, T., Zhu, Y., Li, A., Huang, Y., Chen, X. 2014. Live-cell stimulated Raman scattering imaging of alkyne-tagged biomolecules. *Angew. Chem. Int. Ed. Engl.* **53**: 5827-5831.

[188] Shen, Y., Xu, F., Wei, L., Hu, F., Min, W. 2014. Live-cell quantitative imaging of proteome degradation by stimulated Raman scattering **. *Angew. Chem. Int. Ed. Engl.* **53**: 5596-5599.

[189] Lee, H. J., Zhang, W., Zhang, D., Yang, Y., Liu, B., Barker, E. L., et al. 2015. Assessing cholesterol storage in live cells and C. elegans by stimulated Raman scattering imaging of phenyl-diyne cholesterol. *Sci. Rep.* **5**: 7930.

[190] Swyer, G. I. M. 1942. The cholesterol content of normal and enlarged prostates. *Cancer Res.* **2**: 372-375.

[191] Solomon, K. R., Freeman, M. R. 2011. The complex interplay between cholesterol and prostate malignancy. *Urol. Clin. North Am.* **38**: 243-259.

[192] Krycer, J. R., Brown, A. J. 2013. Cholesterol accumulation in prostate cancer: a classic observation from a modern perspective. *Biochim. Biophys. Acta* **1835**: 219-229.

[193] Fukuchi, J., Hiipakka, R. A., Kokontis, J. M., Hsu, S., Ko, A. L., Fitzgerald, M. L., Liao, S. 2004. Androgenic suppression of ATP-binding cassette transporter A1 expression in LNCaP human prostate cancer cells. *Cancer Res.* **64**: 7682-7685.

[194] Siegel, R. L., Miller, K. D., Jemal, A. 2017. Cancer statistics, 2017. *CA. Cancer J. Clin.* **67**: 7-30.

[195] Watson, P. A., Arora, V. K., Sawyers, C. L. 2015. Emerging mechanisms of resistance to androgen receptor inhibitors in prostate cancer. *Nat. Rev. Cancer* **15**: 701-711.

[196] Igawa, T., Lin, F. F., Lee, M. S., Karan, D., Batra, S. K., Lin, M. F. 2002. Establishment and characterization of androgen-independent human prostate cancer LNCaP cell model. *Prostate* **50**: 222-235.

[197] Lin, H. K., Hu, Y. C., Yang, L., Altuwaijri, S., Chen, Y. T., Kang, H. Y., Chang, C. 2003. Suppression versus induction of androgen receptor functions by the phosphatidylinositol 3-kinase/Akt pathway in prostate cancer LNCaP cells with different passage numbers. *J. Biol. Chem.* **278**: 50902-50907.

[198] Unni, E., Sun, S., Nan, B., McPhaul, M. J., Cheskis, B., Mancini, M. A., Marcelli, M. 2004. Changes in androgen receptor nongenotropic signaling correlate with transition of LNCaP Cells to androgen independence. *Cancer Res.* **64**: 7156-7168.

[199] Youm, Y. H., Kim, S., Bahk, Y. Y., Yoo, T. K. 2008. Proteomic analysis of androgen-independent growth in low and high passage human LNCaP prostatic adenocarcinoma cells. *BMB reports* **41**: 722-727.

[200] Slipchenko, M. N., Le, T. T., Chen, H., Cheng, J. X. 2009. High-speed vibrational imaging and spectral analysis of lipid bodies by compound Raman microscopy. *J. Phys. Chem. B* **113**: 7681-7686.

[201] Park, S. I., Kim, S. J., McCauley, L. K., Gallick, G. E. 2010. Pre-clinical mouse models of human prostate cancer and their utility in drug discovery. *Curr. Protoc. Pharmacol.*, **51**: 14.15: 14.15.01-14.15.27.

[202] Pavese, J., Ogden, I. M., Bergan, R. C. 2013. An orthotopic murine model of human prostate cancer metastasis. *J. Vis. Exp.*: e50873.

[203] Quehenberger, O., Armando, A., Dumlao, D., Stephens, D. L., Dennis, E. A. 2008. Lipidomics analysis of essential fatty acids in macrophages. *Prostaglandins Leukot. Essent. Fatty Acids* **79**: 123-129.

[204] Yang, W. C., Adamec, J., Regnier, F. E. 2007. Enhancement of the LC/MS analysis of fatty acids through derivatization and stable isotope coding. *Anal. Chem.* **79**: 5150-5157.

[205] Movasaghi, Z., Rehman, S., Rehman, I. U. 2007. Raman spectroscopy of biological tissues. *Appl. Spectrosc. Rev.* **42**: 493-541.

[206] Kozlowski, J. M., Fidler, I. J., Campbell, D., Xu, Z. L., Kaighn, M. E., Hart, I. R. 1984. Metastatic behavior of human tumor cell lines grown in the nude mouse. *Cancer Res.* **44**: 3522-3529.

[207] Kaighn, M. E., Narayan, K. S., Ohnuki, Y., Lechner, J. F., Jones, L. W. 1979. Establishment and characterization of a human prostatic carcinoma cell line (PC-3). *Invest. Urol.* **17**: 16-23.

[208] Edamura, K., Nasu, Y., Takaishi, M., Kobayashi, T., Abarzua, F., Sakaguchi, M., et al. 2007. Adenovirus-mediated REIC/Dkk-3 gene transfer inhibits tumor growth and metastasis in an orthotopic prostate cancer model. *Cancer Gene Ther.* **14**: 765-772.

[209] Tripathi, V., Popescu, N. C., Zimonjic, D. B. 2014. DLC1 induces expression of E-cadherin in prostate cancer cells through Rho pathway and suppresses invasion. *Oncogene* **33**: 724-733.

[210] Zhang, H., Pan, Y., Zheng, L., Choe, C., Lindgren, B., Jensen, E. D., et al. 2011. FOXO1 inhibits Runx2 transcriptional activity and prostate cancer cell migration and invasion. *Cancer Res.* **71**: 3257-3267.

[211] Chandran, U. R., Ma, C., Dhir, R., Bisceglia, M., Lyons-Weiler, M., Liang, W., et al. 2007. Gene expression profiles of prostate cancer reveal involvement of multiple molecular pathways in the metastatic process. *BMC Cancer* **7**: 64.

[212] Yu, Y. P., Yu, G., Tseng, G., Cieply, K., Nelson, J., Defrances, M., et al. 2007. Glutathione peroxidase 3, deleted or methylated in prostate cancer, suppresses prostate cancer growth and metastasis. *Cancer Res.* **67**: 8043-8050.

[213] Bowen, C., Bubendorf, L., Voeller, H. J., Slack, R., Willi, N., Sauter, G., et al. 2000. Loss of NKX3.1 expression in human prostate cancers correlates with tumor progression. *Cancer Res.* **60**: 6111-6115.

[214] Kypta, R. M., Waxman, J. 2012. Wnt/beta-catenin signalling in prostate cancer. *Nature reviews. Urology* **9**: 418-428.

[215] Jung, S. J., Oh, S., Lee, G. T., Chung, J., Min, K., Yoon, J., et al. 2013. Clinical significance of Wnt/β-catenin signalling and androgen receptor expression in prostate cancer. *World J. Mens Health* **31**: 36-46.

[216] Dubrovska, A., Kim, S., Salamone, R. J., Walker, J. R., Maira, S. M., Garcia-Echeverria, C., et al. 2009. The role of PTEN/Akt/PI3K signaling in the maintenance and viability of prostate cancer stem-like cell populations. *Proc. Natl. Acad. Sci. U. S. A.* **106**: 268-273.

[217] Willert, K., Brown, J. D., Danenberg, E., Duncan, A. W., Weissman, I. L., Reya, T., et al. 2003. Wnt proteins are lipid-modified and can act as stem cell growth factors. *Nature* **423**: 448-452.

[218] Takada, R., Satomi, Y., Kurata, T., Ueno, N., Norioka, S., Kondoh, H., et al. 2006. Monounsaturated fatty acid modification of Wnt protein: its role in Wnt secretion. *Dev. Cell* **11**: 791-801.

[219] Tobin, K. A., Steineger, H. H., Alberti, S., Spydevold, O., Auwerx, J., Gustafsson, J. A., Nebb, H. I. 2000. Cross-talk between fatty acid and cholesterol metabolism mediated by liver X receptor-alpha. *Mol. Endocrinol.* **14**: 741-752.

[220] Ye, J., DeBose-Boyd, R. A. 2011. Regulation of cholesterol and fatty acid synthesis. *Cold Spring Harb. Perspect. Biol.* **3**: a004754.

[221] Chen, B., Dodge, M. E., Tang, W., Lu, J., Ma, Z., Fan, C. W., et al. 2009. Small molecule-mediated disruption of Wnt-dependent signaling in tissue regeneration and cancer. *Nat. Chem. Biol.* **5**: 100-107.

[222] Swinnen, J. V., Roskams, T., Joniau, S., Van Poppel, H., Oyen, R., Baert, L., et al. 2002. Overexpression of fatty acid synthase is an early and common event in the development of prostate cancer. *Int. J. Cancer* **98**: 19-22.

[223] Migita, T., Ruiz, S., Fornari, A., Fiorentino, M., Priolo, C., Zadra, G., et al. 2009. Fatty acid synthase: a metabolic enzyme and candidate oncogene in prostate cancer. *J. Natl. Cancer Inst.* **101**: 519-532.

[224] Wu, X., Daniels, G., Lee, P., Monaco, M. E. 2014. Lipid metabolism in prostate cancer. *Am. J. Clin. Exp. Urol.* **2**: 111-120.

[225] Attard, G., Parker, C., Eeles, R. A., Schroder, F., Tomlins, S. A., Tannock, I., et al. 2016. Prostate cancer. *Lancet* **387**: 70-82.

[226] Chen, F., Zhao, X. 2013. Prostate cancer: current treatment and prevention strategies. *Iran. Red. Crescent. Med. J.* **15**: 279-284.

[227] Scher, H. I., Fizazi, K., Saad, F., Taplin, M. E., Sternberg, C. N., Miller, K., et al. 2012. Increased survival with enzalutamide in prostate cancer after chemotherapy. *N. Engl. J. Med.* **367**: 1187-1197.

[228] Ferraldeschi, R., Welti, J., Luo, J., Attard, G., de Bono, J. S. 2015. Targeting the androgen receptor pathway in castration-resistant prostate cancer: progresses and prospects. *Oncogene* **34**: 1745-1757.

[229] de Gonzalo-Calvo, D., Lopez-Vilaro, L., Nasarre, L., Perez-Olabarria, M., Vazquez, T., Escuin, D., et al. 2015. Intratumor cholesteryl ester accumulation is associated with human breast cancer proliferation and aggressive potential: a molecular and clinicopathological study. *BMC Cancer* **15**: 460.

[230] Mulas, M. F., Abete, C., Pulisci, D., Pani, A., Massidda, B., Dessi, S., Mandas, A. 2011. Cholesterol esters as growth regulators of lymphocytic leukaemia cells. *Cell Prolif.* **44**: 360-371.

[231] Bandyopadhyay, S., Li, J., Traer, E., Tyner, J. W., Zhou, A., Oh, S. T., Cheng, J. X. 2017. Cholesterol esterification inhibition and imatinib treatment synergistically inhibit growth of BCR-ABL mutation-independent resistant chronic myelogenous leukemia. *PLoS One* **12**: e0179558.

[232] Geng, F., Cheng, X., Wu, X., Yoo, J. Y., Cheng, C., Guo, J. Y., et al. 2016. Inhibition of SOAT1 suppresses glioblastoma growth via blocking SREBP-1-mediated lipogenesis. *Clin. Cancer Res.* **22**: 5337-5348.

[233] Griffiths, B., Lewis, C. A., Bensaad, K., Ros, S., Zhang, Q., Ferber, E. C., et al. 2013. Sterol regulatory element binding protein-dependent regulation of lipid synthesis supports cell survival and tumor growth. *Cancer Metab.* **1**: 3.

[234] Guo, D., Bell, E. H., Mischel, P., Chakravarti, A. 2014. Targeting SREBP-1-driven lipid metabolism to treat cancer. *Curr. Pharm. Des.* **20**: 2619-2626.

[235] Liu, J., Pan, S., Hsieh, M. H., Ng, N., Sun, F., Wang, T., et al. 2013. Targeting Wnt-driven cancer through the inhibition of Porcupine by LGK974. *Proc. Natl. Acad. Sci. U. S. A.* **110**: 20224-20229.

[236] Dan, R., Van Allen, E. M., Wu, Y. M., Schultz, N., Lonigro, R. J., Mosquera, J. M., et al. 2015. Integrative clinical genomics of advanced prostate cancer. *Cell* **161**: 1215-1228.

[237] Fiorentino, M., Zadra, G., Palescandolo, E., Fedele, G., Bailey, D., Fiore, C., et al. 2008. Overexpression of fatty acid synthase is associated with palmitoylation of Wnt1 and cytoplasmic stabilization of beta-catenin in prostate cancer. *Lab Invest.* **88**: 1340-1348.

[238] Nelson, E. R., Wardell, S. E., Jasper, J. S., Park, S., Suchindran, S., Howe, M. K., et al. 2013. 27-Hydroxycholesterol links hypercholesterolemia and breast cancer pathophysiology. *Science* **342**: 1094-1098.

[239] Arthur, J. R., Heinecke, K. A., Seyfried, T. N. 2011. Filipin recognizes both GM1 and cholesterol in GM1 gangliosidosis mouse brain. *J. Lipid Res.* **52**: 1345-1351.

[240] Yamakoshi, H., Dodo, K., Okada, M., Ando, J., Palonpon, A., Fujita, K., et al. 2011. Imaging of EdU, an alkyne-tagged cell proliferation probe, by Raman microscopy. *J. Am. Chem. Soc.* **133**: 6102-6105.

[241] Pezacki, J. P., Blake, J. A., Danielson, D. C., Kennedy, D. C., Lyn, R. K., Singaravelu, R. 2011. Chemical contrast for imaging living systems: molecular vibrations drive CARS microscopy. *Nat. Chem. Biol.* **7**: 137-145.

[242] Matthaus, C., Krafft, C., Dietzek, B., Brehm, B. R., Lorkowski, S., Popp, J. 2012. Noninvasive imaging of intracellular lipid metabolism in macrophages by Raman microscopy in combination with stable isotopic labeling. *Anal. Chem.* **84**: 8549-8556.

[243] Xie, X. S., Yu, J., Yang, W. Y. 2006. Living cells as test tubes. *Science* **312**: 228-230.

[244] Bergner, G., Albert, C. R., Schiller, M., Bringmann, G., Schirmeister, T., Dietzek, B., et al. 2011. Quantitative detection of C-deuterated drugs by CARS microscopy and Raman microspectroscopy. *Analyst* **136**: 3686-3693.

[245] Shao, Y., Molnar, L. F., Jung, Y., Kussmann, J., Ochsenfeld, C., Brown, S. T., et al. 2006. Advances in methods and algorithms in a modern quantum chemistry program package. *Phys. Chem. Chem. Phys.* **8**: 3172-3191.

[246] Gordon, M. S., Schmidt, M. W. 2005. Chapter 41 - Advances in electronic structure theory: GAMESS a decade later. *Theory and Applications of Computational Chemistry*: 1167-1189.

[247] Millard, E. E., Srivastava, K., Traub, L. M., Schaffer, J. E., Ory, D. S. 2000. Niemann-pick type C1 (NPC1) overexpression alters cellular cholesterol homeostasis. *J. Biol. Chem.* **275**: 38445-38451.

[248] Lee, J. Y., Suh, S. B., Kim, K. S. 2000. Polyenes vs polyynes: Efficient π-frame for nonlinear optical pathways. *J. Chem. Phys.* **112**: 344-348.

[249] Cadigan, K. M., Chang, C. C., Chang, T. Y. 1989. Isolation of Chinese hamster ovary cell lines expressing human acyl-coenzyme A/cholesterol acyltransferase activity. *J. Cell Biol.* **108**: 2201-2210.

[250] Carstea, E. D., Morris, J. A., Coleman, K. G., Loftus, S. K., Zhang, D., Cummings, C., et al. 1997. Niemann-Pick C1 disease gene: homology to mediators of cholesterol homeostasis. *Science* **277**: 228-231.

[251] Liu, B., Turley, S. D., Burns, D. K., Miller, A. M., Repa, J. J., Dietschy, J. M. 2009. Reversal of defective lysosomal transport in NPC disease ameliorates liver dysfunction and neurodegeneration in the npc1-/- mouse. *Proc. Natl. Acad. Sci. U. S. A.* **106**: 2377-2382.

[252] Abi-Mosleh, L., Infante, R. E., Radhakrishnan, A., Goldstein, J. L., Brown, M. S. 2009. Cyclodextrin overcomes deficient lysosome-to-endoplasmic reticulum transport of cholesterol in Niemann-Pick type C cells. *Proc. Natl. Acad. Sci. U. S. A.* **106**: 19316-19321.

[253] Valdes, V. J., Athie, A., Salinas, L. S., Navarro, R. E., Vaca, L. 2012. CUP-1 is a novel protein involved in dietary cholesterol uptake in Caenorhabditis elegans. *PLoS One* **7**: e33962.

[254] Zhang, S. O., Box, A. C., Xu, N., Le Men, J., Yu, J., Guo, F., et al. 2010. Genetic and dietary regulation of lipid droplet expansion in Caenorhabditis elegans. *Proc. Natl. Acad. Sci. U. S. A.* **107**: 4640-4645.

[255] Ekkebus, R., van Kasteren, S. I., Kulathu, Y., Scholten, A., Berlin, I., Geurink, P. P., et al. 2013. On terminal alkynes that can react with active-site cysteine nucleophiles in proteases. *J. Am. Chem. Soc.* **135**: 2867-2870.

[256] Dix, J. A., Verkman, A. S. 1990. Pyrene eximer mapping in cultured fibroblasts by ratio imaging and time-resolved microscopy. *Biochemistry* **29**: 1949-1953.

[257] Kaletta, T., Hengartner, M. O. 2006. Finding function in novel targets: C. elegans as a model organism. *Nat. Rev. Drug Discov.* **5**: 387-398.

[258] Li, J., Brown, G., Ailion, M., Lee, S., Thomas, J. H. 2004. NCR-1 and NCR-2, the C. elegans homologs of the human Niemann-Pick type C1 disease protein, function upstream of DAF-9 in the dauer formation pathways. *Development* **131**: 5741-5752.

[259] Ashrafi, K., Chang, F. Y., Watts, J. L., Fraser, A. G., Kamath, R. S., Ahringer, J., Ruvkun, G. 2003. Genome-wide RNAi analysis of Caenorhabditis elegans fat regulatory genes. *Nature* **421**: 268-272.

[260] Merris, M., Wadsworth, W. G., Khamrai, U., Bittman, R., Chitwood, D. J., Lenard, J. 2003. Sterol effects and sites of sterol accumulation in Caenorhabditis elegans: developmental requirement for 4alpha-methyl sterols. *J. Lipid Res.* **44**: 172-181.

[261] Yen, K., Le, T. T., Bansal, A., Narasimhan, S. D., Cheng, J. X., Tissenbaum, H. A. 2010. A comparative study of fat storage quantitation in nematode Caenorhabditis elegans using label and label-free methods. *PloS one* **5**: e12810.

VITA

Hyeon Jeong Lee

Comparative Pathobiology, Purdue University

Education

B.S., 2011, Department of Biochemical Science and Technology, National Taiwan University, Taipei City, Taiwan (R.O.C.)

Ph.D., 2017, Comparative Pathobiology Department, Interdisciplinary Life Science program, Purdue University, West Lafayette, IN, USA

Research Interests

Cancer metabolism

Lipid metabolism

Cancer diagnosis and treatment

Biomedical imaging

PUBLICATIONS

- **Hyeon Jeong Lee**, Jie Li, Renee E. Vickman, Junjie Li, Rui Liu, Abigail C. Durkes, Bennett D. Elzey, Shuhua Yue, Xiaoqi Liu, Timothy L. Ratliff, Ji-Xin Cheng (2017). Inhibition of Cholesterol Esterification Suppresses Prostate Cancer Metastasis through Impairing Wnt/β-catenin Pathway. *Mol. Cancer Res*. (under review).
- **Hyeon Jeong Lee**, Ji-Xin Cheng (2017). Imaging Chemistry inside Living Cells by Stimulated Raman Scattering Microscopy. *Methods* 128: 119-28.
- Jiayingzi Wu, Liyan You, Lu Lan, **Hyeon Jeong Lee**, Saadia T. Chaudhry, Rui Li, Ji-Xin Cheng, Jianguo Mei (2017). Semiconducting Polymer Nanoparticles for Centimeters-Deep Photoacoustic Imaging in the Second Near-Infrared Window. *Adv. Mater*. 29:1703403
- **Hyeon Jeong Lee**, Delong Zhang, Ying Jiang, Xiangbing Wu, Pei-Yu Shih, Chien-Sheng Liao, Brittani Bungart, Xiao-Ming Xu, Ryan M. Drenan, Edward Bartlett, Ji-Xin Cheng (2017). Label-Free Vibrational Spectroscopic Imaging of Neuronal Membrane Potential. *J. Phys. Chem. Lett*. 8(9): 1932-6.
- Chien-Sheng Liao, Pu Wang, Ping Wang, Junjie Li, **Hyeon Jeong Lee**, Gregory Eakins, Ji-Xin Cheng (2015). Spectrometer-free Vibrational Imaging by Retrieving Stimulated Raman Signal from Highly Scattered Photons. *Sci. Adv.* 1(9): e1500738.
- Bin Liu, **Hyeon Jeong Lee**, Delong Zhang, Chien-Sheng Liao, Na Ji, Yuanqin Xia, and Ji-Xin Cheng (2015). Label-free Spectroscopic Detection of Membrane Potential using Stimulated Raman Scattering. *Appl. Phys. Lett*. 106: 173704.
- Dennis J. Lee, Kyunghun Han, **Hyeon Jeong Lee** and Andrew M. Weiner (2015). Synthetic Aperture Microscopy Based on Referenceless Phase Retrieval with an Electrically Tunable Lens. *Appl. Opt*. 54(17): 5346-52.
- **Hyeon Jeong Lee**, Wandi Zhang, Delong Zhang, Yang Yang, Bin Liu, Eric L. Barker, Kimberly K. Buhman, Lyudmila V. Slipchenko, Mingji Dai, Ji-Xin Cheng (2015). Assessing Cholesterol Metabolism and Storage in Live Cells by SRS Imaging of Phenyl-Diyne Cholesterol. *Sci. Rep.* 5:7930.

- Shuhua Yue, Junjie Li, Seung-Young Lee, **Hyeon Jeong Lee**, Tian Shao, Bing Song, Liang Cheng, Timothy A. Masterson, Xiaoqi Liu, Timothy L. Ratliff, Ji-Xin Cheng (2014). Cholesteryl Ester Accumulation Induced by PTEN Loss and PI3K/AKT Activation Underlies Human Prostate Cancer Aggressiveness. *Cell Metab*. 19(3):393-406.
- Aki Uchida, **Hyeon Jeong Lee**, Ji-Xin Cheng, and Kimberly K. Buhman (2013). Imaging Cytoplasmic Lipid Droplets in Enterocytes and Assessing Dietary Fat Absorption. *Methods Cell Biol*. 116:151-66.
- Hao-Yen Chang, Chi-Chen Fan, Po-Chen Chu, Bo-En Hong, **Hyeon Jeong Lee**, Mau-Sun Chang (2011). hPuf-A/KIAA0020 Modulates PARP-1 Cleavage upon Genotoxic Stress. *Cancer Res.* 71(3):1126-34.